THE UNIVERSITY OF CHICAGO

THREE DIMENSIONAL STRUCTURES IN THE DIRECTED SELF-ASSEMBLY OF BLOCK COPOLYMERS

A DISSERTATION SUBMITTED TO

THE FACULTY OF THE INSTITUTE FOR MOLECULAR ENGINEERING

IN CANDIDACY FOR THE DEGREE OF

DOCTOR OF PHILOSOPHY

BY

JIAXING REN

CHICAGO, ILLINOIS

AUGUST 2017

TABLE OF CONTENTS

LIST OF FIGURES

LIST OF TABLES

ACKNOWLEDGEMENT

First and foremost, I would like to thank my advisor, Prof. Paul Nealey, for his guidance and support throughout my graduate study. I greatly appreciate the many insightful discussions that drove and led me to uncover the fundamental mechanisms behind physical phenomena. He also gave me the research freedom to pursue topics of interest as well as the opportunities to expand my knowledge and skills through various external collaborations.

Secondly, I am deeply grateful to have worked with amazing group members who helped me tremendously in both work and life. Special thanks to Dr. Tamar Segal-Peretz and Chun Zhou for the beautiful TEM tomography data essential to my research. I would like to thank Xuanxuan Chen for her company and support through every moment of my graduate life as well as Dr. Xiao Li, Dr. Hyo Seon Suh, Robert Seidel, Lance Williamson, Paulina Rincon, Takejiro Inoue, Dr. Shisheng Xiong, Dr. Christopher Arges, Dr. Xiaoying Liu, Dr. Mark Stoykovich, Dr. Manolis Doxastakis, Jiajing Li, Moshe Dolejsi and the rest of the group for their help and advice.

I also benefited greatly from many research collaborations. Prof. de Pablo and his group members, Daman, Grant, Alec, Abelardo and Cody, provided simulation support and theoretical understanding for my experiments. Prof. Sibener and Jonathan Raybin helped launch the research into DSA kinetics. Dr. Leo Ocola, Dr. Ralu Divan and Dr. David Czaplewski at Argonne CNM are instrumental in developing the nanofabrication processes. Dr. Roel Gronheid and Jan Doise at imec provided precious guiding templates and helped reengineer the back etch process. Dr. R. Joseph Kline, Dr. Daniel Sunday and Dr. Christopher Liman characterized the grating structures using soft X-ray scattering. I would also like to thank the incredible managers at the UChicago user facilities, Dr. Peter Duda, Dr. Qiti Guo and Dr. Justin Jureller, for their constant support on sample characterization and fabrication.

Finally, I must thank my wife and my parents. Without them, none of this work would have been possible, nor would it have any meaning. Their love, support and encouragement throughout the years gave me the strength to complete this journey.

ABSTRACT

Directed self-assembly (DSA) of block copolymers (BCP) can multiply the resolution of conventional lithography and has been studied extensively for the next generation of nanopatterning. Great progress has been made in DSA using guide patterns with chemical or topographical contrast to achieve high levels of ordering, registration and pattern complexity that enable technological applications. However, most of the focus has been on perfecting the two-dimensional ordering of BCP for pattern transfer and the investigation on the three-dimensional (3D) structures inside the BCP films has been rare. Characterization of the 3D structures plays a critical role in understanding the fundamental physics behind polymer assembly and the ability to control the 3D structures offers great potential for direct 3D nanofabrication.

This dissertation focuses on the characterization and manipulation of the 3D structures in BCP DSA. In Chapter 1, important literatures and the rationale for studying the 3D structures in DSA are briefly discussed. Characterization of DSA-derived features are mostly based on top-down SEM imaging but it provides only surface information. TEM tomography has emerged as a powerful tool for though-film characterization but it requires samples to be prepared on specialized membrane substrates. Chapter 2 describes the sample fabrication method necessary to enable 3D metrologies. We developed a generalizable process to implement BCP DSA on silicon nitride membranes. A key feature of the process developed here is that it does not introduce any artifacts or damage to the polymer assemblies as DSA is performed prior to back-etched membrane formation.

In Chapter 3, we used TEM tomography to systematically and quantitatively investigate the BCP morphology through the film thickness for different template geometries. Results showed that incommensurate confinement from template topography could cause roughness and

intermittent dislocations in domains over the background region at the bottom of the film. We also demonstrated that the positional fluctuations of the BCP interface between domains showed a depth-dependent behavior, with high levels of fluctuations near both the free surface and the substrate and lower fluctuation levels in the middle of the film.

In Chapter 4, we investigated the kinetic evolution of 3D structures in density multiplication DSA to elucidate the crucial role of transient 3D structures in determining the thermodynamic landscape and defectivity. We found that morphologies are first developed independently at the top and bottom of the film and then evolve cooperatively as grains coarsen. There also exists a metastable "stitched" morphology that represents an undesirable bottleneck in the kinetic evolution. We demonstrated that by engineering the DSA conditions to disfavor the metastable stitched morphology the speed of assembly could be greatly enhanced by over 100x.

Chapter 5 explores the DSA of 3D structures using 2D chemical patterns. BCPs spontaneously assemble into periodic 3D structures at the nanometer length scale. Using sphere-forming BCP, we showed that the crystallographic symmetries and orientations of the 3D lattice could be deliberately controlled by matching the 2D chemical pattern and the film thickness to the lattice. The ordered structure is also able to propagate through 300 nm thick films. Using Wigner-Seitz cells, we estimated the relative stability of different crystallographic geometries and established the rules governing 3D DSA.

This research highlights the significance of 3D structures in understanding BCP DSA and extends the concept of DSA into the third dimension, enabling better process design and advanced 3D fabrication of functional materials.

CHAPTER 1: INTRODUCTION

1.1 Motivation

In 1965, Dr. Gordon Moore made the observation and prediction, known as "Moore's Law", that the number of transistors in an integrated circuit will double every two years.[1] For more than five decades, Moore's Law has guided the development of the semiconductor industry and laid the foundation for the unprecedented advancement of information technology. By 2017, the transistor count for commercially available CPU has exceeded 10 billion and the minimum pitch of critical layers has dropped to around 35 nm.[2] Nanofabrication at such small length scales poses tremendous technological challenge, especially on lithography.[3] Due to the diffraction limit, the 193 nm immersion scanners currently used in the industry has a maximum resolution of ~80 nm periodicity for dense line and space features. The development of next-generation light sources with smaller wavelength such as Extreme Ultraviolet Lithography (EUV) is also proven to be a difficult and prolonged process.[4] To address the bottleneck in lithographical resolution and ensure the continuation of Moore's Law, multiple-patterning is required to enhance the feature density after the lithography step. One of the multiple-patterning techniques being developed is the Directed Self-Assembly (DSA) of block copolymers.[5]

1.2 Block copolymer thin film morphology

Block copolymers (BCP) spontaneously form nanostructures with high uniformity at the length scales between 5 and 50 nm.[6] Microphase separation and nanostructure formation are driven by the thermodynamic incompatibility between the constituent polymer blocks as determined by the Flory–Huggins interaction parameter (χ) and the degree of polymerization (N). For diblock copolymers, where two chemically distinct polymer blocks are covalently linked at

one end, the nanoscale morphology can be tailored between dense arrays of spheres, cylinders, gyroids and lamellae by changing the volume fraction of the two blocks. The morphology results from the minimization of the thermodynamic free energy of the system. In the bulk, this is achieved by balancing the entropic contributions to limit chain stretching with the enthalpic interactions to minimize inter-block contacts. In the thin film, the polymer morphology is also determined by additional boundary conditions including the interactions at the free surface and the substrate interface as well as the constraints of film thickness.[7]

One particular morphology of interest is the lamellae phase, formed by diblock copolymers with symmetric volume fractions. The orientation of the lamellae in the thin film can be controlled by tuning the surface properties at the free surface and the substrate as well as the commensurability between the film thickness and the lamellae natural periodicity (L_0).[8,9] Surfaces that are preferential for one of the blocks will cause the lamellae to align parallel to the substrate. A flat film can be obtained only when the film thickness is commensurate with L_0, whereas incommensurate film thickness will lead to terracing and the formation of holes and islands. When the surfaces are non-preferential for either of the blocks, the lamellae will orient perpendicularly to the substrate. Non-preferential substrate interface is typically achieved by grafting a layer of random copolymer brush,[10] whereas non-preferential free surface can be obtained by solvent annealing,[11,12] applying a "top coat",[13–15] or choosing BCP chemistries that have similar surface energies between the two blocks.[16,17]

1.3 Directed Self-Assembly of block copolymers

Although the self-assembled structures of BCPs are highly uniform, they lack long range order and registration to the substrate. Ordering could be improved by solvent annealing,[18]

applying external magnetic or electric fields,[19–21] and mechanical shear,[22] but the resulting structures are still far from the level of perfection required for semiconductor fabrication. Alternatively, the BCP assembly can be guided by lithographically defined templates to reach high levels of perfection and substrate registration that enables technical applications, widely known as the Directed Self-Assembly (DSA).[5,23,24] The periods of the guiding templates are usually larger than 80 nm and up to several microns and easily handled by existing lithographic tools. Yet the self-assembled structures typically have periods less than 40 nm and down to even 10 nm, well beyond the resolution of the immersion scanners, leading to a significant increase in feature density. The self-assembled patterns are then transferred on to the substrate using dry etch to form functional structures. Of particular interest are the dense dot and line/space patterns due to their applications in high density storage media and integrated circuits respectively.

Among various guiding schemes in DSA, guiding templates that uses either topographical features, known as graphoepitaxy, or chemical contrast, known as chemoepitaxy, have been most widely studied. Graphoepitaxy DSA was first demonstrated in 2001 by Segalman *et al.*[25] using lithographically patterned trenches to guide the assembly of a monolayer of polystyrene-*block*-poly(2-vinylpyridine) (PS-*b*-P2VP) spheres into a single crystalline domain with hexagonal symmetry. Subsequently, topographical trenches or grooves have been used to align spheres[26,27] and perpendicular cylinders[28,29] into well-ordered dot patterns as well as to direct the self-assembly of perpendicular lamellae[30,31] and parallel cylinders[28,32] to form line and space patterns. In this form of graphoepitaxy, the guiding features typically leave a large undesirable footprint in the final device, which complicates device integration. To address issue, it is necessary to miniaturize the guiding features to the size of a single polymer domain. In 2008, Bita *et al.*[33] demonstrated the use of lithographically patterned posts to guide the assembly

of perpendicular cylinders so a uniform pattern could be obtained. Similarly, guiding mesas with the same dimension as the polymer blocks have been fabricated to template the assembly of parallel cylinders.[34]

Chemoepitaxy DSA, pioneered by Nealey *et al.*,[35] was first demonstrated in 2003 using patterned self-assembled monolayer to template the assembly of BCP lamellae into single-crystalline line/space domains over arbitrarily large area. In this first demonstration, however, the lithographic template had the same periodicity as the BCP, without the power to multiply feature density as in graphoepitaxy. Density multiplication using chemical patterns were subsequently achieved in 2008 by Ruiz *et al.*[36] and Cheng *et al.*[37] for dense dot arrays and line/space patterns respectively. In density multiplication chemoepitaxy, the template typically consists of two chemically distinct regions: guiding stripes/spots that are preferential for one of the BCP blocks and background regions that are mostly non-preferential to both blocks. Unlike graphoepitaxy, chemoepitaxy naturally generates uniform features over the entire patterned surface. But on the other hand it also requires the guiding stripes to have similar dimension as a single polymer domain, difficult to be directly patterned by immersion lithography. To integrate chemoepitaxy into the current semiconductor fabrication process based on 193 nm lithography, Liu *et al.*[38] developed a DSA flow, widely known as the "Line Flow", that uses trim etch to shrink the line width of guiding stripes to sub-lithography dimensions. The background chemistry is controlled by grafting a random copolymer brush in between the crosslinked guide stripes. In 2012, Line Flow DSA was successfully demonstrated on 300 mm track-processed wafers at imec, a first in the industry.[39] DSA has since attracted significant research attention and has been highlighted by the ITRS roadmap as one of the leading multiple patterning techniques for advanced lithography.[40]

1.4 Three dimensional structures in DSA

Since the main application of DSA is as an etch mask for pattern transfer on to the substrate, most of the research has focused on improving the two dimensional (2D) ordering, evaluated using top down metrologies such as scanning electron microscopy (SEM) and atomic force microscopy (AFM). However, the BCP morphologies are inherently three dimensional (3D). Even for relatively simple BCP architectures such as lamellae and cylinders, complex non-bulk 3D structures can arise at grain boundaries, at defective sites, at transient states during structural formation, or when the polymer is subjected to confinements and boundary conditions.[41] Accessing 3D information is challenging as the structures are buried inside the film and hidden from top down metrologies. Most studies therefore relied on molecular simulations to reveal the details of 3D structures. Using a combination of coarse grain simulation and top down SEM analysis, Liu *et al.*[42] demonstrated that at certain DSA conditions the lamellae could be broken up inside the film even though the top surface appears to be well-aligned, which would negatively impact subsequent pattern transfer. Detcheverry *et al.*[43] investigated the influence of the geometry and chemistry of the guiding template on the DSA of lamella-forming BCP. They found that changing the interaction strength of the guiding stripes and the background can lead to various complex 3D structures including mixed lamellae, "checkerboard" patterns as well as "dot and stitch" patterns. Hur *et al.*[44] studied the annihilation pathway for dislocation pairs in lamellae DSA and found that there exists multiple 3D metastable states along the minimum free energy path toward alignment. Escaping from these metastable states requires formation of 3D transient structures that have high free energy barriers which could cause the defects to be kinetically trapped. The above examples illustrate that studying the 3D structures and their formation is crucial for understanding the fundamental interactions that govern polymer assembly.

Other than being used as a sacrificial etch mask for pattern transfer, BCPs are also capable of forming structures with highly uniform 3D lattice that can provide functionalities in their own right. For example the double gyroid structures formed by triblock copolymers have been used to fabricate 3D photonic crystals that would otherwise require laborious stacking of multiple lithographically patterned layers with difficult overlay.[45,46] Several strategies have been explored for three dimensional fabrication using BCPs. First is a layer-by-layer process that stacks multiple crosslinked layers of BCP into a 3D structure, analogous to the sequential lithography process.[47] Consequently, this strategy shares similar disadvantages with a large number of process steps and difficult overlay. Another method is to use 3D topographical templates to guide the BCP assembly.[48] It relies on the self-assembly of the BCP to propagate into the third dimension, thus eliminated the need for sequential processing. However, the topographical templates take up significant footprint in the resulting 3D structure and miniaturization is not as straight forward as in 2D graphoepitaxy due to the high aspect ratio required. A third strategy is to extend the chemoepitaxy concept to the third dimension and use 2D chemical patterns to control the BCP assembly in thick films. Welander *et al.*[49] demonstrated using lamellae forming BCPs that DSA can propagate more than 600 nm in thickness when the template geometry is commensurate with polymer spacing. Perpendicular lamellae and cylinders have no periodicity in the third dimension and therefore have no commensurability concerns in film thickness. It is of great fundamental interest to investigate the DSA of BCPs with 3D lattice structures that have repeating features in all three dimensions.

1.5 Three dimensional metrology

As mentioned in the earlier section, challenges remain in the experimental characterization of 3D structures in BCP films. The vast majority of DSA metrology is by top

down SEM imaging, which provides limited or even misleading information on 3D morphology. Cross-sectional SEM can reveal the through-film structure on a single plane, though cross-sectional sample preparation for BCP films often damages the polymer structure.[50] Ion milling can be used to polish the damaged surface but it is a laborious process and results in only limited imaging area. X-ray scattering methods have also been used to study polymer 3D structures.[51] Scattering is capable of extracting quantitative and statistical information from large areas of the sample, especially suitable for analyzing repeating structures that are prevalent in BCP assembly. But it lacks the ability to characterize non-uniform and isolated structures such as defects. On the other hand, electron tomography has been demonstrated to be a powerful tool to visualize complicated 3D structures in polymer thin films, complementing the scattering techniques.[41] Both X-ray and TEM requires samples to be prepared on thin membrane substrates. Integration of membrane fabrication into the DSA process is desired to allow 3D metrology.

1.6 Outline

The primary focus of this document is on characterizing 3D structures in BCP DSA and understanding their impact on self-assembly. Chapter 2 describes a generalizable process to implement BCP DSA on silicon nitride membranes that enables 3D metrologies. In Chapter 3, we use TEM tomography to systematically and quantitatively investigate the BCP morphology through the film thickness for different template geometries. In Chapter 4, we investigate the kinetic evolution of 3D structures in density multiplication DSA to elucidate the crucial role of transient 3D structures in determining the thermodynamic landscape and defectivity. We also engineer DSA conditions to optimize the 3D structural evolution and enhance the kinetics of assembly. In Chapter 5, we explore the DSA of 3D structures using 2D chemical patterns and seek to establish the rules governing 3D DSA.

1.7 References

1. Moore, G. E. Cramming more components onto integrated circuits (Reprinted from Electronics, pg 114-117, April 19, 1965). *Proc. Ieee* **86,** 82–85 (1965).

2. Brain, R. Interconnect Scaling : Challenges and Opportunities. 232–235 (2016).

3. Totzeck, M., Ulrich, W., Göhnermeier, a. & Kaiser, W. Pushing deep ultraviolet lithography to its limits. *Nat. Photon.* **1,** 629–631 (2007).

4. Pirati, A. *et al.* EUV lithography performance for manufacturing: status and outlook. **9776,** 97760A (2016).

5. Ji, S., Wan, L., Liu, C. C. & Nealey, P. F. Directed self-assembly of block copolymers on chemical patterns: A platform for nanofabrication. *Prog. Polym. Sci.* **54–55,** 76–127 (2016).

6. Bates, F. S. & Fredrickson, G. H. Block Copolymers—Designer Soft Materials. *Phys. Today* **52,** 32 (1999).

7. Albert, J. N. L. & Epps, T. H. Self-assembly of block copolymer thin films. *Mater. Today* **13,** 24–33 (2010).

8. Suh, H. S., Kang, H., Nealey, P. F. & Char, K. Thickness dependence of neutral parameter windows for perpendicularly oriented block copolymer thin films. *Macromolecules* **43,** 4744–4751 (2010).

9. Suh, H. S., Kang, H., Liu, C. C., Nealey, P. F. & Char, K. Orientation of block copolymer resists on interlayer dielectrics with tunable surface energy. *Macromolecules* **43,** 461–466 (2010).

10. Mansky, P., Liu, Y., Huang, E., Russell, T. P. & Hawker, C. J. Controlling Polymer-Surface Interactions with Random Copolymer Brushes. *Science (80-.).* **275,** 1458–1460 (1997).

11. Kim, S. H., Misner, M. J., Xu, T., Kimura, M. & Russell, T. P. Highly Oriented and Ordered Arrays from Block Copolymers via Solvent Evaporation. *Adv. Mater.* **16,** 226–231 (2004).

12. Xiong, S. *et al.* Directed Self-Assembly of Triblock Copolymer on Chemical Patterns for Sub-10-nm Nanofabrication via Solvent Annealing. *ACS Nano* **10,** 7855–7865 (2016).

13. Bates, C. M. *et al.* Polarity-switching top coats enable orientation of sub-10-nm block copolymer domains. *Science* **338,** 775–9 (2012).

14. Suh, H. S. *et al.* Sub-10-nm patterning via directed self-assembly of block copolymer films with a vapour-phase deposited topcoat. *Nat. Nanotechnol.* (2017). doi:10.1038/nnano.2017.34

15. Yoshida, H. *et al.* Topcoat Approaches for Directed Self-Assembly of Strongly Segregating Block Copolymer Thin Films. *J. Photopolym. Sci. Technol.* **26,** 55–58 (2013).

16. Kim, S., Nealey, P. F. & Bates, F. S. Decoupling Bulk Thermodynamics and Wetting Characteristics of Block Copolymer Thin Films. *ACS Macro Lett.* **1,** 11–14 (2012).

17. Yang, G.-W. *et al.* Directed Self-Assembly of Polystyrene-b-poly(propylene carbonate) on Chemical Patterns via Thermal Annealing for Next-Generation Lithography. *Nano Lett.* acs.nanolett.6b05059 (2017). doi:10.1021/acs.nanolett.6b05059

18. Kim, S. H., Misner, M. J. & Russell, T. P. Solvent-Induced Ordering in Thin Film Diblock Copolymer/Homopolymer Mixtures. *Adv. Mater.* **16,** 2119–2123 (2004).

19. Thurn-Albrecht, T. *et al.* Ultrahigh-Density Nanowire Arrays Grown in Self-Assembled Diblock Copolymer Templates. *Science (80-.).* **290,** 2126–2129 (2000).

20. Morkved, T. L. *et al.* Local Control of Microdomain Orientation in Diblock Copolymer Thin Films with Electric Fields. *Science (80-.).* **273,** 931–933 (1996).

21. Osuji, C. *et al.* Alignment of self-assembled hierarchical microstructure in liquid crystalline diblock copolymers using high magnetic fields. *Macromolecules* **37,** 9903–9908 (2004).

22. Angelescu, D. E., Waller, J. H., Register, R. A. & Chaikin, P. M. Shear-induced alignment in thin films of spherical nanodomains. *Adv. Mater.* **17,** 1878–1881 (2005).

23. Darling, S. B. Directing the self-assembly of block copolymers. *Prog. Polym. Sci.* **32,** 1152–1204 (2007).

24. Jeong, S. J., Kim, J. Y., Kim, B. H., Moon, H. S. & Kim, S. O. Directed self-assembly of block copolymers for next generation nanolithography. *Mater. Today* **16,** 468–476 (2013).

25. Segalman, R. A., Yokoyama, H. & Kramer, E. J. Graphoepitaxy of spherical domain block copolymer films. *Adv. Mater.* **13,** 1152–1155 (2001).

26. Cheng, J. Y., Mayes, A. M. & Ross, C. A. Nanostructure engineering by templated self-assembly of block copolymers. *Nat. Mater.* **3,** 823–828 (2004).

27. Jung, Y. S. & Ross, C. A. Well-ordered thin-film nanopore arrays formed using a block-copolymer template. *Small* **5,** 1654–1659 (2009).

28. Black, C. T. & Bezencenet, O. Nanometer-scale pattern registration and alignment by directed diblock copolymer self-assembly. *IEEE Trans. Nanotechnol.* **3,** 412–415 (2004).

29. Xiao, S., Yang, X., Edwards, E. W., La, Y.-H. & Nealey, P. F. Graphoepitaxy of cylinder-forming block copolymers for use as templates to pattern magnetic metal dot arrays. *Nanotechnology* **16,** S324–S329 (2005).

30. Park, S. M. *et al.* Directed Assembly of Lamellae- Forming Block Copolymers by Using Chemically and Topographically Patterned Substrates. *Adv. Mater.* **19,** 607–611 (2007).

31. Han, E., Kang, H., Liu, C. C., Nealey, P. F. & Gopalan, P. Graphoepitaxial assembly of symmetric block copolymers on weakly preferential substrates. *Adv. Mater.* **22,** 4325–4329 (2010).

32. Black, C. T. Self-aligned self assembly of multi-nanowire silicon field effect transistors. *Appl. Phys. Lett.* **87,** 1–3 (2005).

33. Bita, I. *et al.* Graphoepitaxy of self-assembled block copolymers on two-dimensional periodic patterned templates. *Science* **321,** 939–43 (2008).

34. Millward, D. B. *et al.* A comparison of the pattern transfer of line-space patterns from graphoepitaxial and chemoepitaxial block co-polymer directed self-assembly. *Proc. SPIE* **9054,** 90540M (2014).

35. Kim, S. O. *et al.* Epitaxial self-assembly of block copolymers on lithographically defined nanopatterned substrates. *Nature* **424,** 411–4 (2003).

36. Ruiz, R. *et al.* Density multiplication and improved lithography by directed block copolymer assembly. *Science* **321,** 936–9 (2008).

37. Cheng, J. K., Rettner, C. T., Sanders, D. P., Kim, H. C. & Hinsberg, W. D. Dense self-assembly on sparse chemical patterns: Rectifying and multiplying lithographic patterns using block copolymers. *Adv. Mater.* **20,** 3155–3158 (2008).

38. Liu, C.-C. *et al.* Fabrication of Lithographically Defined Chemically Patterned Polymer Brushes and Mats. *Macromolecules* **44,** 1876–1885 (2011).

39. Rincon Delgadillo, P. A. Implementation of a chemo-epitaxy flow for directed self-assembly on 300-mm wafer processing equipment. *J. Micro/Nanolithography, MEMS, MOEMS* **11,** 31302 (2012).

40. International Roadmap Committee. *International Technology Roadmap for Semiconductors 2.0 2015 Edition*. (2015).

41. Segal-Peretz, T. *et al.* Characterizing the Three-Dimensional Structure of Block Copolymers via Sequential Infiltration Synthesis and Scanning Transmission Electron Tomography. *ACS Nano* **9,** 5333–5347 (2015).

42. Liu, C.-C. *et al.* Chemical Patterns for Directed Self-Assembly of Lamellae-Forming Block Copolymers with Density Multiplication of Features. *Macromolecules* **46,** 1415–1424 (2013).

43. Detcheverry, F. a., Liu, G., Nealey, P. F. & de Pablo, J. J. Interpolation in the Directed Assembly of Block Copolymers on Nanopatterned Substrates: Simulation and Experiments. *Macromolecules* **43,** 3446–3454 (2010).

44. Hur, S.-M. *et al.* Molecular pathways for defect annihilation in directed self-assembly. *Proc. Natl. Acad. Sci.* **112,** 14144–14149 (2015).

45. Urbas, A. M., Maldovan, M., DeRege, P. & Thomas, E. L. Bicontinuous cubic block copolymer photonic crystals. *Adv. Mater.* **14,** 1850–1853 (2002).

46. Vignolini, S. *et al.* A 3D optical metamaterial made by self-assembly. *Adv. Mater.* **24,** 23–27 (2012).

47. Rose, F., Bosworth, J. K., Dobisz, E. a & Ruiz, R. Three-dimensional mesoporous structures fabricated by independent stacking of self-assembled films on suspended membranes. *Nanotechnology* **22,** 35603 (2011).

48. Chuang, V. P., Cheng, J. Y., Savas, T. a & Ross, C. a. Three-dimensional self-assembly of spherical block copolymer domains into V-shaped grooves. *Nano Lett.* **6,** 2332–7 (2006).

49. Welander, A. M., Craig, G. S. W., Tada, Y., Yoshida, H. & Nealey, P. F. Directed Assembly of Block Copolymers in Thin to Thick Films. *Macromolecules* **46,** 3915–3921 (2013).

50. Liu, G. *et al.* Cross-sectional Imaging of Block Copolymer Thin Films on Chemically Patterned Surfaces. *J. Photopolym. Sci. Technol.* **23,** 149–154 (2010).

51. Sunday, D. F. *et al.* Determination of the internal morphology of nanostructures patterned by directed self assembly. *ACS Nano* **8,** 8426–37 (2014).

CHAPTER 2: POST-DIRECTED-SELF-ASSEMBLY MEMBRANE FABRICATION FOR IN-SITU ANALYSIS OF BLOCK COPOLYMER STRUCTURES

This work was published previously and reproduced in part with permission from: Ren, J.; Ocola, L. E.; Divan, R.; Czaplewski, D. A.; Segal-Peretz, T.; Xiong, S.; Kline, R. J.; Arges, C. G.; Nealey, P. F. *Nanotechnology* **2016**, *27*, 435303. Copyright 2016 IOP Publishing Ltd. (See details in https://doi.org/10.1088/0957-4484/27/43/435303)

2.1 Introduction

Directed self-assembly (DSA) of block copolymers (BCP) can multiply the resolution of conventional lithography and has been studied extensively for the next generation of nanopatterning [1–3]. Great progress has been made in DSA using guide patterns with chemical or topographical contrast to achieve levels of perfection and pattern complexity that enable technological applications. Characterization of DSA-derived features, however, are mostly based on top-down scanning electron microscopy (SEM) imaging and it provides only surface information. Challenges remain to fully characterize and understand the three dimensional (3D) structures throughout the BCP film. Characterization of the through-film structures not only has technological significance in monitoring the DSA process, but can also shed light on the fundamental physics governing BCP DSA.

Several techniques have been demonstrated to reveal the buried structures in BCP films, including: cross-sectional SEM imaging [4,5], transmission electron microscopy (TEM) tomography [6–8] and X-ray scattering [9–11]. Cross-sectional SEM is a surface imaging technique that reveals in-film structures by physically cutting the sample. Complicated milling steps are often required to prepare the surface, and the technique is time-consuming, destructive to the

sample. It produces a small imageable area and may introduce artefacts. In contrast, TEM tomography and X-ray scattering are through-film analysis techniques that can access 3D structures. TEM tomography directly resolves structures in real-space, making it ideal for visualizing complicated morphologies and investigating the details of individual features. X-ray scattering, on the other hand, collects data in reciprocal space, and requires inverse Fourier transform analysis to model the real-space structure. Combining sensitivity with the relatively large footprint of the beam, X-ray scattering is suitable for accurate statistical quantification of the repeating features that are common in BCP DSA, making it a perfect complement to TEM tomography. Among the many forms of X-ray scattering techniques, resonant soft X-ray scattering (RSoXS) is especially attractive for the analysis of BCP thin films due to strong contrast in organic materials without the need for staining and the straight forward data interpretation in transmission geometry [9,8,12]. Unfortunately, as substrate materials strongly absorb electrons and soft X-rays, both TEM tomography and RSoXS require high quality BCP DSA samples on thin (<100 nm) membrane substrates.

The conventional technique for making polymer thin films samples on membranes is by first preparing the BCP film on a thick substrate and then transferring the film to a membrane by either peeling the film off the original substrate or dissolving a sacrificial layer to float the thin film on liquid [9,13–15]. As the film is very thin (<100 nm), however, these processes inevitably cause cracks and wrinkles in the transferred film and introduce undesirable artefacts in the data. The transferring process also makes it hard to align the position and orientation of the DSA pattern with the membrane window, which is important in both characterization techniques. Alternatively, Gotrik *et al.* [7] prepared samples for TEM tomography by directly performing DSA on pre-fabricated membranes, eliminating the transfer process and its related issues. Processing

on thin membranes, however, has its own problems: 1) it is hard to spin-coat uniformly on a membrane sample due to the edge effects of the small frame as well as the topography that is created from the bending of the membrane under the weight of the solution, and 2) the membrane is fragile and easy to break during the many steps of the DSA process.

Considering the advantages and disadvantages of the methods described above, an ideal way to prepare membrane samples would be to complete the DSA process on a thick substrate and then fabricate the membrane in-situ. Stein *et al.* [12] reported such a method using substrates with a three-layer stack of silicon nitride/silicon/silicon nitride and prepared membrane samples for RSoXS by back etching the silicon layer after DSA. The resulting film was uniform and the DSA pattern could be aligned with the membrane window through pre-defined alignment marks. The DSA process in this past work used 1:1 chemical pre-pattern features : assembled features. It only requires control over the surface property of the polystyrene brush, which was done by repeated brush grafting until saturation was achieved as suggested by water contact angle measurements.

Here we extend the approach to a generalizable back etch process to prepare membrane samples of BCP DSA for both TEM tomography and RSoXS. The DSA process studied here is with density multiplication of features, comparable to that which is envisioned for nanomanufacturing today. Surface properties of both the crosslinked guide stripe and the background brush need to be carefully controlled, so repeated grafting is no longer possible. Since most research and applications of BCP lithography are based on silicon substrates, process variations introduced by implementing DSA on silicon nitride versus silicon were investigated and mitigated to ensure that the assembly behaviors were the same on both substrates. A full wafer process was developed to allow layout flexibility and systematic study of DSA parameters.

Finally TEM tomography and RSoXS characterization were demonstrated on the DSA of lamella-forming BCP systems with density multiplication.

2.2 Experimental details

2.2.1 Materials

Silicon wafers (4", N-type, <100> orientation) coated with silicon nitride were purchased from WRS Materials. The wafers were double side polished and the nitride was deposited using low pressure chemical vapour deposition (LPCVD) process with a stress of 150 ± 30 MPa tensile. Wafers for X-ray measurements had a thickness of 535 µm and the nitride thickness was 100 nm. Wafers for TEM tomography had a thickness of 200 µm and the nitride thickness was 30 nm. GL-2000-12 e-beam resist was purchased from Gluonlab and was diluted with anisole v:v = 1:2.5. Microposit S1818 photoresist and 351 developer were purchased from Dow Chemical and used as received. Cross-linkable poly(styrene) (X-PS, AZEMBLY™ NLD128), hydroxyl-terminated poly(styrene-*random*-methyl methacrylate) (P(S-*r*-MMA)-OH) brush (AZEMBLY™ NLD127), and poly(styrene-*block*-methyl methacrylate) (PS-*b*-PMMA, AZEMBLY™ PME312) BCP with L_0 = 28 nm, were synthesized by EMD Performance Materials and used as received [16]. Poly(2-vinylpyridine-*block*-styrene-*block*-2-vinylpyrindine) (P2VP-*b*-PS-*b*-P2VP, M_n = 45 kg/mol, PDI=1.25, L_0 = 21 nm), lamella-forming PS-*b*-PMMA (L3737, 37K-b-37K, PDI = 1.08, L_0 ~40 nm) and hydroxyl-terminated poly(styrene) (PS-OH, M_n = 1.2 kg/mol) were purchased from Polymer Source and used as received. All solvents were purchased from Sigma-Aldrich and used as received.

2.2.2 Sample preparation

Patterning of back side nitride

S1818 photoresist was spin coated at 3000 rpm and baked at 115 °C for 1 min. The resist was then patterned with SUSS MA6 mask aligner to define windows and alignment marks on the backside. The patterned wafer was developed in a v:v = 1:3 mixture of 351 developer and water for 30 sec and rinsed with water. The exposed nitride was then etched and removed with CF_4 plasma (150 W, 160 mTorr, 45 sccm in March CS-1701 RIE with 15.2 nm/min etch rate). The remaining resist was removed with acetone.

Deposition of front side alignment marks

S1818 was spin coated at 3000 rpm on the front side of the wafer and baked at 115 °C for 1 min. Front side alignment marks were aligned to the back side alignment marks using the backside alignment feature on the MA6 aligner. After the front side marks were patterned and developed, 50 nm tungsten was sputtered on to the resist using Emitech K675X and lifted off by immersing in n-methyl-2-pyrrolidone (NMP) at 70 °C for 1 hour.

Directed self-assembly on the front side

The wafer was cleaned with piranha solution (sulfuric acid and hydrogen peroxide v:v = 7:3. *Caution*: piranha solution is an extremely strong oxidizer and should be handled with care) at 130 °C for 3 min. Then an 8 nm X-PS mat was prepared by spin coating NLD128 at 1500 rpm and cross-linking at 270 °C for 30 min. 60 nm GL-2000 resist was coated and baked at 150 °C for 3 min. E-beam patterning was done on JEOL 9300 lithography system using 100 kV accelerating voltage and 1 nA beam current. The sample was developed in n-amyl acetate for 15 sec at room temperature. The pattern was then etched with oxygen plasma (50 W, 10 mTorr, 10 sccm in Oxford PlasmaPro 100 RIE for ~25 sec) to break through the exposed X-PS mat as well as trimming the width of the remaining resist and X-PS stripe to 0.6 L_0 of the polymer. The resist

was then removed by sonication in NMP for 5 minutes for 3 times. Hydroxyl-terminated brush NLD127 was coated at 1500 rpm and annealed at 250 °C for 5 min to graft the brush to the exposed substrate between X-PS guide stripes. Ungrafted brush was then rinsed with toluene. 30 nm of PS-*b*-PMMA PME312 was coated and thermally annealed at 250 °C for 5 min to achieve DSA. For the DSA of P2VP-*b*-PS-*b*-P2VP, PS-OH was used as the backfill brush where it was coated from 0.25 wt% solution in toluene at 1000 rpm and thermally annealed at 200°C for 1 hour. Excess brush was removed by sonication in NMP. Subsequently, the triblock copolymer was spin-coated on the chemical patterns from 1 wt% toluene solution, yielding a 22 nm film. BCP was annealed by solvent vapour annealing using acetone vapour for 1 hour and the swelling ratio was kept at 42% as determined by reflectometry (Filmetrics 60 setup).

Back etch in KOH

After the DSA process, the wafer was placed in a wet etch holder (4" Tandem™ from AMMT) with the front side sealed off by O-rings to protect the BCP film, and only the back side with the windows pattern was exposed. The setup was immersed in 30 wt% KOH solution at 85 °C. The silicon was anisotropically etched at ~85 µm/h until the etching reached the silicon nitride on the front side. The holder was then removed from the KOH solution and rinsed with DI water in a cascade with the wafer inside. Finally the wafer was removed from the holder and dried.

2.2.3 Analysis

Self-assembly of lamella-forming BCP (L3737) was used to determine brush grafting behaviour (fingerprint test). Hydroxyl-terminated brush NLD127 was coated at 1500 rpm and annealed at 250 °C for 5 min to graft the brush. Excess material was removed by sonication in

toluene. 1.9 wt% L3737 in toluene was coated onto the brush at 4000 rpm, yielding a 50 nm film. Thermal annealing was done at 250 °C for 5 min.

TEM tomography was performed using field-emission gun TEM operated at 200 kV (FEI Tecnai F20ST). Tilt series were acquired by tilting the samples to ± 70º with 2-3º intervals. The tilt series were then aligned and reconstructed using FEI software (Inspect 3D^{TM}) to resolve the 3D structure. Thresholding and visualization were performed using FEI software (Amira^{TM}). Sequential infiltration synthesis (SIS) of Al_2O_3 was performed using 3 cycles of alternating exposures to trimethylaluminum and deionized water vapour at 85 °C as previously reported [6]. Subsequently, the polymer was removed using oxygen plasma (50 W, 170 mTorr, 24 sccm, 5 min, March CS-1701 RIE) to obtain alumina nanostructure templated by the BCP.

RSoXS measurements were performed at the Advanced Light Source beam line 11.0.1.2 operating at 285.3 eV. Sample was mounted in transmission geometry, perpendicular to the incident beam. Scattering was collected by a 2D CCD detector and the sample to detector distance was 7.18 cm. The angle between the detector and incident beam was 12° so the direct beam was out of the field of view.

Scanning electron microscopy (SEM) was performed on Carl Zeiss Merlin SEM. X-ray photoelectron spectroscopy (XPS) was acquired on a Kratos Axis 165 with an aluminium filament operated at 12 kV and 10 mA. Film thickness was measured with ellipsometer (J.A.Woollam alpha-SE). Water contact angle was measured by goniometer (Dataphysics OCA15 Plus).

2.3 Results and discussion

2.3.1 Membrane fabrication

A schematic illustration of the process used to fabricate DSA membrane samples in this study is shown in Figure 2-1. The process is based on conventional microfabrication techniques using double-side-polished Si <100> wafers with thin silicon nitride layers deposited on both sides [17]. The thickness of the silicon wafer for RSoXS samples was 535 μm. For TEM tomography, the sample needs to be 3 mm or less in size to fit in the small space inside the microscope and this limits the window size. Therefore, 200 μm thin wafers were used to allow 70° of sample tilt before the edge of the window starts to block the electron beam. The thin wafer was more fragile than the 535 μm wafers and required gentle handling. The thickness of silicon nitride layers was chosen to be 100 nm for RSoXS samples. It allows 45% to 70% X-ray transmission for photon energies from 280 eV to 400 eV and also offers mechanical strength for the membrane. For TEM samples, 30 nm-thick nitride was used for better contrast during imaging. The reduction in mechanical strength for the thin membrane can be compensated by reducing the window size. The silicon nitride was deposited with LPCVD. The resulting nitride film had high density and low stress, so it was resistant to the KOH etching and mechanically robust. Full wafers with 4” diameters were used instead of small chips in order to obtain multiple membrane samples from a single wafer and to systematically study DSA processing parameters while minimizing the process variance.

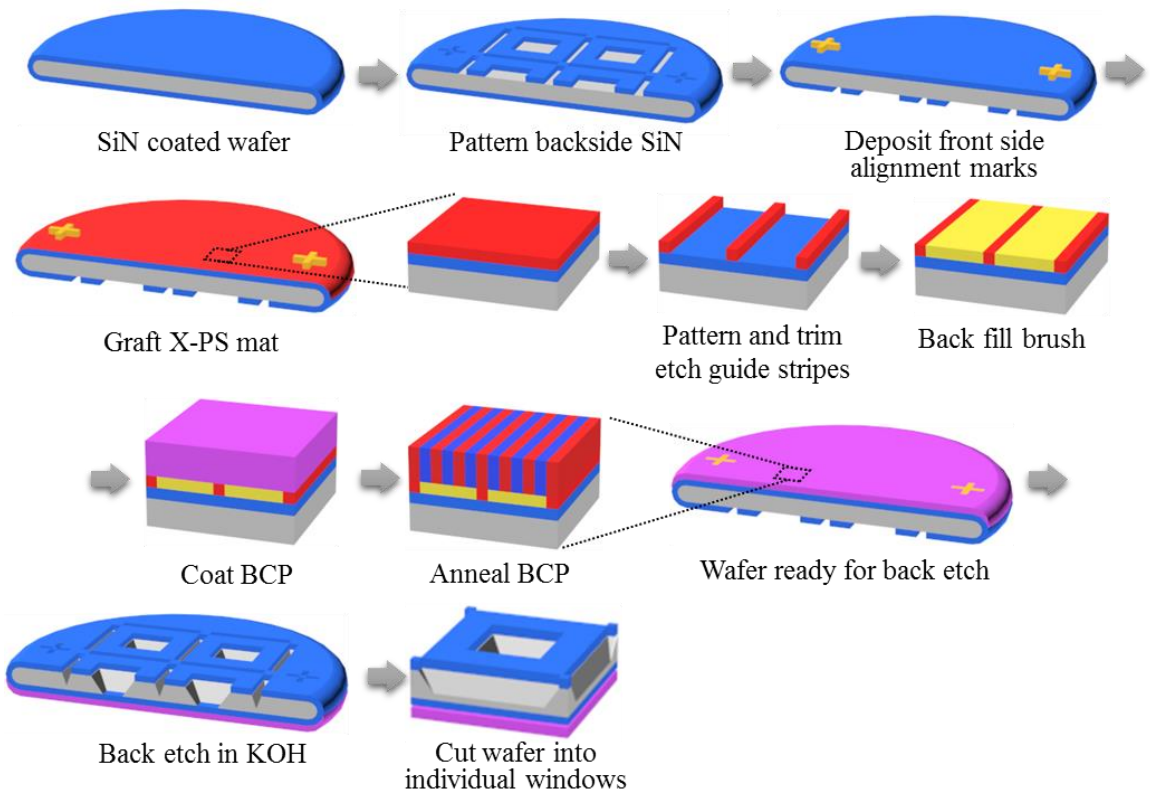

Figure 2-1. Schematic of the back etch process. Si wafer is coated with SiN on both sides. Back side SiN is patterned and etched to define windows. Metal alignment marks are patterned on the corresponding positions on the front through lift-off process. X-PS mat is coated, patterned and trim-etched. Random copolymer brush is then grafted to the exposed areas of the substrate. Block copolymer is coated on the chemical pattern and annealed. After DSA, the wafer is back etched in KOH solution in a sealed holder that protects the front side polymer. After SiN membranes are formed, the etched wafer is cut into individual windows.

The process started with lithographically patterning the silicon nitride on the backside to define a 10 by 10 array of windows (only 4 were shown in the schematic in Figure 2-1 for simplicity). The nitride inside the windows was removed by dry etching using CF_4 plasma. The windows determine the sizes and positions of the final membranes. For RSoXS, the windows were 2.3 mm × 2.3 mm in size. It was chosen so that the final membrane would be 1.5 mm × 1.5 mm to allow 70° tilt. The windows were spaced 5 mm apart, leading to 5 mm × 5 mm frame size for the final membrane. For TEM, the window was 1.3 mm in length to allow tilt angles up to

70° for tomography and only 0.5 mm in width to make up for the lower mechanical strength of the thinner membrane. The width was still large enough considering that the size of a typical TEM image was only ~1 μm^2. The windows were spaced 3 mm from each other so that the 3 mm × 3 mm frames could fit into the TEM. Lines were patterned on the nitride between neighbouring windows. The dimensions of the lines were 4.2 mm × 0.4 mm and 2.2 mm × 0.1 mm for RSoXS and TEM respectively. After backside etching, the lines provide guides to easily cleave the wafer into individual samples. Backside alignment marks were also patterned on the nitride. The backside patterns were aligned with the <110> crystal direction of the silicon wafer to avoid undercutting during wet etching. Tungsten alignment marks were patterned and deposited on the front side through a lift-off process. The front side marks were aligned with the backside patterns and would be used during subsequent e-beam lithography to ensure that the DSA patterns would be positioned over and aligned with the final membranes. The substrate with backside pattern and front side alignment marks was cleaned with piranha solution for 3 minutes. The time was chosen so that the organic contaminants could be removed without damaging the tungsten alignment marks.

Following substrate preparation, chemoepitaxy DSA with density multiplication was carried out on the front side [18,19]. X-PS mat was deposited and annealed, followed by resist coating and e-beam lithography of line and space patterns. The resist patterns were transferred to the X-PS via oxygen plasma etch and an extended etch time was used to further trim the X-PS lines to desired widths. After resist removal, the interspatial regions between X-PS guide lines were functionalized with hydroxyl-terminated random copolymer brush (backfill) so the wetting preference of the background could be adjusted according to the specific BCP system. Block copolymer was coated on to the wafer and annealed to achieve DSA. Guided by the tungsten

alignment marks, the time-consuming e-beam lithography step was only performed on selected areas on the wafer where membranes would be formed, while all the coating, etching and annealing steps were done on the wafer scale so it was highly uniform across all the membranes.

Following the DSA, the wafer was placed into a wet etch holder that sealed-off the polymer side and only exposed the backside with nitride window patterns. The setup was then immersed in an aqueous solution of 30 wt% KOH at 85 °C to etch the silicon. The etching temperature was set well below the glass transition of PS, PMMA and P2VP to prevent any morphology change during the wet etching. As the silicon nitride is resistant to KOH etching, the backside nitride patterning resulted in etching of silicon only within the windows. The etching was also self-limited and would stop as it reached the silicon nitride layer on the front side, forming thin membranes. The KOH etching of silicon is anisotropic and the etch rate in Si <111> direction is negligible compared to the other directions, forming Si (111) side walls with an angle of 54.7° to the wafer surface. Therefore the resulting membranes were smaller in size compared to the original windows on the backside nitride. The membrane size was 1.5 mm × 1.5 mm and 1 mm × 0.2 mm for RSoXS and TEM respectively. Cleave lines were also etched so the wafer could be easily cleaved into individual samples. The width of the cleave line pattern was chosen so that the opposing Si (111) side walls would meet half way into the wafer before reaching the front side nitride, forming grooves to facilitate cleaving. Upon etch completion, the holder was rinsed with water in a cascade rinser. Finally, the wafer was removed from the holder and cut up into individual membrane windows. The front side polymer was perfectly protected by the holder during the etching and was not subjected to any additional processing after DSA.

Pictures of the wafer and individual membranes after etching with polymer on the front side were shown in Figure 2-2. The uniform colour of the BCP film in Figure 2-2a indicates that

the polymer film was perfectly preserved and was uniform across the entire wafer, without any of the damages or artefacts that were reported in conventional membrane sample preparation methods. This full wafer back etch process also allowed flexibility and customizability in the design of membrane windows. The size, thickness and layout of the windows can be easily tuned to satisfy different needs.

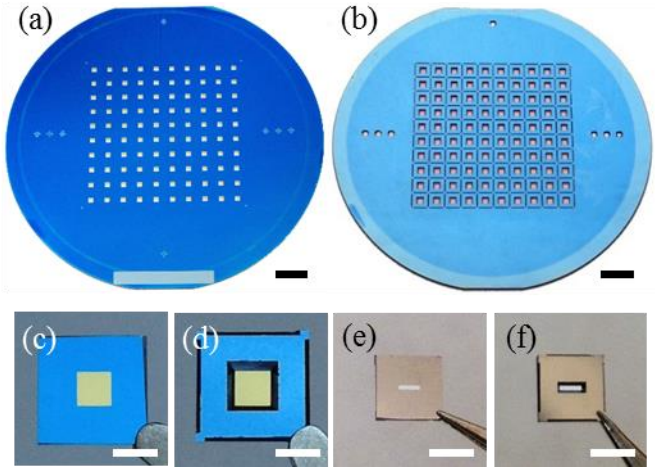

Figure 2-2. SiN membranes with BCP after back etch. Front (a) and back (b) of 4" substrate with 100 membranes for scattering experiments; Front (c) and back (d) of individual membrane cut from the 4" wafer in (a)(b); Front (e) and back (f) of individual membrane for TEM experiments. Scale bars are 10 mm for (a), (b) and 2 mm for (c)-(f).

2.3.2 Chemical pattern fabrication on silicon nitride

Previous studies of chemoepitaxy DSA were mainly based on silicon substrates with native oxide layers. In order to form membranes post-DSA, it is necessary to implement the DSA process on a stack of silicon nitride/silicon/silicon nitride. Having the additional silicon nitride layers could potentially change processing properties as well as properties of the chemical pattern and affect the assembly behaviour. Thus, both e-beam lithography conditions and brush grafting on the silicon nitride stack versus silicon substrate were investigated.

E-beam lithography was used to define the X-PS guide lines. The width and roughness of the guide lines will affect the quality of DSA and need to be carefully controlled through lithography. E-beam lithography of 60 nm pitch line and space patterns was tested on both silicon substrates and silicon nitride stacks with 100 nm silicon nitride layers. The test pattern size was 200 μm, much larger than the typical range of proximity effect on silicon substrates (~30 μm). Therefore all measurements were taken at the centre of each pattern and no proximity effect correction was used. SEM images of the patterns (Figure 2-3a) showed that the patterns on silicon nitride stack were not fully developed at 320 $\mu C/cm^2$ and at 520 $\mu C/cm^2$ the resist lines were starting to break up due to overexposure. In contrast, the patterns on silicon at the same doses had clear and smooth lines. The process latitude, defined as the exposed line width as a function of exposure dose, was measured for both substrates (Figure 2-3b). The process latitude for the silicon nitride stack had a larger slope than for the silicon substrate, i.e. a small change in dose would lead to a large change in line width, making the control of the line width with exposure dose more difficult.

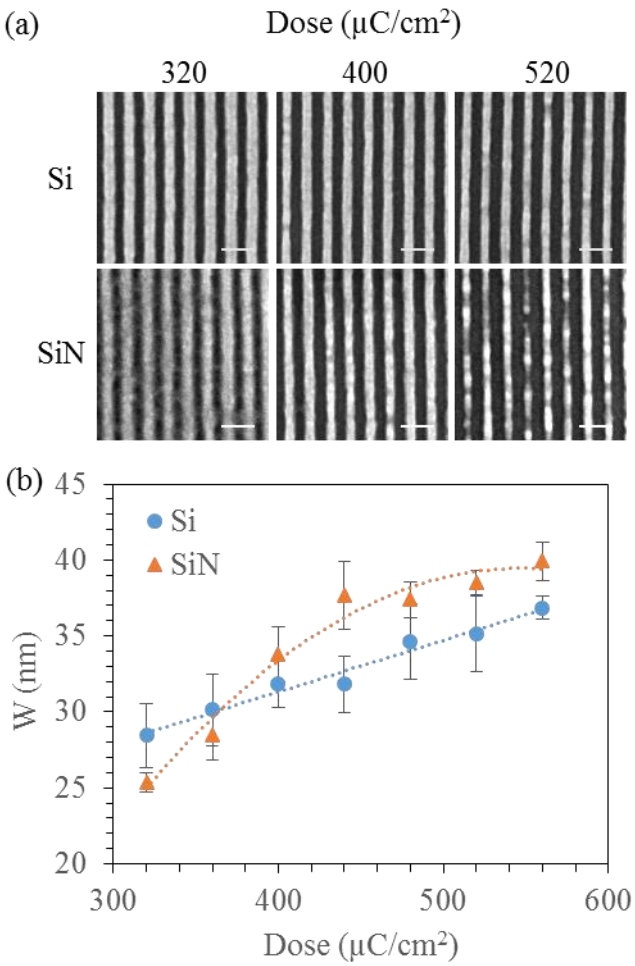

Figure 2-3. Comparison of e-beam lithography on Si substrate and one that is coated with 100 nm SiN. (a) Exposed resist of 60 nm pattern at different doses. Scale bars are 100 nm. (b) Exposure latitude on the two substrates. Error bars represent standard deviation of line width measurements.

Since the incident beam in the exposure tool is invariant, the difference in pattern quality must be caused by the effect of local substrate on the beam when reaching the resist. The narrower process window and steeper process latitude on the silicon nitride stack compared to the silicon substrate was attributed to the deterioration of the beam quality as caused by beam deflection and deformation due to charge accumulation on the substrate. As the wafer stack had non-conductive silicon nitride on both surfaces, it could not be effectively grounded and there would be a charge build up even though the silicon layer in the middle was semiconductive. It's

also possible that the silicon layer in the silicon nitride stack was doped less and had a higher resistivity (5~10 Ω cm) than the silicon substrate (0~0.005 Ω cm) used in this test. The higher resistivity could have led to inefficient dissipation of electrons and caused beam deflection. The effect of charging on pattern quality is consistent with the observation of Zhang *et al.* that the wafer with higher resistivity had lower pattern quality [20]. It should be noted, however, that the charging on the stack was not as severe as on a completely non-conductive substrate such as quartz where entire patterns could be shifted and distorted. To overcome the charging effect, it has been reported that a conductive coating could be applied on the resist to dissipate the charges [21,22]. Here, however, a conductive coating was not necessary. Even though the process window on silicon nitride stacks were narrower, we were still able to fabricate 60 nm pitch line and space patterns, which could be transformed into 10 nm feature size with 3x density multiplication DSA.

Brush grafting in the backfill regions of the chemical pattern is crucial for chemoepitaxy DSA [19,23]. In the DSA process, the brush is grafted after the trim etch step, where the substrate surface has been modified by oxygen plasma. Therefore it is necessary to study the brush grafting behaviour on plasma-treated silicon nitride stack and compare it to that on the plasma-treated silicon substrate. We examined the self-assembly of BCP (fingerprint test) [18,24] on both substrates after oxygen plasma etch under the trim etch condition, using a hydroxyl-terminated non-preferential brush and lamella-forming block copolymer (Figure 2-4). The brush was coated and grafted onto the substrates using the same conditions as the backfill process in DSA (250 °C for 5 min), and excess materials were removed by sonicating in toluene. Then the lamella-forming PS-*b*-PMMA was coated onto the brush and thermally annealed at 250 °C for 5 min (Figure 2-4a). When properly grafted, the interfacial energies between the brush and the blocks

of the copolymer are similar such that the lamellae would assemble perpendicular to the substrate. For both substrates, the typical fingerprint patterns of perpendicular lamella were observed after polymer assembly (Figure 2-4b). The brush grafted onto the plasma-treated nitride also had the same thickness and water contact angle as the one grafted on plasma-treated silicon (Table 2-1). The results suggest that the brush grafting behaviours were the same for both substrates.

Table 2-1. Thickness and water contact angle of grafted brush on plasma-treated substrates. (Mean ± standard deviation of measurements)

	Brush thickness (nm)	Contact angle (°)
Si	6.99 ± 0.06	76.5 ± 0.0
SiN	6.84 ± 0.10	76.4 ± 0.2

Oxygen plasma is known to convert both silicon and silicon nitride to silicon oxide [25,26]. This could be the reason why the silicon nitride stack and the silicon substrate showed the same surface reactivity for brush grafting after oxygen plasma treatment. To support this hypothesis, we studied the atomic composition of the silicon nitride surface using XPS before and after plasma treatment under the trim etch condition (Figure 2-4c). Prior to plasma treatment, Si and N concentrations were stoichiometric 3:4 and there was also 17% of oxygen on the surface. The presence of oxygen could be the result of slow hydrolysis of silicon nitride in atmosphere or during the piranha treatment [27,28]. After plasma etching, the oxygen concentration was almost doubled to 31%, and the amount of nitrogen dropped from 45% to 31% while the silicon concentration remained the same, indicating that the nitrogen atoms were partially replaced with oxygen atoms during plasma treatment and the silicon nitride was converted to oxynitride. Since

XPS was probing ~5 nm into the surface, the oxygen content of the very top layer was probably even higher, close to that of the silicon oxide.

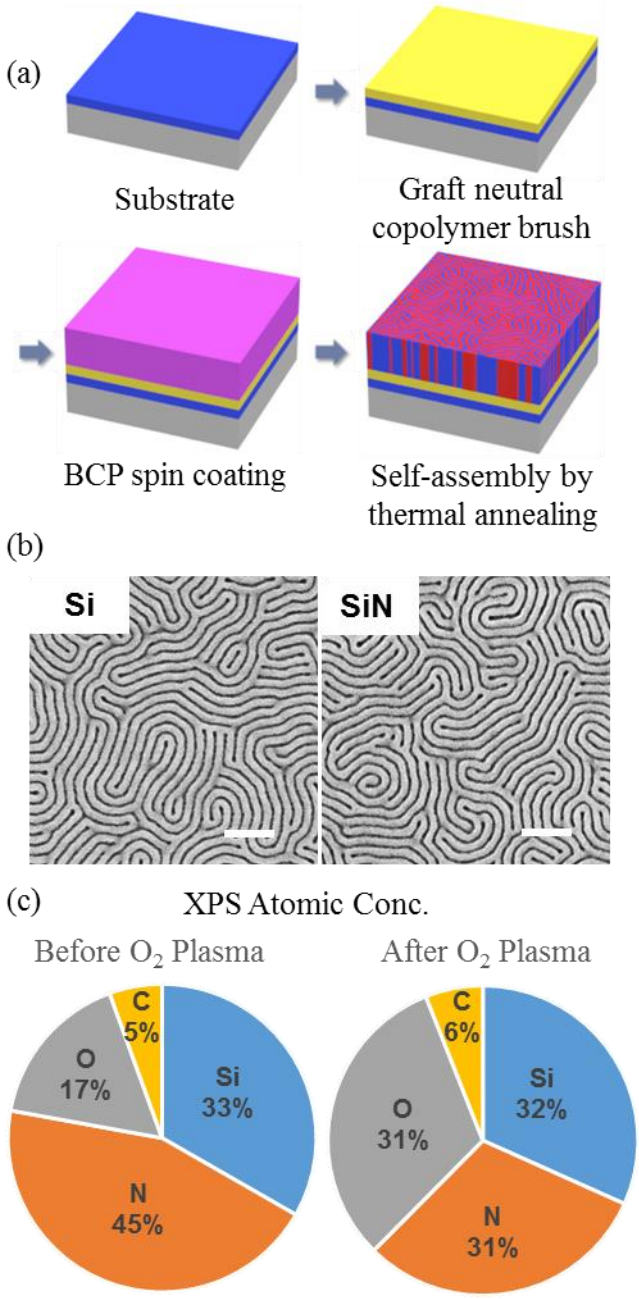

Figure 2-4. Brush grafting on plasma-treated silicon nitride. (a) Process for using self-assembly to test brush grafting. (b) SEM images of self-assembly on plasma-treated silicon and silicon nitride substrates. Scale bars are 200 nm. (c) XPS atomic concentration on SiN surface before and after plasma treatment.

2.3.3 TEM tomography

TEM tomography has been demonstrated as an excellent tool for investigating the three-dimensional structures in block copolymer [6–8]. In TEM tomography, the sample is rotated in the microscope, and a series of 2D projections is collected. The 2D image series is then aligned and back-projected using software to reconstruct the 3D structure. Here, membrane dimensions were designed to enable tilting to ±70°; this high tilt imaging improves the tomography accuracy and minimize missing wedge effects [29]. A picture of the membrane sample mounted onto the tomography sample holder is shown in Figure 2-5a. The holder was custom designed to fit the square frame so the membrane would be automatically aligned and centred. The tilt direction was along the membrane slit.

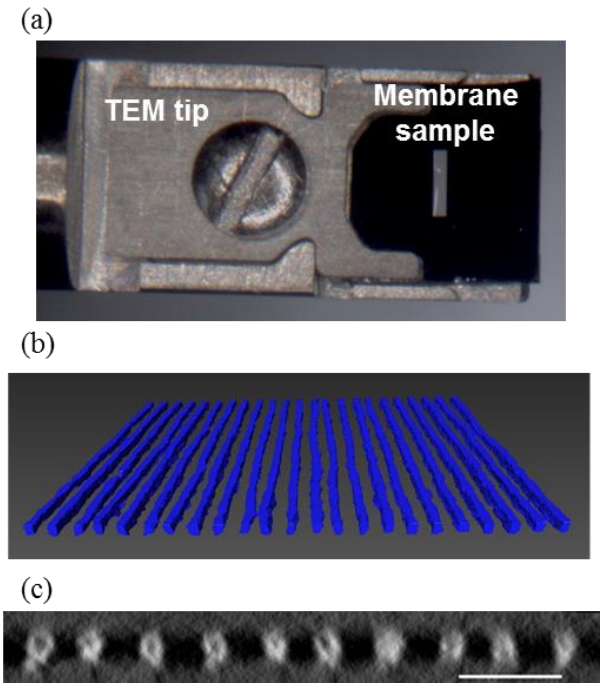

Figure 2-5. TEM tomography of alumina nanostructures templated by the DSA of PS-*b*-PMMA lamella, infiltrated with alumina through SIS, and followed by polymer removal with dry etch. (a) Picture of the TEM membrane fit inside the tomography sample holder. (b) Visualization of the 3D reconstruction of alumina nanostructures. Alumina colored in blue. (c) Digitally-sliced cross-section of the reconstructed volume showing the depth profile. Bright domains represent the alumina nanostructure. Scale bar is 50 nm.

One of the most important application of BCP DSA is as an etch mask to transfer the pattern into silicon substrate. Before pattern transfer, one of the blocks needs to be removed, most commonly through RIE dry etching, which can be challenging for several widely studied DSA systems, such as PS-PMMA and PS-P2VP, due to the relatively low etch contrast between the blocks. An alternative method for pattern transfer, sequential infiltration synthesis (SIS), greatly enhances the etch contrast between the blocks by selectively growing Al_2O_3 in the polar domains of the BCP [30,31]. It is important to understand the alumina nanostructure as it serves as a hard mask and directly determines the quality of pattern transfer.

Figure 2-5b is a 3D visualization of the reconstructed alumina nanostructure (coloured in blue), obtained from TEM tomography of a back-etched membrane sample. A DSA sample with 3x density multiplication was prepared on nitride membrane using PS-*b*-PMMA lamella (L_0 = 28 nm). After DSA, the polymer film was treated with 3 cycles of alumina SIS and was then etched with oxygen plasma to remove all the organics, leaving only the alumina lines. A digitally-sliced cross section of the reconstructed data was presented in Figure 2-5c, showing the structure of individual alumina lamellae (bright domains). The inhomogeneity in the brightness of some of the domains was attributed to non-ideal polymer etching after the SIS process. While most of the alumina nanostructure has a perfect perpendicular profile, some of the alumina features are a bit tilted. The tilting could be due to the collapse of the supporting PMMA scaffolds when the organics were removed by oxygen plasma. Indeed, Ruiz *et al.* also reported the collapsing of the alumina structures after removing the organics, but noted that by tuning the SIS and etching condition this collapse can be prevented and control over the critical dimension of the blocks could be achieved [32]. Combined with the back etch process, TEM tomography provides a non-intrusive way to extract the three dimensional details of BCP structures.

2.3.4 Resonant Soft X-ray Scattering

RSoXS has emerged as a powerful tool for through-film analysis due to the high contrast in signal obtained from the various blocks in the film. In hard X-ray scattering, the contrast is based on electron density. Many important BCP systems, such as PS-b-PMMA and PS-b-P2VP, lack heavy elements and there is little difference in electron density between different blocks, leading to weak signal and contrast in scattering. In RSoXS, on the other hand, the X-ray energy is chosen to be near the absorption edges of light elements where the contrast becomes sensitive to the bonding environments and is greatly enhanced. The contributions from different polymer blocks could also be isolated by tuning to the absorption edges of different elements that are unique to each block [8,33]. PS-P2VP BCP is a high-χ material for the next generation of DSA into sub-10 nm feature size [34,35]. However, due to the similarity in compositions between PS and P2VP, the block copolymer lacks contrast under electron microscopes without staining. The different bonding environments of the two blocks, on the other hand, gave the polymer strong contrast in RSoXS at the carbon absorption edge (285.3 eV), enabling characterization without staining. P2VP-*b*-PS-*b*-P2VP (L_0 = 21 nm) was assembled on a chemical pattern with 84 nm pitch for 4x density multiplication, resulting in 10.5 nm line features. Unlike PS-*b*-PMMA, PS-P2VP BCPs tend to form wetting layer at the free surface during thermal annealing due to large difference in surface energies. Therefore, solvent vapour annealing was used to promote the assembly of perpendicular lamella through the film [36]. After DSA and back etch, the membrane sample was mounted in transmission geometry, perpendicular to the incident beam, as shown in Figure 2-6a. A bonus for using the full wafer back etch process for X-ray scattering experiment was that a large piece with multiple membranes could be mounted to the sample stage so a single alignment was sufficient for multiple samples, saving precious beam time.

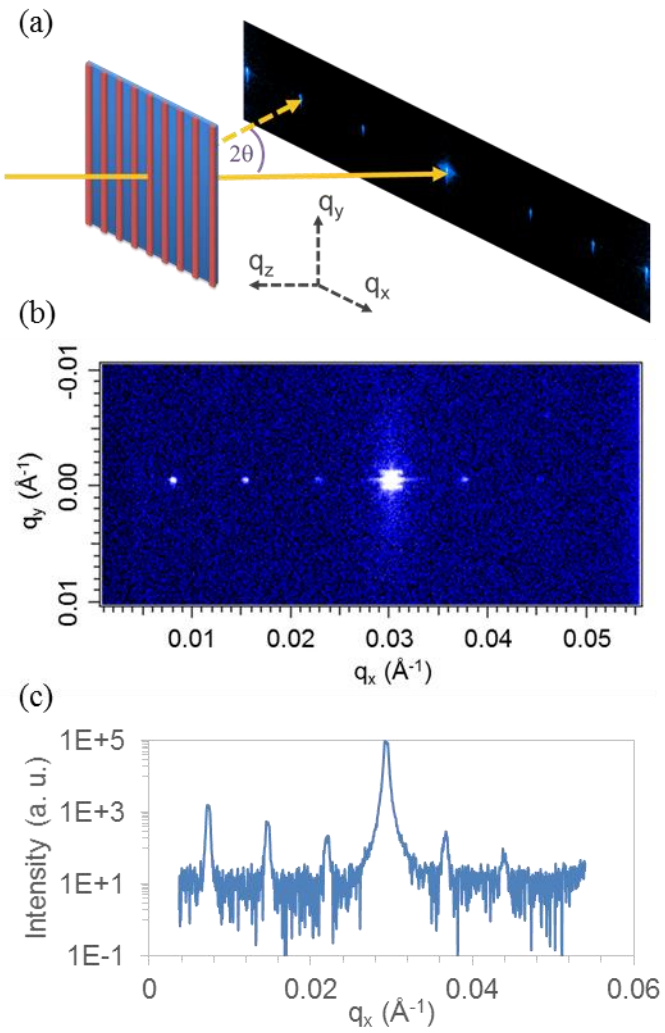

Figure 2-6. RSoXS of P2VP-b-PS-*b*-P2VP lamella 4x DSA using solvent annealing. (a) Schematic of transmission scattering geometry (b) Scattering pattern near the 1st BCP peak showing sharp spots, suggesting perfect DSA. (c) Integrated intensity along scattering peaks.

The scattering pattern, shown in Figure 2-6b, consisted of a set of diffraction spots arranged perpendicularly to the direction of the chemical pattern. Integrated intensity along q_x was shown in Figure 2-6c. The high intensity peak at q_x = 0.03 Å^{-1} was attributed to the 1st order scattering of the block copolymer. The existence of sharp peak instead of a scattering ring or arc indicated that the block copolymer was aligned over the entire illuminated area, which was ~300 µm × 300 µm. The weaker peaks in the scattering corresponded to a periodicity of 84 nm, same

as that of the chemical pattern. The contrast came from the difference in profile and topography between the PS domains on top of guiding stripes and those on background regions. Based on transmission RSoXS, Sunday *et al*. [9,37] have also developed methods to extract the average cross-sections of the BCP lamellae by collecting data from a tilt series of ±70°. This technique provides statistical information that complements TEM tomography and is the object of future investigation.

2.4 Conclusion

In this paper we presented a back etch process to fabricate high quality BCP membrane samples after DSA using a substrate stack of silicon nitride/silicon/silicon nitride layers. Patterning and brush grafting on the stacked substrate were found to be comparable to processing on silicon and DSA with 3x and 4x density multiplication was demonstrated. This generalizable method for membrane fabrication was used to make DSA samples for TEM tomography and RSoXS. Based on this membrane platform, a combination of the 3D visualization power of TEM tomography and the strength of statistical characterization of RSoXS are ready to be harnessed to investigate the materials and processes for BCP DSA, from fundamental to technological implementations.

2.5 References

1. Darling, S. B. Directing the Self-Assembly of Block Copolymers. *Prog. Polym. Sci.* **2007**, *32*, 1152–1204.

2. Bang, J.; Jeong, U.; Ryu, D. Y.; Russell, T. P.; Hawker, C. J. Block Copolymer Nanolithography: Translation of Molecular Level Control to Nanoscale Patterns. *Adv. Mater.* **2009**, *21*, 4769–4792.

3. Hu, H.; Gopinadhan, M.; Osuji, C. O. Directed Self-Assembly of Block Copolymers: A Tutorial Review of Strategies for Enabling Nanotechnology with Soft Matter. *Soft Matter* **2014**, *10*, 3867–3889.

4. Welander, A. M.; Craig, G. S. W.; Tada, Y.; Yoshida, H.; Nealey, P. F. Directed Assembly of Block Copolymers in Thin to Thick Films. *Macromolecules* **2013**, *46*, 3915–3921.

5. Liu, G.; Kang, H.; Craig, G. S. W. .; Detcheverry, F. a. . F.; de Pablo, J. J. .; Nealey, P. F.; Tada, Y.; Yoshida, H. Cross-Sectional Imaging of Block Copolymer Thin Films on Chemically Patterned Surfaces. *J. Photopolym. Sci. Technol.* **2010**, *23*, 149–154.

6. Segal-Peretz, T.; Winterstein, J.; Doxastakis, M.; Ramírez-Hernández, A.; Biswas, M.; Ren, J.; Suh, H. S.; Darling, S. B.; Liddle, J. A.; Elam, J. W.; *et al.* Characterizing the Three-Dimensional Structure of Block Copolymers via Sequential Infiltration Synthesis and Scanning Transmission Electron Tomography. *ACS Nano* **2015**, *9*, 5333–5347.

7. Gotrik, K. W.; Lam, T.; Hannon, A. F.; Bai, W.; Ding, Y.; Winterstein, J.; Alexander-Katz, A.; Liddle, J. A.; Ross, C. a. 3D TEM Tomography of Templated Bilayer Films of Block Copolymers. *Adv. Funct. Mater.* **2014**, *24*, 7689–7697.

8. Wang, C.; Lee, D. H.; Hexemer, A.; Kim, M. I.; Zhao, W.; Hasegawa, H.; Ade, H.; Russell, T. P. Defining the Nanostructured Morphology of Triblock Copolymers Using Resonant Soft X-Ray Scattering. *Nano Lett.* **2011**, *11*, 3906–3911.

9. Sunday, D. F.; Hammond, M. R.; Wang, C.; Wu, W.-L.; Delongchamp, D. M.; Tjio, M.; Cheng, J. Y.; Pitera, J. W.; Kline, R. J. Determination of the Internal Morphology of Nanostructures Patterned by Directed Self Assembly. *ACS Nano* **2014**, *8*, 8426–8437.

10. Mahadevapuram, N.; Strzalka, J.; Stein, G. E. Grazing-Incidence Transmission Small Angle X-Ray Scattering from Thin Films of Block Copolymers. *J. Polym. Sci. Part B Polym. Phys.* **2013**, *51*, 602–610.

11. Gu, X.; Gunkel, I.; Hexemer, A.; Gu, W.; Russell, T. P. An In Situ Grazing Incidence X-Ray Scattering Study of Block Copolymer Thin Films During Solvent Vapor Annealing. *Adv. Mater.* **2014**, *26*, 273–281.

12. Stein, G. E.; Liddle, J. A.; Aquila, A. L.; Gullikson, E. M. Measuring the Structure of Epitaxially Assembled Block Copolymer Domains with Soft X-Ray Diffraction. *Macromolecules* **2010**, *43*, 433–441.

13. Park, S.-M.; Craig, G. S. W.; La, Y.-H.; Nealey, P. F. Morphological Reconstruction and Ordering in Films of Sphere-Forming Block Copolymers on Striped Chemically Patterned Surfaces. *Macromolecules* **2008**, *41*, 9124–9129.

14. Han, E.; Stuen, K. O.; Leolukman, M.; Liu, C.-C.; Nealey, P. F.; Gopalan, P. Perpendicular Orientation of Domains in Cylinder-Forming Block Copolymer Thick Films by Controlled Interfacial Interactions. *Macromolecules* **2009**, *42*, 4896–4901.

15. Stein, G. E.; Kramer, E. J.; Li, X.; Wang, J. Layering Transitions in Thin Films of Spherical-Domain Block Copolymers. *Macromolecules* **2007**, *40*, 2453–2460.

16. Rincon Delgadillo, P. A.; Craig, G. S. W.; Gronheid, R.; Nealey, P. F. Scale-up of a Chemo-Epitaxy Flow for Feature Multiplication Using Directed Self- Assembly of Block-Copolymers. *J. Photopolym. Sci. Technol.* **2013**, *26*, 831–839.

17. Franssila, S. *Introduction to Microfabrication*; John Wiley & Sons, Ltd: Chichester, UK, 2010.

18. Liu, C.-C.; Han, E.; Onses, M. S.; Thode, C. J.; Ji, S.; Gopalan, P.; Nealey, P. F. Fabrication of Lithographically Defined Chemically Patterned Polymer Brushes and Mats. *Macromolecules* **2011**, *44*, 1876–1885.

19. Liu, C.-C.; Ramírez-Hernández, A.; Han, E.; Craig, G. S. W.; Tada, Y.; Yoshida, H.; Kang, H.; Ji, S.; Gopalan, P.; de Pablo, J. J.; *et al.* Chemical Patterns for Directed Self-Assembly of Lamellae-Forming Block Copolymers with Density Multiplication of Features. *Macromolecules* **2013**, *46*, 1415–1424.

20. Zhang, J.; Fouad, M.; Yavuz, M.; Cui, B. Charging Effect Reduction in Electron Beam Lithography with nA Beam Current. *Microelectron. Eng.* **2011**, *88*, 2196–2199.

21. Mohamed, K.; Alkaisi, M. M.; Blaikie, R. J. Surface Charging Suppression Using PEDOT/PSS in the Fabrication of Three Dimensional Structures on a Quartz Substrate. *Microelectron. Eng.* **2009**, *86*, 535–538.

22. Muhammad, M.; Buswell, S. C.; Dew, S. K.; Stepanova, M. Nanopatterning of PMMA on Insulating Surfaces with Various Anticharging Schemes Using 30 keV Electron Beam Lithography. *J. Vac. Sci. Technol. B Microelectron. Nanom. Struct.* **2011**, *29*, 06F304.

23. Rincon Delgadillo, P. a.; Gronheid, R.; Lin, G.; Cao, Y.; Romo, A.; Somervell, M.; Nafus, K.; Nealey, P. F. Process Sensitivities in Exemplary Chemo-Epitaxy Directed Self-Assembly Integration. In *Proc. of SPIE*; Tong, W. M.; Resnick, D. J., Eds.; 2013; Vol. 8680, p. 86801H.

24. Huang, E.; Pruzinsky, S.; Russell, T. P.; Mays, J.; Hawker, C. J. Neutrality Conditions for Block Copolymer Systems on Random Copolymer Brush Surfaces. *Macromolecules* **1999**, *32*, 5299–5303.

25. Jime´nez, C.; Perrie`re, J.; Vickridge, I.; Enard, J. P.; Albella, J. M. Transformation of Silicon Nitride in Oxygen Plasma. *Surf. Coatings Technol.* **1991**, *45*, 147–154.

26. Kennedy, G. P.; Buiu, O.; Taylor, S. Oxidation of Silicon Nitride Films in an Oxygen Plasma. *J. Appl. Phys.* **1999**, *85*, 3319.

27. Liao, W.; Lin, C.; Lee, S. Oxidation of Silicon Nitride Prepared by Plasma-Enhanced Chemical Vapor Deposition at Low Temperature. *Appl. Phys. Lett.* **2001**, *65*, 2229–2231.

28. Chiang, J. N.; Ghanayem, S. G.; Hess, D. W. Low-Temperature Hydrolysis (Oxidation) of Plasma-Deposited Silicon Nitride Films. *Chem. Mater.* **1989**, *1*, 194–198.

29. *Electron Tomography*; Frank, J., Ed.; Springer US: Boston, MA, 1992.

30. Peng, Q.; Tseng, Y. C.; Darling, S. B.; Elam, J. W. A Route to Nanoscopic Materials via Sequential Infiltration Synthesis on Block Copolymer Templates. *ACS Nano* **2011**, *5*, 4600–4606.

31. Tseng, Y. C.; Mane, A. U.; Elam, J. W.; Darling, S. B. Enhanced Lithographic Imaging Layer Meets Semiconductor Manufacturing Specification a Decade Early. *Adv. Mater.* **2012**, *24*, 2608–2613.

32. Ruiz, R.; Wan, L.; Lille, J.; Patel, K. C.; Dobisz, E.; Johnston, D. E.; Kisslinger, K.; Black, C. T. Image Quality and Pattern Transfer in Directed Self Assembly with Block-Selective Atomic Layer Deposition. *J. Vac. Sci. Technol. B Microelectron. Nanom. Struct.* **2012**, *30*, 06F202.

33. Wang, C.; Hexemer, A.; Nasiatka, J.; Chan, E. R.; Young, a T.; Padmore, H. a; Schlotter, W. F.; Lüning, J.; Swaraj, S.; Watts, B.; *et al.* Resonant Soft X-Ray Scattering of Polymers with a 2D Detector: Initial Results and System Developments at the Advanced Light Source. *IOP Conf. Ser. Mater. Sci. Eng.* **2010**, *14*, 12016.

34. Yoshida, H.; Suh, H. S.; Ramirez-Hernandez, A.; Lee, J. I.; Aida, K.; Wan, L.; Ishida, Y.; Tada, Y.; Ruiz, R.; de Pablo, J.; *et al.* Topcoat Approaches for Directed Self-Assembly of Strongly Segregating Block Copolymer Thin Films. *J. Photopolym. Sci. Technol.* **2013**, *26*, 55–58.

35. Sun, Z.; Chen, Z.; Zhang, W.; Choi, J.; Huang, C.; Jeong, G.; Coughlin, E. B.; Hsu, Y.; Yang, X.; Lee, K. Y.; *et al.* Directed Self-Assembly of Poly(2-Vinylpyridine)- B -Polystyrene- B -poly(2-Vinylpyridine) Triblock Copolymer with Sub-15 Nm Spacing Line Patterns Using a Nanoimprinted Photoresist Template. *Adv. Mater.* **2015**, *27*, 4364–4370.

36. Nealey, P. F.; Wan, L. Solvent Annealing Block Copolymers on Patterned Substrates. 20120202017, 2012.

37. Sunday, D. F.; Hammond, M. R.; Wang, C.; Wu, W.; Kline, R. J.; Stein, G. E. Three-Dimensional X-Ray Metrology for Block Copolymer Lithography Line-Space Patterns. *J. Micro/Nanolithography, MEMS, MOEMS* **2013**, *12*, 31103.

CHAPTER 3: QUANTITATIVE THREE DIMENSIONAL CHARACTERIZATION OF BLOCK COPOLYMER DIRECTED SELF -ASSEMBLY ON COMBINED CHEMICAL AND TOPOGRAPHICAL PRE-PATTERNED TEMPLATES

This work was published previously and reproduced in part with permission from: Segal-Peretz, T.; Ren, J.; Xiong, S.; Khaira, G.; Bowen, A.; Ocola, L. E.; Divan, R.; Doxastakis, M.; Ferrier, N. J.; de Pablo, J.; *et al. ACS Nano* **2017**, *11*, 1307–1319. (See details in http://doi.org/10.1021/acsnano.6b05657)

3.1 Introduction

In recent years, as the feature size in nanomanufacturing has scaled down into the sub-20 nm regime, approaches such as self-aligned double and quadruple pattering,[1-3] and directed self-assembly (DSA) of block copolymers (BCP)[4-5] were developed in order to extend patterning capabilities beyond the resolution limits of conventional optical lithography tools. In all these processes, there is a need for tight control over the feature size, the feature's three-dimensional (3D) profile, and over the fluctuation of the feature's size and shape to meet stringent manufacturing constraints for semiconductors. Probing and understanding the three-dimensional morphology of the pattern is therefore important for the development of new materials and processes in nanomanufacturing.

In DSA, BCPs are directed to assemble by chemical or topographical pre-pattern templates in a bottom-up process.[4, 6] Thus, probing the 3D morphology of BCP DSA is necessary not only for determining the exact structure of the DSA film, but to enable better understanding of the relationship between the guiding pattern and the final assembled film. In general, the final 3D morphology of a DSA film is determined by the BCP chemistry, together with the guiding

pattern geometry and chemistry, and the processing conditions.[6-7] It's therefore desirable to obtain a detailed correlation between all these parameters and the DSA film morphology.

Besides controlling the through-film morphology and the features' fluctuations, DSA films should also exhibit defectivity levels that are compatible with the semiconductor industry (~1 defect per 100 cm^2 area) in order to be implemented in manufacturing. To achieve this low defectivity level, the origins of DSA defects should be better understood.[8-10] However, optical metrology tools and scanning electron microscopy (SEM), which are routinely used for defect detection and process window evaluation, cannot detect defects which are hidden underneath the BCP surface and might over predict the process window.[11-12] These defects often become apparent only after the pattern transfer process, and tracing their origin is challenging since both the BCP layer and the pattern transfer process can contribute to its formation. Indeed, both Gronheid *et al.*[12] and Wan *et al.*[13] reported that defects which were not identified after BCP DSA, appeared at the end of the pattern transfer process. Thus, probing the local BCP structure in 3D assists in identifying hidden defects, while mapping their 3D structure can shed light on their origin.

Two main 3D characterization techniques of BCP thin films have been demonstrated in the last few years. The first is based on reciprocal space characterization using X-ray scattering demonstrated by Stein *et al.*[14] and by Sunday *et al.*[15-16] X-ray scattering is a powerful technique which probes large-area samples with sub-nm resolution. It relies on high intensity scattering from periodic features, providing valuable statistical information on the average structure and fluctuations in structure from macroscopic areas. However, X-ray scattering requires a model to derive the structure from reciprocal space data, and provides limited information about individual BCP features and non-periodic structures such as defects. The second 3D

characterization technique is based on real space characterization using transmission electron microscope (TEM) tomography. Although sampling size is limited in TEM, it is considered a powerful technique for BCP DSA metrology,[17] providing the data necessary for understanding BCP assembly in 3D,[18-19] for studying defect formation,[9, 19] and for validating molecular simulations.[18-19] The relatively straight-forward interpretation of TEM tomography data, and recent progress in sample preparation,[17] make it an attractive method for probing the structure BCP DSA films. Moreover, since TEM tomography is a real-space characterization method, it is possible to decouple the average shape of the structure (in the field of view) from the positional fluctuation of the shape, and measure them independently.

Here we develop in-depth understanding of the through-film structure, fluctuation in structure, and defects in DSA films of high-χ (Flory-Huggins interaction parameter), solvent vapor annealed (SVA), poly(2-vinylpyridne)-*b*-polystyrene-*b*-poly(2-vinylpyridne) (P2VP-*b*-PS-*b*-P2VP) triblock copolymer, through scanning TEM (STEM) tomography and theoretically informed coarse-grain (TICG) simulations results. SVA is known to mitigate the differences in interfacial energies at the film's free surface and enable sub-10 nm DSA,[20-26] while P2VP-*b*-PS-*b*-P2VP has high χ (0.18 at room temperature),[27-28] and was recently shown to be directed into highly ordered patterns.[21, 24, 26, 29] The effect of the template's dimensions on the 3D BCP structure was investigated by systematically changing the width of the guiding stripes from 0.7 $L_{0,s}$ to 1.9 $L_{0,s}$ in 4x density multiplication pre-pattern pattern, where $L_{0,s}$ is self-assembled period of the polymer after undergoing the SVA process. A combination of tomographic characterization and TICG simulations revealed that two regimes of guide stripe width lead to aligned assembly at the top of the film. However, the internal BCP structure in these regimes is significantly different in terms of assembly on the top and sides of the cross linked polystyrene

(X-PS) guiding stripes, the curvature of the assembled lamellae in the through-film structure, and the defect levels at the BCP-template interface. The 3D characterization also showed that the topography of the pre-pattern template plays a strong role in the assembly in terms of the level of alignment and defect formation. Analysis of the fluctuation of the interface between PS and P2VP domains revealed that the interface positional fluctuation depends on the location of the domains with respect to the underlying template and on the distance away from the free surface of the film and the substrate. Moreover, by quantifying the 2D shape of the domains and their positional fluctuations, we were able to probe the compositional profile of the domain interface. Finally, STEM tomography characterization enabled us to probe the 3D structure of common defects such as micro-bridge defect and line breakage defects, giving insights to their origins.

3.2 Results and discussion

3.2.1 BCP DSA for 3D characterization

Samples were prepared for TEM imaging and tomography according to the procedure illustrated in Figure 3-1. Detailed description can be found in the experimental section and in previous reports.[17] In short, 4" SiN_x/Si/SiN_x (30 nm/200 μm/30 nm) wafers were patterned on the back side using optical lithography to define openings in the back SiN_x that would later serve as an etching mask to create individual SiN_x windows. Then, templates consisting of X-PS mats and hydroxyl terminated polystyrene brushes (PS-OH) were fabricated using the Liu-Nealey (LINE) flow on the front side of the SiN_x/Si/SiN_x wafer (Figure 3-1a).[7] The X-PS guiding stripes were fabricated using ebeam lithography and oxygen-plasma etch. The etch processes exposes the X-PS sidewalls to oxygen plasma, leading to different chemistry between the sidewalls and top surface of the X-PS guide stripes.[30] The oxidized sidewalls of the guide stripes were

preferential for the more polar block of the polymer, in this case P2VP, and the protected top surface was preferential for PS. Low molecular weight (1.2k) PS-OH brush, which has been shown to induce P2VP-*b*-PS-*b*-P2VP perpendicular domains in self-assembly films, was grafted on the exposed substrate sections, and presumably and to a lesser extent to the X-PS sidewalls. The modified sidewalls remained P2VP preferential and together with the non-preferential background and PS preferential guide stripe formed a three-tone chemistry. The period ($L_{0,s}$) of P2VP-*b*-PS-*b*-P2VP in the solvated but micro-phase separated state under the SVA conditions used in this study was 21.3 nm, as determined by grazing incident small angle X-ray (GISAXS) measurement of SVA self-assembled films. Therefore, the pitch of the template (L_s) was designed to be 84 nm, for DSA with 4 X density multiplication. In addition, the templates had ~ 5 nm topography (~ 0.25 $L_{0,s}$), with ~ 7 nm thick X-PS guiding stripes, and ~ 2 nm thick PS-OH brush background. The role of topography in template will be discussed in the following section. To study the effect of the template geometry on the 3D structure of BCP film, the guiding stripe width, W, was varied between 1.9 $L_{0,s}$ and 0.7 $L_{0,s}$ by changing the exposure dose. The geometry of the X-PS guiding stripes was determined after photoresist removal using atomic force microscopy (AFM) measurements.

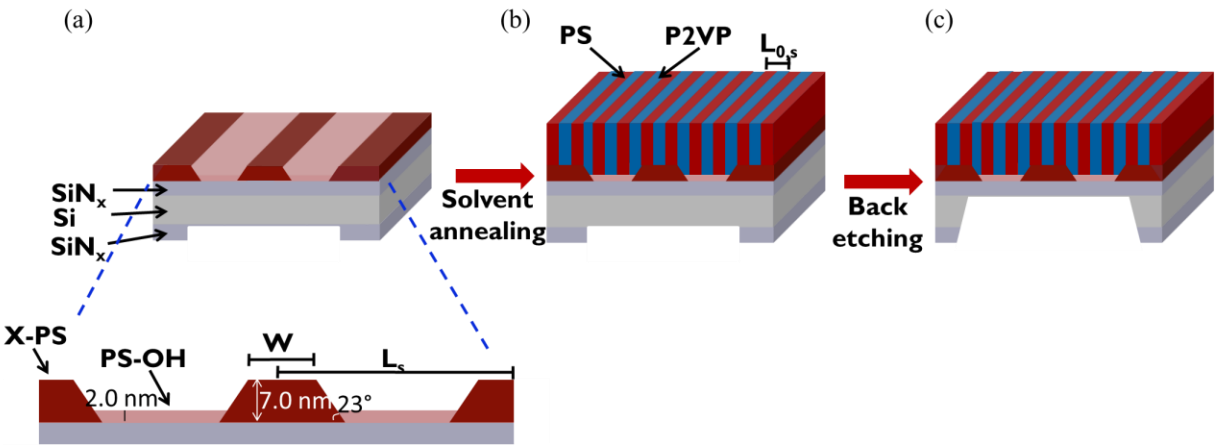

Figure 3-1. Schematic illustration of sample preparation process. (a) Pre-pattern templates were fabricated on SiNx/Si/SiNx 4" wafer. (b) P2VP-b-PS-b-P2VP was directed self-assembled on the templates using acetone solvent vapor annealing. (c) The silicon wafer was back etched to create windows for TEM imaging.

Following the template fabrication, 25 nm thick P2VP-*b*-PS-*b*-P2VP film was spin cast on the wafer and annealed using acetone SVA for 60 min (Figure 3-1b). Acetone is considered a non-selective solvent to both PS and P2VP blocks, and therefore it mitigates the difference in surface energies between the blocks during the SVA process, enabling assembly of perpendicularly oriented lamellae.[24, 26] The swelling ratio of the polymer film ((swollen film thickness- non-swollen thickness)/ non-swollen thickness) was kept at 42 % during the SVA process and was returned to ~2 % during the rapid drying step. Under these conditions, the BCP assembles in the highly mobile solvated but micro-phase separated state.[26] The solvated PS and P2VP blocks recognize the template chemistry and topography, leading to well-aligned morphologies.[20] Swelling is not expected to affect the template topography as the X-PS guide stripes were highly crosslinked and the background brush was very thin (2 nm). Upon rapid solvent removal, the domains shrink in the direction normal to the substrate and retain their lateral dimensions in the plane of the film.[31] Following the DSA, the silicon substrate was back

etched through the openings defined on the back side using KOH wet etching procedure for ~ 2 hours, forming 200 µm x 1mm windows of BCP/ SiN_x windows (Figure 3-1c).

Before TEM imaging, samples were stained for 2 hours using iodine vapors. Iodine forms a complex with the P2VP pyridine group, enhancing electron scattering from the P2VP domains.[32] Although the kinetics of iodine staining is unknown, our experience suggests that 2 hours of staining of 25 nm thick film could reach staining saturation. *i.e.* all the available pyridine groups are stained.

3.2.2 Through-film structure of BCP DSA films

In order to decipher the three dimensional morphology, STEM tomography characterization was performed. For each sample, a tilt series of 51 images with tilt angles ranging from -68° to +68° was acquired, followed by alignment and reconstruction, resulting in a reconstructed volume of roughly 850 nm x 850 nm x 40 nm (*x,y,z*). Visualization of the reconstructed volume of P2VP-*b*-PS-*b*-P2VP DSA films on the templates with varying X-PS guide stripes width are shown at high magnification in the left column of Figure 3-2. For clarity, P2VP domains in the visualization images are colored in blue while PS domains are transparent. Corresponding *xy* slices, parallel to the substrate, from close to the top of the film ($z \approx 22$ nm), and close to the bottom of the film ($z \approx 5$ nm) obtained from the reconstructed volumes are shown in the central column. Bright domains in the STEM images correspond to iodine-stained P2VP domains and will be referred to as P2VP domains, while dark domains correspond to PS domains. To quantify the through-films morphology in the films, each reconstructed volume was digitally sliced to 0.48 nm thick *xz* cross sections (the number of cross section varied between 1700 and 1900, according to the size of the reconstructed volume). The individual cross sections from each volume were averaged along the *y* direction to obtain high signal to noise images. The

averaged cross sections are presented in Figure 3-2 on the right column together with an illustration of a single X-PS guide stripe (in dark red) to assist the interpretation of the data.

The tomographic data shows that the degree of alignment changes with the width of the guiding stripes. Two regimes (processes windows) of aligned assembly can be identified: the first is around W = 1.5 $L_{0,s}$, where templates with W = 1.6 $L_{0,s}$ and W = 1.4 $L_{0,s}$ direct the BCP into aligned lamellae (Figure 3-2b and 2c, respectively). In this regime, three lamellae assemble on the top of the guiding stripe (two PS lamellae and one P2VP lamellae), while the X-PS side walls are wetted by P2VP lamellae, as can be seen in the averaged cross sections. Templates with wider X-PS guiding stripes (W = 1.9 $L_{0,s}$) or narrower X-PS guiding stripes (W = 1.1 $L_{0,s}$) result in a non-aligned morphology (Figure 3-2a and 2d, respectively). The second regime of aligned assembly was identified in templates with X-PS guiding stripes width of 0.8 $L_{0,s}$ and 0.7 $L_{0,s}$ (Figure 3-2e and 2f, respectively). In this regime, only one PS lamellae assembles on the top of the guiding stripe and the adjacent P2VP lamellae assemble on the X-PS side walls. Similar regimes were also seen in the assembly of PS-*b*-poly methyl methacrylate (PS-*b*-PMMA) on pre-pattern templates.[33]

The tomographic characterization probes the detailed 3D structure of each assembled film. When the X-PS width is tuned to 1.6 $L_{0,s}$ and 1.4 $L_{0,x}$, vertical through-film domains are obtained (Figure 3-2b and 2c). The *xy* slices (central column) and the full *xy* slice series of P2VP-*b*-PS-*b*-P2VP DSA film on template with W=1.4 $L_{0,s}$ show that one lamella in every four P2VP lamellae "disappears" towards the bottom of the film. Thus, while at the top of the film (Figure 3-2b and 2c, central column, $z \approx 22$ nm), and through most of the film thickness there are four lamellae in every template pitch (L_s), only three lamellae are seen in each L_S near the BCP-template interface (Figure 3-2b and 2c, central column, $z \approx 5$ nm). The origin of this assembly is

the topography of the template, where the ~ 5 nm difference in height between the X-PS guide stripe and the PS-OH brush results in height variation in the assembly of the lamellae according to their location. The template topography creates two P2VP lamellae populations: P2VP lamellae that assembled on top of the X-PS guiding stripe ($P2VP_G$), and P2VP lamellae that assembled on the PS-OH brush or on the PS-OH brush-PS guide stripe interface ($P2VP_B$, Figure 3-2b and 2c, right column). Measurements of the *z* length of each population in the averaged cross section (Figure 3-2c, right column) corroborate that there is ~ 5 nm *z* length difference between the two populations. The two lamellae populations also differ in their brightness intensity; in both the single cross sections and in the averaged cross sections, $P2VP_G$ has lower brightness than $P2VP_B$. This was attributed to lower scattered electron detection by the annular STEM detector due to the X-PS that is present below the $P2VP_G$.

When the width of the X-PS is tuned to W=1.9 $L_{0,s}$ and W=1.1 $L_{0,s}$, non-aligned lamellae are assembled due to the mismatch between W and BCP domain size (Figure 3-2a and 2d). Interestingly, even near the interface with the brush domain, where there is geometrical constraint of the X-PS guide stripes, the lamellae are still non-aligned or only partly-aligned, as can be seen in Figure 3-2a and 2d – central column, $z \approx 5$ nm. The non-aligned assembly results in blurred averaged cross sections (Figure 3-2a and 2d, right column) due to the variety of orientations of the BCP. The difference in blurriness within these cross sections corresponds to the percentage of misalignment in the particular area where the tomography and averaging were performed.

When W is further decreased to 0.8 $L_{0,s}$, aligned assembly is obtained but the films had higher defect levels than what was observed in the first aligned regime. In this regime, the tomographic characterization reveals an interesting phenomenon; while aligned lamellae are seen

at the top of the film (Figure 3-2e, central column, $z \approx 22$ nm) and this assembly would probably be deemed as satisfactory aligned assembly in top-down imaging, there is significant deviation between the assembly at the top and the assembly at the bottom of the film; many defects appear close to the interface the BCP and the brush (Figure 3-2e, central column, $z \approx 5$ nm), and curved lamellae are observed in the averaged cross section (Figure 3-2e, right column). These defects are formed at the bottom 5 nm of the film, between the X-PS guide stripes, as can be seen from the full *xy* slice series. Assembly directed by templates with W=0.7 $L_{0,s}$ showed similar behavior (Figure 3-2f), and the differences between the two morphologies will be discussed shortly. Despite the defects at the bottom of the film, averaged cross sections show uniform structures along the *y* axis (Figure 3-2e and 3f, right column, respectively). These averaged cross sections reveal a significant difference between the two P2VP lamellae populations in these films: the external P2VP lamellae in the L_s repeating unit (P2VP-side; $P2VP_S$) and the two central lamellae in the L_s repeating unit (P2VP-center; $P2VP_C$). At the top two thirds of the film, all lamellae form perpendicular morphology. However, at the bottom third of the film thickness, $P2VP_s$ curve and become narrower at the brush-BCP interface, while $P2VP_C$ remain relatively straight and with constant width. Comparison between the assemblies at W=0.8 $L_{0,s}$ and W=0.7 $L_{0,s}$ shows that the curvature of $P2VP_S$ is dependent on the template's geometry. While $P2VP_C$ are straight in both cross sections, the curvature of $P2VP_S$ is larger in the assembled film with W=0.8 $L_{0.s}$ (Figure 3-2e, right column) compared to the assembled film with 0.7 $L_{0,s}$ (Figure 3-2f, right column).

Several conditions could have contributed to the defects formation and the thin, curved, lamellae observed at the bottom of the film. First, the preferred wetting of the side walls by P2VP together with the width of the brush regions of the template imposed a spatial constraint on the assembly, *i.e.* the brush region was not wide enough to accommodate four P2VP and three

PS lamellae. Indeed, when the brush region was wider at W=0.7 $L_{0,s}$, the curvature of $P2VP_S$ was reduced. Second, a gradient in the solvent evaporation during the drying step in the SVA process could have created volume fraction constraints that can lead to thin P2VP domains where there is preferred wetting (X-PS sidewalls). We anticipate that if W were decreased to 0.5 $L_{0,s}$, the $P2VP_S$ curvature would be further decreased and non-defective, perpendicular and aligned lamellae would be assembled.

Importantly, the effect of the morphologies seen in Figure 3-2e and 2f on the pattern transfer of the BCP film has not been explored yet. There is a concern that these BCP patterns will be categorized as aligned assembly by top-down meteorology tools but would lead to defective lines after the pattern transfer process. In addition, placement errors and variation in pattern width can occur due to the curved lamellae at the bottom of the film.

To gain insight into the BCP-template interactions and to quantify their role in DSA, TICG simulations were performed. Figure 3-3a and 3b show TICG simulations of P2VP-*b*-PS-*b*-P2VP DSA films on template patterns with different interaction chemistries (W=1.4 $L_{0,s}$, in both simulations). The template in Figure 3-3a was modeled as a two-tone pre-pattern template where the X-PS guide stripes are preferential to PS wetting uniformly across both top and sides of the guiding stripe. The strength of interaction, $\chi_s N$, was set to -0.5 ($\chi_{top} N = \chi_{side} N = -0.5$) according to a series of simulations and previous templates models.[34-35] The brush wetting was modeled to be non-preferential ($\chi_{brush} N = 0$). This simulated template leads to non-aligned assembly (Figure 3-3a). Simulating the assembly using a three-tone template, on the other hand, resulted in highly aligned assembly (Figure 3-3b), in good agreement with the experimental results (Figure 3-2c). In the three-tone pattern, the top of the X-PS was modeled to be slightly preferential to PS ($\chi_{top} N = -0.5$), while the sides of the guide stripes were modeled to be preferential for P2VP wetting

with higher strength of interaction ($\chi_{side}N$ = 1.0), creating three distinctive zones for guiding the assembly. The variation in wetting between the three zones of the template seen here is in good agreement with recent reports on three-tone templates for PS-*b*-PMMA and other BCPs.[30, 36]

The quantification of the BCP-template interactions enabled us to examine this interface in the DSA films. Templates that resulted in aligned morphology in the experimental set up (W=1.6 $L_{0,s}$, 1.4 $L_{0,s}$, 0.8 $L_{0,s}$, and 0.7 $L_{0,s}$, Figure 3-2b, 2c, 2e, and 2f, respectively) were modeled using TICG simulations (Figure 3-3c-3f). The good agreement between the molecular simulations and the tomographic results corroborates the three-tone model and highlights the role of the template's chemistry and topography in creating a side-wall driven (or assisted) directed assembly. In addition, the simulations shed light on the origin of curvature in $P2VP_S$ in the assemblies with W=0.8 $L_{0,s}$ and W=0.7 $L_{0,s}$ (Figure 3-3e and 3f, respectively). The favorable interaction of the X-PS side walls with the P2VP domains leads to assembly where the P2VP follow the geometry of the X-PS guide stripe side walls, which results in curved lamellae near the interface with the guide stripe. Indeed, the simulations show that the P2VP curvature decreases with decreasing guide stripe width, in good agreement with the tomographic results (Figure 3-2e and 2f).

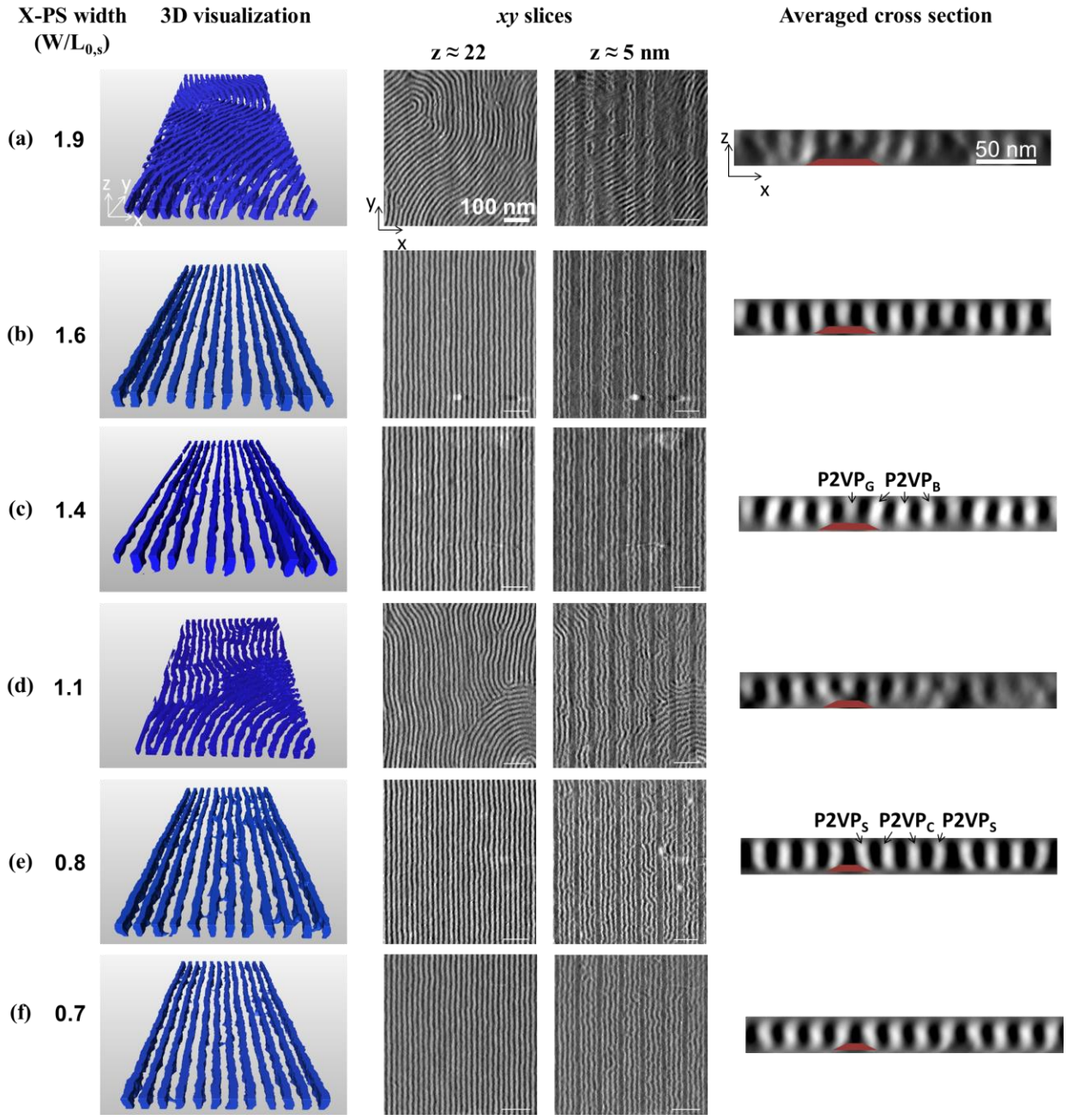

Figure 3-2. STEM tomography data of P2VP-*b*-PS-*b*-P2VP DSA film on pre-pattern templates with varying X-PS guide stripes width. High magnification visualization of the reconstructed volume (left column), 0.48 nm thick, parallel to the substrate (*xy*), slices of the reconstructed volume taken close to the top of the film (z ≈ 22 nm, central column on the left), and close to the bottom of the film (z ≈ 5 nm, central column on the right), and averaged cross sections of the reconstructed volume (right column). P2VP domains in the 3D reconstructed volume visualization are colored in blue while PS domains are transparent. One X-PS guide stripe is illustrated in each cross section to highlight the location of the pre-pattern template.

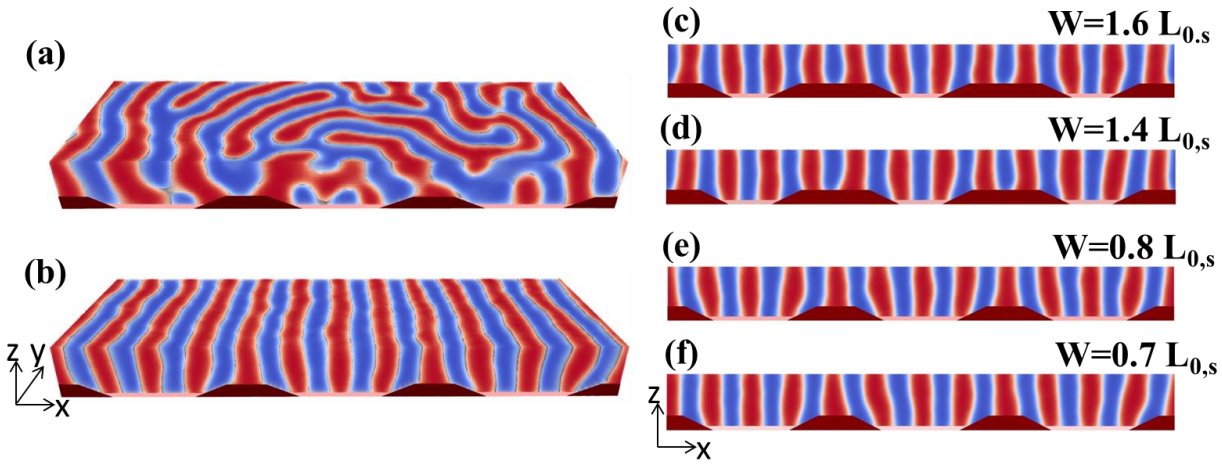

Figure 3-3. TICG simulations of P2VP-*b*-PS-*b*-P2VP DSA films. (a,b) DSA films on templates with W=1.4 $L_{0,s}$ with different interaction geometry: (a) the pre-pattern template has two-tone interaction with the BCP ($\Lambda_{top}N=\Lambda_{side}N=-1.0$; $\Lambda_{brush}N=0$), and (b) the pre-pattern template has three-tone interaction with the BCP ($\Lambda_{top}N=-0.5$; $\Lambda_{side}N=1.0$; $\Lambda_{brush}N=0$). (c-f) TICG simulations of P2VP-*b*-PS-*b*-P2VP DSA films on pre-pattern templates with three-tone interaction geometry with varying X-PS guide stripes width. Blue domains correspond to P2VP domains, red domains correspond to PS domains, while the white domains correspond to PS-P2VP interface.

3.2.3 Fluctuations and interfacial width

To fully explore a DSA system, it is necessary to probe both the through-film structure *and* the positional fluctuations in shape, size and placement of the structures with respect to the underlying template. The local interface between two domains in a BCP system is a diffuse interface with a finite interfacial width, Δ, over which the composition normal to the plane of the interface changes from A to B, and is well-modeled by a hyperbolic tangent function.[37-38] The position of the interface also fluctuates; in the melt, the positional fluctuations relate to thermal fluctuations that produce random shifts in the position of each point of the BCP interface over time and are commonly described using a capillary wave model.[38-39] After quenching into the glassy regime, positional fluctuations are locked into the surface that describes the interface between the blocks. These positional fluctuations contribute to the roughness of DSA patterns.[14]

Quantitative analysis of the STEM tomography data allowed us to specify the positional fluctuation of the PS/P2VP interface as a function of depth in the film and the location of the interface with respect to the features of the underlying template. To quantify the positional fluctuation of the PS/P2VP interface, the center of the PS/P2VP interface was found using the canny edge detection algorithm[40] and the standard deviation, σ, of this line from a straight line along the *y* axis was calculated for each interface and in each *xy* slice of the tomographic reconstructed volume. Positional fluctuation measurements were performed in two P2VP-*b*-PS-*b*-P2VP representative films: DSA film on a templates with W=1.4 $L_{0,s}$, and DSA film on a template with W=0.8 $L_{0,s}$. It should be noted that the choice of magnification in the TEM that enables high resolution structural characterization also limits the field of view for fluctuation analysis. Nonetheless, with ~850 nm field of view in the *y* direction, and an estimated resolution of 0.5 nm, the BCP interface fluctuations could be reliably measured.

Positional fluctuation (σ) of P2VP-*b*-PS-*b*-P2VP DSA film on templates with W=1.4 $L_{0,s}$ as a function of depth are presented in Figure 3-4a. σ differed across the film's depth, with high value at the top of the film (1.4 ± 0.1 nm) and at the bottom of the film (1.5 ± 0.1 nm), and lower values at the middle of the film's thickness (1.1 ± 0.1 nm). All measurements are shown as average ± one standard deviation of the 80 PS/P2VP interface in the tomographic field of view. The change in positional fluctuations with depth can be visually seen in the *xy* slices in Movie 2. $\sigma_{template}$, measured before photoresist removal using SEM imaging, was 1.1 ± 0.1 nm, and while these fluctuations have an effect on the BCP fluctuations,[41] they do not solely explain the high fluctuations observed at the bottom of the film.

To gain insight into the origin of the depth-dependent behavior described previously, we compared the measured σ to the theoretically predicted value of P2VP-*b*-PS-*b*-P2VP

fluctuations. The standard deviation of the interface position between polymer blocks can be predicated for a diblock system from the interface tension γ_0, the interfacial width, and the polymer periodicity L_0.[14, 37]

(1) $\sigma^2 = \langle {\delta_x}^2 \rangle = \frac{1}{2\pi\gamma_0} \ln(\frac{L_0}{\Delta})$

where $\langle {\delta_x}^2 \rangle$ is the variance of the interface position between the polymer blocks. The interfacial width can be calculated using χ, the degree of polymerization N, and the statistical segment length a_{st} [14, 37]

(2) $\Delta = 2a_{st} \frac{1}{(6\chi)^{0.5}} (1 + \frac{1.34}{(\chi N)^{\frac{1}{3}}})$

Although there has not been yet a theoretical description of the variance in interface position in triblock copolymers, theoretical calculations for diblock systems have been used for triblock copolymers by modifying the total degree of polymerization to N_{eff}, where $N_{eff} = N/2$.[42-43] The interface tension in equation (1) is calculated according to mean-field theory using the following equation (γ_0 is expressed in kT units):

(3) $\gamma_0 = \frac{a_{st}\chi^{0.5}}{\upsilon 6^{0.5}}$

where υ is the monomer volume.

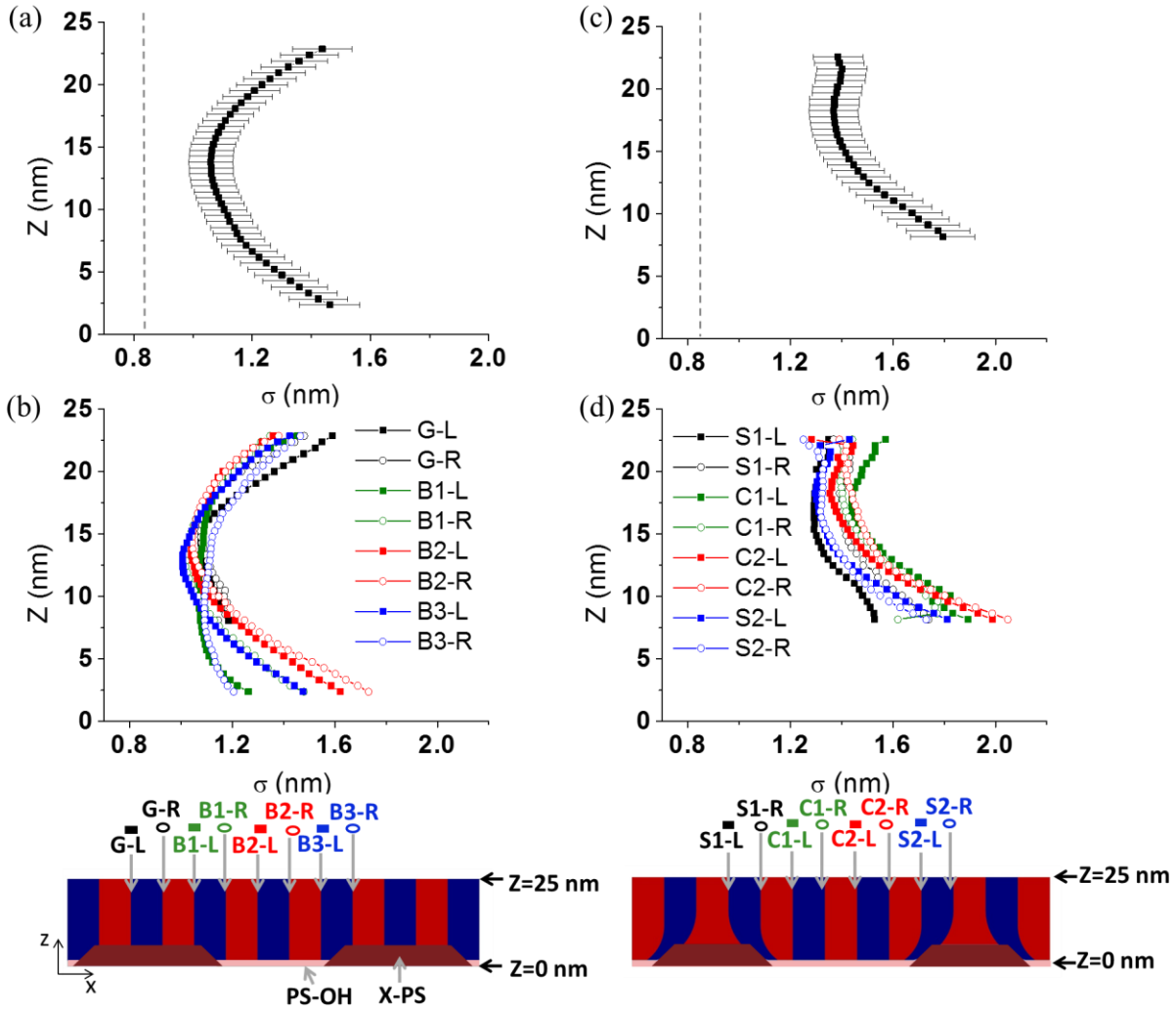

Figure 3-4. Positional fluctuation of the PS/P2VP interface as a function of depth in P2VP-*b*-PS-*b*-P2VP DSA film on templates with W=1.4 $L_{0,s}$ (a,b), and W=0.8 $L_{0,s}$ (c,d). (a,c) Average σ of all the interfaces measured in the tomographic reconstructed volume as a function of depth. The grey dashed line shows the theoretically predicted value of σ for P2VP-*b*-PS-*b*-P2VP (0.82 nm). (b,d) The fluctuations shown in (a) and (c) plotted per edge in the 4x density multiplication repeating unit, respectively. For each P2VP lamellae, the left edge is marked with solid squares, and the right edge is marked with open circles. Colors correspond to the lamellae location as depicted in the schematic illustrations at the bottom of the figure.

In order to calculate the theoretical σ of PS/P2VP interface positional fluctuations, one must consider the effective χ of this system under SVA conditions. χ_{eff}, was calculated using equation 4:[26, 44]

(4) $\chi_{\text{eff}}=\phi_p^{\alpha}(\frac{63}{T}-0.033)$

where ϕ_p is the polymer volume fraction in the solvated state, α is the power factor, and T is the annealing temperature in K. For the conditions used in this research, the polymer volume fraction in the solvated state (extracted from swelling ratio measurements) was 0.7, α was 1.6, and T was 298 K, resulting in χ_{eff}, of 0.101.

Using the values specified in Table 3-1, the theoretical σ of P2VP-*b*-PS-*b*-P2VP was calculated to be 0.83 nm. To compare this value to the measured σ as a function of depth in the DSA film, the theoretical value was plotted as a dashed grey line in Figure 3-4a. The comparison shows that in the middle of the film (10 nm < *z* < 15 nm), the positional fluctuations are closer to the theoretically predicted value than at the top and bottom of the film, suggesting that high fluctuations are suppressed by the neighboring polymer molecules. On the other hand, as P2VP-*b*-PS-*b*-P2VP gets closer to the interfaces it deviates from the predicted value and higher fluctuations are observed. We hypothesized that at the top and the bottom interfaces, the polymer molecules are more mobile and less constrained by the neighboring polymer molecules, resulting in higher fluctuations at the interfaces. Interfacial energy of the BCP- template can also play a role; at the BCP-template interface it is difficult to optimize the interfacial energy of the two blocks with the various regions of the template, leading to higher fluctuations at that interface.

Table 3-1. Characteristics of solvent annealed P2VP-b-PS-b-P2VP

Parameter	N	N_{eff}	χ_{eff}	$L_{0,s}$ (nm)[a]	a_{st} (nm)[45]	υ (nm^3)[28]
P2VP-*b*-PS-*b*-P2VP	450	225	0.101	21.0	0.67	0.18

a- Since the film was assembled on 84 nm pitch template with 4x density multiplication, $L_{0,s}$ of the DSA calculation was 21.0 nm

In order to understand the contribution of the various lamellae to the averaged σ in each *xy* slice, the PS/P2VP interface positional fluctuations were analyzed with respect to the position of the underlying template. The positional fluctuations of each of the eight interfaces present in the 4x density multiplication DSA film with W=1.4 $L_{0,s}$ are plotted as function of depth in Figure 3-4b. To ease the interpretation of the plot, errors bars were not included in this plot; we estimated the error as ± 0.1 nm. This individual interface investigation revealed an interesting phenomenon: while at the top two thirds of the film only minor differences are seen between the various interfaces, at the bottom third of the film, and in particular in *z* heights lower than the X-PS guiding stripe, there is a strong correlation between σ and the location of the interface, with symmetric behavior around the central $P2VP_B$ lamella (B2). The two PS/P2VP interfaces of the central $P2VP_B$ lamella (B2-L and B2-R, solid red squares and open red circles, respectively) have the highest standard deviation, reaching values of 1.6-1.7 nm close to the BCP-template interface. The two PS/P2VP interfaces adjacent to the central $P2VP_B$ lamella, B1-R and B3-L (open green circles and solid blue squares, respectively), show almost identical positional fluctuations with intermediate σ value of 1.5 nm close to the BCP-template interface, while the two PS/P2VP interfaces that are the furthest away from the central $P2VP_B$ lamella (or closest to the guiding stripe), B1-L and B3-R (solid green squares and open blue circles, respectively), have the lowest σ values close to the BCP-template interface (1.2-1.3 nm). We interpret this behavior as related to the energy cost of positional fluctuations for the various interfaces. B1 and B3 (the left and right interfaces of $P2VP_B$) assemble on regions in the template which are preferential to one domain, in this case, the P2VP preferential guiding stripes sidewalls. High fluctuations of those interfaces will lead to frequent presence of P2VP or the neighboring PS on template sections that have different preference, which is unfavorable energetically. Thus, high

positional fluctuations are suppressed in PS/P2VP adjunct to the guide stripes. B2, on the other hand, assembles solely on the brush in the template, which is considered non-preferential; thus, even when the B2 PS/P2VP interfaces wiggle, P2VP stays on the same brush region and higher fluctuations can be tolerated. The difference in positional fluctuation levels between the various P2VP lamellae can be seen directly in the *xy* slice at $z \approx 5$ nm (Figure 3-2c, central column).

When P2VP-*b*-PS-*b*-P2VP was assembled on templates with W = 0.8 $L_{0,s}$, higher σ values were measured (1.4–1.8 nm, Figure 3-4c) compared to the assembly on W=1.4 $L_{0,s}$ (Figure 3-4a). The σ values were almost constant at the top 10 nm of the film, and then rapidly increased with depth to a maximum of 1.8 ± 0.1 nm at z = 8 nm. Positional fluctuations were not measured at smaller z due to the abundance of defects at the bottom of the film. The PS/P2VP interface positional fluctuations at the top of the film (1.4 ± 0.1 nm, Figure 3-4c) are very close to the values measured at the top of the film assembled on W=1.4 $L_{0,s}$ (1.4 ± 0.1, Figure 3-4a), suggesting a uniform behavior of assembly at the free surface. The high positional fluctuations observed z< 15 nm were attributed to the curvature in $P2VP_s$, and the abundance of defects formed at the bottom of this film.

In General, all the individual PS/P2VP interfaces showed similar trend with depth (Figure 3-4c). While the differences between the different PS/P2VP interfaces were small, the interfaces adjacent to the guide stripes (S1-L and S2-R; solid black squares and open blue circles, respectively) had consistently lower standard deviation values than the interfaces of the central lamellae (C1-L, C1-R, C2-L, and C2-R; solid green squares, open green circles, solid red squares, and open red circles, respectively). It should be noted that measurements in *xy* slices can overestimate the fluctuation in curved lamellae since the positional fluctuations are normal to the

interface surface while the measurements are done in slices parallel to the substrate. Thus, close to the guide stripes, $P2VP_S$ fluctuations have probably smaller values.

Current routine measurements of BCP DSA positional fluctuations (or line edge roughness) are preformed using top-down SEM images of the film, usually after etching one of the BCP domains to obtain high contrast imaging.[15-16, 41] The tomographic characterization, on the other hand, enabled us to probe the interface between the polymer blocks and through the depth of the film. The change in σ with depth and with relative position to the underlying template can have implications on understanding and designing BCP processes. First, the increase in fluctuations with distance from the guiding stripes at aligned DSA films (Figure 3-4b) suggest that while it is desirable to fabricate templates with large density multiplication factors, it might result in high positional fluctuations of lamellae that are far from the guiding stripes. Second, since minimal fluctuations were measured at the middle of the film thickness, we anticipate that in thicker DSA films, substantial part of the film thickness will have low fluctuations, which can still result to high fidelity structures after pattern transfer. Therefore, high aspect ratio DSA patterns might be preferable for obtaining low roughness. Third, techniques that probe structures in reciprocal space, such as X-ray scattering, often rely on models which describe the system as a single unit cell from one guiding stripe to another, exhibiting Gaussian fluctuations around the center of mass.[46] The fluctuations depth profile presented in this work implies that these models can be improved if the changes in positional fluctuations as a function of depth are accounted for.

The interfacial width of a BCP system plays an important role in the ability to transfer the BCP pattern to an underlying layer.[13] Measurements of the interface that probe the averaged structure, such as X-ray probes and neutron reflectivity, measure an "apparent" width Δ_a, which

combines both the interfacial width and the positional fluctuations of this interface.[14, 16, 38] When the positional fluctuations follow a normal distribution, the relationship between Δ_a, Δ, and $\langle \delta_x{}^2 \rangle$ can be described using equation 5:[14, 37]

(5) $\Delta^2 = \Delta_a^2 - 2\pi\langle \delta_x{}^2 \rangle$

Tomographic characterization of DSA films provides a rare opportunity to extract the interfacial width from real space data since it enables examination of both the averaged structure and the positional fluctuation. Δ_a was measured from the averaged through-film structure while the fluctuations were measured in the *xy* slices. Since σ varied with depth and location, we focused our measurement and discussion on the middle of the film (z = 13.3 nm) of the best assembled sample (P2VP-*b*-PS-*b*-P2VP film on template with W = 1.4 $L_{0,s}$). At this z, the change in fluctuations with z was minimal and no distinctive difference between the various lamellae was found. Figure 3-5 shows the intensity profile (red circles) of the averaged cross section of P2VP-*b*-PS-*b*-P2VP DSA film on templates with W = 1.4 $L_{0,s}$ at z = 13.3 nm. Independent fitting of each lamella with a hyperbolic tangent function at both interfaces (blue line) resulted in an apparent width of Δ_a = 5.0 ± 0.4 nm. The fluctuations measured at that depth ($\sigma_{z=13.3nm}$ = 1.1 ± 0.1 nm; $\langle \delta_x{}^2 \rangle_{z=13.3nm}$ = 1.1 ± 0.1 nm^2) had a normal distribution and therefore can be used in equation (5), resulting in an interfacial width of Δ = 4.2 ± 0.4 nm. To compare the measured values with the predicted values of P2VP-*b*-PS-*b*-P2VP fluctuations, we turn back to equations (1) - (5). The predicted Δ and Δ_a, calculated from these equations and the parameters in Table 3-1, are 2.5 nm and 3.3 nm, respectively. The values determined from the TEM analysis are therefore significantly larger than the predicted values. TICG simulations predict an intermediate Δ_a value of 3.7 nm. The high apparent and interfacial width, measured from the tomographic data, hints that assembly in the solvated state and trapping that state during rapid drying in thin

films leads to a PS/P2VP interfacial width understandably much broader than assembly without boundary conditions (thick film or bulk configuration). In previous studies on thermally annealed PS-PVP BCPs, interfacial widths of 2.8 nm to 3.3 nm were measured.[42, 47] Further study is needed to determine the relative contributions from SVA and other aspects of the DSA process to the apparent interfacial width. It should also be noted, that since the measurement was conducted on a stained film, there could be also an influence of the staining profile; while the iodine interacts with the pyridine group in the P2VP domain[32], small interaction with the PS domain could result in a wider measured apparent width. The contribution of various staining agents such as iodine and selective Al_2O_3 growth[19] to the interfacial profile measurements has not been quantified in past studies and is the subject of ongoing research.

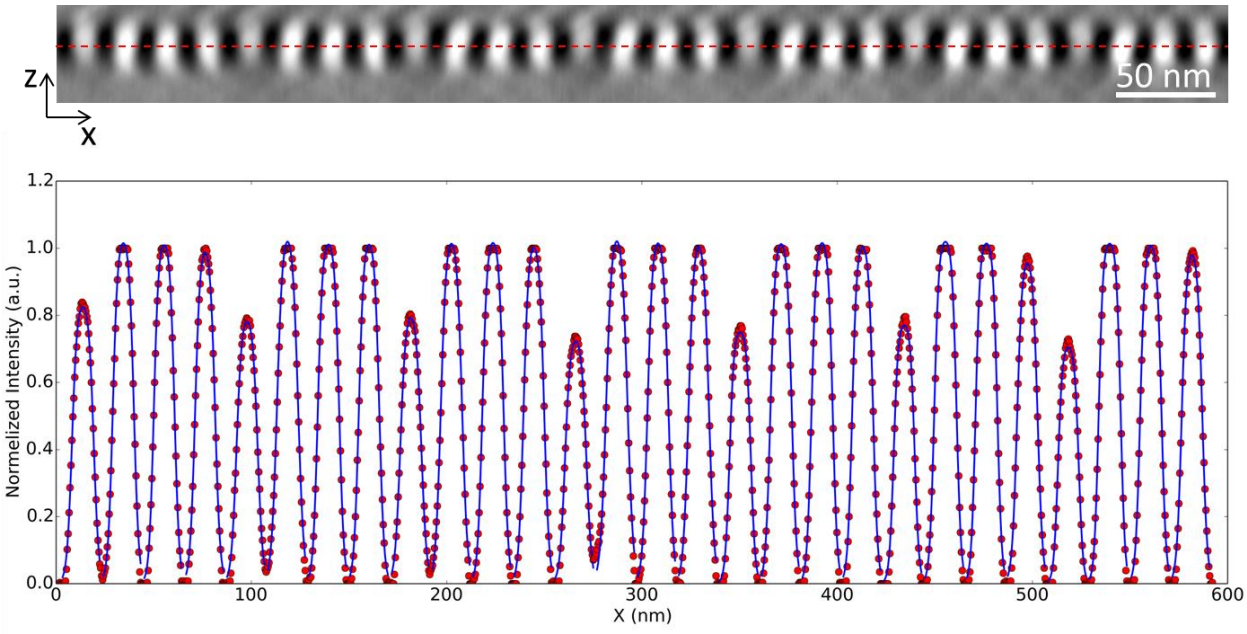

Figure 3-5. The apparent width of P2VP-*b*-PS-*b*-P2VP DSA film on template with W=1.4 $L_{0,s}$. The intensity profile (red circles) of the averaged cross section at *z* = 13.3 nm (marked at the top with a dashed red line) was fitted with hyperbolic tangent function (blue line).

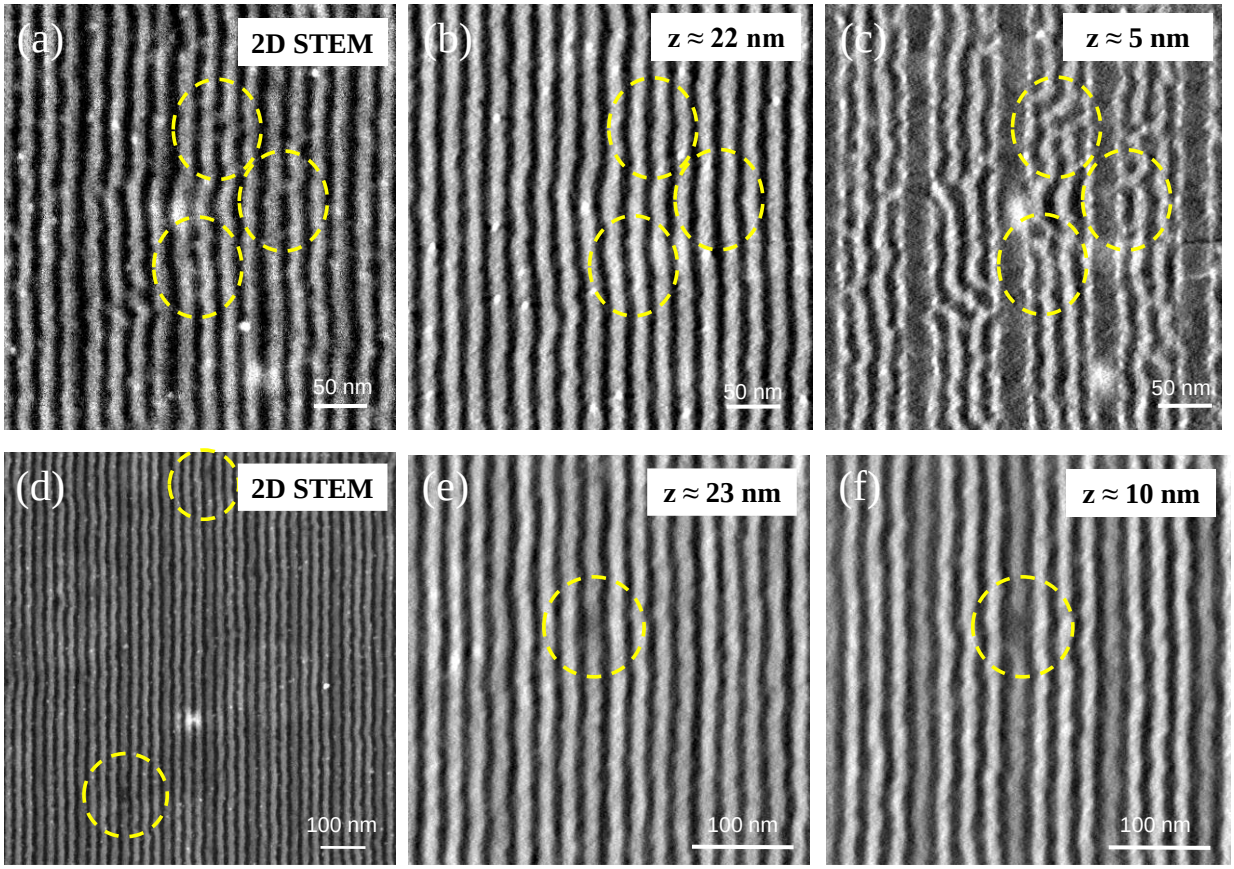

Figure 3-6. The three dimensional structure of DSA micro-bridge and line breakage defects. P2VP-*b*-PS-*b*-P2VP films were assembled on templates with (a-c) W = 0.8 $L_{0,s}$, or (d-f) W = 1.4 $L_{0,s0}$. (a) STEM image with few examples of defects that are classified as micro-bridge defects (marked with a dashed yellow circle). (b,c) *xy* slices from STEM tomography reconstruction volume of the same are shown in (a) at *z* heights 22 nm and 5 nm, respectively. (d) STEM image with two line breakage defects marked with dashed yellow circles. (e,f) *xy* slices from STEM tomography reconstruction volume of line breakage defect at *z* heights 23 nm and 10 nm, respectively.

3.2.4 Understanding DSA defects

Understanding the origin of defects in BCP DSA films and the defects' morphology in the film is essential for developing processes with low defect density. The most common BCP-related defects in chemo-epitaxy DSA are: dislocations, residues with topography, micro-bridges, and line breakage.[12, 48] Recent investigations on the formation and kinetics of dislocations in DSA films have led to better understanding of their origin and 3D morphology.[9-

[10, 49] On micro-bridges and line breakage defects, on the other hand, little is known. In particular, there is scarce information on the formation of these defects in DSA films with density multiplication. Gronheid *et al.*[12] and Pathangi *et al.*[11] reported that micro-bridges (also called "flat bridges") are created in the BCP layer but are very difficult to detect after assembly and are usually identified only after the pattern transfer process.

In transmission microscopy, the 2D image is a projection of the 3D volume, similar to the effect of pattern transfer. By exploiting the abundance of defects in DSA film on templates with W=0.8 $L_{0,s}$, micro-bridges were explored. A 2D STEM image of P2VP-*b*-PS-*b*-P2VP DSA film on templates with W=0.8 $L_{0,s}$ (Figure 3-6a) shows several structures (marked with dashed yellow circles) that are reminiscent of the micro-bridges after pattern transfer. The *xy* slices obtained from STEM tomography reconstructed volume of the same area of Figure 3-6a reveal that one source for micro-bridges are defects that were formed at the bottom of the film (Figure 3-6c). These defects are not present at the top of the film (Figure 3-6b), and therefore cannot be identified using SEM characterization. The defects persist through ~ 5 nm of the film thickness at the bottom of the film, and therefore can affect the quality of pattern transfer from this BCP film. While micro-bridge formations in the assembly investigated here is related to the non-optimal geometry of the template, it is reasonable to assume that other types of mismatch between the templates and the BCP will also lead to formation of micro-bridges defects. Indeed, Williamson *et al.* observed an increased formation of micro-bridges defects with an increased mismatch between the chemical composition of the BCP and the pre-pattern template (through BCP formulation).[30]

Line breakage defects were also observed in P2VP-*b*-PS-*b*-P2VP DSA (Figure 3-6d). These defects, found in P2VP-*b*-PS-*b*-P2VP DSA film on templates with W=1.4 $L_{0,s}$, are

disconnected P2VP domains. Interestingly, they were found almost entirely in $P2VP_G$, *i.e.* on top of the X-PS guide stripe. STEM tomography of the defect reveals that the line breakage appears at the entire $P2VP_G$ thickness, with small disconnection at the top of the film (Figure 3-6e), and larger disconnection at the bottom of $P2VP_G$ (Figure 3-6f), close to the interface with the X-PS. We hypothesize that the line breakage defects are the result of defects in the X-PS guiding stripes (pinholes or local excess of X-PS), although accurate comparison between the templates and the BCP layer is needed in order to corroborate that.

3.3 Conclusion

Detailed investigation of the through-film structures, fluctuations, and defects in solvent annealed P2VP-*b*-PS-*b*-P2VP DSA films was conducted through STEM tomography three-dimensional characterization. The tomographic characterization together with molecular simulations enabled us to correlate between the template chemistry, geometry, and topography and the BCP assembled structure, and revealed hidden defects and curved lamellae at DSA films that were considered aligned from top-down imaging. The topography in the template together with preferential wetting of the X-PS side walls by the P2VP resulted in a side-wall driven directed assembly. Measurements of the positional fluctuations of the BCP domain interface, conducted through the film's depth and as function of the interface location in a density multiplication film, showed minimum fluctuations at the middle of the film thickness and an increase in fluctuations at the bottom of the film as PS/P2VP interfaces were further away from the guiding stripes. Moreover, it was demonstrated that combining positional fluctuations measurements and profile analysis of the through film averaged structure can enable interfacial width measurements and shed light on BCP interface in a DSA processes. Finally, both micro-

bridge defects and line breakage defects 3D structures were characterized, pinpointing the location of defects through the film's thickness and with regard to the pre-pattern template.

SVA and triblock DSA are examples of the growing arsenal of materials and processes that enable sub-10 nm DSA patterning;[26] this arsenal also includes top-coat DSA,[50] and high-χ, top-coat free materials.[51] While each method has specific parameters that influence the BCP assembly, in all these methods, the BCP interaction with the BCP-guiding pattern interface is crucial for successful directed assembly. Therefore, probing the BCP structure and its fluctuations at the BCP-guiding pattern interface is necessary to fully describe high χ DSA assembly, and enable better understanding of the assembly processes. Combining experimental observations of the BCP 3D structure with theoretical simulations will allow better design and implementation of BCP DSA.

3.4 References:

1. Dusa, M.; Quaedackers, J.; Larsen, O. F. A.; Meessen, J.; van der Heijden, E.; Dicker, G.; Wismans, O.; de Haas, P.; van Ingen Schenau, K.; Finders, J.; Vleeming, B.; Storms, G.; Jaenen, P.; Cheng, S.; Maenhoudt, M., Pitch Doubling Through Dual-Patterning Lithography Challenges in Integration and Litho Budgets. *Proc. SPIE* **2007**, *6520*, 65200G.

2. Xu, P.; Chen, Y.; Chen, Y.; Miao, L.; Sun, S.; Kim, S.-W.; Berger, A.; Mao, D.; Bencher, C.; Hung, R.; Ngai, C., Sidewall Spacer Quadruple Patterning for 15nm Half-Pitch. *Proc. SPIE* **2011**, *7973*, 79731Q.

3. Gregory, S. D.; He, G.; Lei, W.; Jeff, L.; Patel, K. C.; Yves-Andre, C.; Ricardo, R.; Thomas, R. A., Transfer of Self-Aligned Spacer Patterns for Single-Digit Nanofabrication. *Nanotechnology* **2015**, *26*, 085304.

4. Ouk Kim, S.; Solak, H. H.; Stoykovich, M. P.; Ferrier, N. J.; de Pablo, J. J.; Nealey, P. F., Epitaxial Self-Assembly of Block Copolymers on Lithographically Defined Nanopatterned Substrates. *Nature* **2003**, *424*, 411-414.

5. Bita, I.; Yang, J. K. W.; Jung, Y. S.; Ross, C. A.; Thomas, E. L.; Berggren, K. K., Graphoepitaxy of Self-Assembled Block Copolymers on Two-Dimensional Periodic Patterned Templates. *Science* **2008**, *321*, 939-943.

6. Ross, C. A.; Berggren, K. K.; Cheng, J. Y.; Jung, Y. S.; Chang, J.-B., Three-Dimensional Nanofabrication by Block Copolymer Self-Assembly. *Adv. Mater.* **2014**, *26*, 4386-4396.

7. Liu, C.-C.; Ramírez-Hernández, A.; Han, E.; Craig, G. S. W.; Tada, Y.; Yoshida, H.; Kang, H.; Ji, S.; Gopalan, P.; de Pablo, J. J.; Nealey, P. F., Chemical Patterns for Directed Self-Assembly of Lamellae-Forming Block Copolymers with Density Multiplication of Features. *Macromolecules* **2013**, *46*, 1415-1424.

8. Li, W.; Müller, M., Defects in the Self-Assembly of Block Copolymers and Their Relevance for Directed Self-Assembly. *Annu. Rev. Chem. Biomol. Eng.* **2015,** *6*, 187-216.

9. Hur, S.-M.; Thapar, V.; Ramírez-Hernández, A.; Khaira, G.; Segal-Peretz, T.; Rincon-Delgadillo, P. A.; Li, W.; Müller, M.; Nealey, P. F.; de Pablo, J. J., Molecular pathways for defect annihilation in directed self-assembly. *Proc. Natl. Acad. Sci.* **2015**, *112*, 14144-14149.

10. Kim, B.; Laachi, N.; Delaney, K. T.; Carilli, M.; Kramer, E. J.; Fredrickson, G. H., Thermodynamic and Kinetic Aspects of Defectivity in Directed Self-Assembly of Cylinder-Forming Diblock Copolymers in Laterally Confining Thin Channels. *J. Appl. Polym. Sci.* **2014**, *131*, 40790.

11. Pathangi, H.; Chan, B. T.; Bayana, H.; Vandenbroeck, N.; Van Den Heuvel, D.; Van Look, L.; Rincon-Delgadillo, P.; Cao, Y.; Kim, J.; Lin, G.; Parnell, D.; Nafus, K.; Harukawa, R.; Chikashi, I.; Nagaswami, V.; D'Urzo, L.; Gronheid, R.; Nealey, P., Defect Mitigation and Root Cause Studies in IMEC's 14nm Half-Pitch Chemo-Epitaxy DSA Flow. *Proc. SPIE* **2015**, *9423*, 94230M.

12. Gronheid, R.; Rincon Delgadillo, P.; Pathangi, H.; Van den Heuvel, D.; Parnell, D.; Chan, B. T.; Lee, Y.-T.; Van Look, L.; Cao, Y.; Her, Y.; Lin, G.; Harukawa, R.; Nagaswami, V.; D'Urzo, L.; Somervell, M.; Nealey, P., Defect Reduction and Defect Stability in IMEC's 14nm half-pitch Chemo-Epitaxy DSA Flow. *Proc. SPIE* **2014**, *9049*, 904905.

13. Wan, L.; Ruiz, R.; Gao, H.; Patel, K. C.; Albrecht, T. R.; Yin, J.; Kim, J.; Cao, Y.; Lin, G., The Limits of Lamellae-Forming PS-b-PMMA Block Copolymers for Lithography. *ACS Nano* **2015**, *9*, 7506-7514.

14. Stein, G. E.; Liddle, J. A.; Aquila, A. L.; Gullikson, E. M., Measuring the Structure of Epitaxially Assembled Block Copolymer Domains with Soft X-ray Diffraction. *Macromolecules* **2010**, *43*, 433-441.

15. Sunday, D. F.; Ashley, E.; Wan, L.; Patel, K. C.; Ruiz, R.; Kline, R. J., Template–Polymer Commensurability and Directed Self-Assembly Block Copolymer Lithography. *J. Polym. Sci., Part B: Polym. Phys.* **2015**, *53*, 595-603.

16. Sunday, D. F.; Hammond, M. R.; Wang, C.; Wu, W.-l.; Delongchamp, D. M.; Tjio, M.; Cheng, J. Y.; Pitera, J. W.; Kline, R. J., Determination of the Internal Morphology of Nanostructures Patterned by Directed Self Assembly. *ACS Nano* **2014**, *8*, 8426–8437.

17. Segal-Peretz, T.; Winterstein, J.; Ren, J.; Biswas, M.; Liddle, J. A.; Elam, J. W.; Ocola, L. E.; Divan, R. N. S.; Zaluzec, N.; Nealey, P. F., Metrology of DSA process using TEM tomography. *Proc. SPIE* **2015**, 9424, 94240U.

18. Gotrik, K. W.; Lam, T.; Hannon, A. F.; Bai, W.; Ding, Y.; Winterstein, J.; Alexander-Katz, A.; Liddle, J. A.; Ross, C. A., 3D TEM Tomography of Templated Bilayer Films of Block Copolymers. *Adv. Funct. Mater.* **2014**, *24*, 7689-7697.

19. Segal-Peretz, T.; Winterstein, J.; Doxastakis, M.; Ramírez-Hernández, A.; Biswas, M.; Ren, J.; Suh, H. S.; Darling, S. B.; Liddle, J. A.; Elam, J. W.; de Pablo, J. J.; Zaluzec, N. J.; Nealey, P. F., Characterizing the Three-Dimensional Structure of Block Copolymers *via* Sequential Infiltration Synthesis and Scanning Transmission Electron Tomography. *ACS Nano* **2015**, *9*, 5333-5347.

20. Hur, S.-M.; Khaira, G. S.; Ramírez-Hernández, A.; Müller, M.; Nealey, P. F.; de Pablo, J. J., Simulation of Defect Reduction in Block Copolymer Thin Films by Solvent Annealing. *ACS Macro Lett.* **2015**, *4*, 11-15.

21. Sun, Z.; Chen, Z.; Zhang, W.; Choi, J.; Huang, C.; Jeong, G.; Coughlin, E. B.; Hsu, Y.; Yang, X.; Lee, K. Y.; Kuo, D. S.; Xiao, S.; Russell, T. P., Directed Self-Assembly of Poly(2-vinylpyridine)-*b*-polystyrene-*b*-poly(2-vinylpyridine) Triblock Copolymer with Sub-15 nm Spacing Line Patterns Using a Nanoimprinted Photoresist Template. *Adv. Mater.* **2015**, *27*, 4364-4370.

22. Chaudhari, A.; Ghoshal, T.; Shaw, M. T.; Cummins, C.; Borah, D.; Holmes, J. D.; Morris, M. A., Formation of Sub-7 nm Feature Size PS-*b*-P4VP Block Copolymer Structures by Solvent Vapour Process. *Proc. SPIE* **2014**, *9051*, 905110.

23. Kim, J. M.; Kim, Y.; Park, W. I.; Hur, Y. H.; Jeong, J. W.; Sim, D. M.; Baek, K. M.; Lee, J. H.; Kim, M.-J.; Jung, Y. S., Eliminating the Trade-Off between the Throughput and Pattern Quality of Sub-15 nm Directed Self-Assembly *via* Warm Solvent Annealing. *Adv. Funct. Mater.* **2015**, *25*, 306-315.

24. Nealey, P. F.; Wan, L. Solvent Annealing Block Copolymers on Patterned Substrates. US20120202017 A1, Aug. 9, **2012**.

25. Wan, L.; Ji, S.; Liu, C.-C.; Craig, G. S. W.; Nealey, P. F., Directed Self-Assembly of Solvent-Vapor-Induced Non-Bulk Block Copolymer Morphologies on Nanopatterned Substrates. *Soft Matter* **2016**, *12*, 2914-2922.

26. Xiong, S.; Wan, L.; Ishida, Y.; Chapuis, Y.-A.; Craig, G. S. W.; Ruiz, R.; Nealey, P. F., Directed Self-Assembly of Triblock Copolymer on Chemical Patterns for Sub-10-nm Nanofabrication *via* Solvent Annealing. *ACS Nano* **2016**, 10, 7855–7865

27. Dai, K. H.; Kramer, E. J., Determining the Temperature-Dependent Flory Interaction Parameter for Strongly Immiscible Polymers From Block Copolymer Segregation Measurements. *Polymer* **1994**, *35*, 157-161.

28. Eitouni, H.; Balsara, N., Thermodynamics of Polymer Blends. In *Physical Properties of Polymers Handbook*, Mark, J., Ed. Springer New York: **2007**; pp 339-356.

29. Yoshida, H.; Suh, H. S.; Ramirez-Herunandez, A.; Lee, J. I.; Aida, K.; Wan, L.; Ishida, Y.; Tada, Y.; Ruiz, R.; de Pablo, J.; Nealey, P. F., Topcoat Approaches for Directed Self-Assembly of Strongly Segregating Block Copolymer Thin Films. *J. Photopolym. Sci. Technol.* **2013**, *26*, 55-58.

30. Williamson, L. D.; Seidel, R. N.; Chen, X.; Suh, H. S.; Rincon Delgadillo, P.; Gronheid, R.; Nealey, P. F., Three-Tone Chemical Patterns for Block Copolymer Directed Self-Assembly. *ACS Appl. Mater. Interfaces* **2016**, *8*, 2704-2712.

31. Paik, M. Y.; Bosworth, J. K.; Smilges, D.-M.; Schwartz, E. L.; Andre, X.; Ober, C. K., Reversible Morphology Control in Block Copolymer Films *via* Solvent Vapor Processing: An *in Situ* GISAXS Study. *Macromolecules* **2010**, *43*, 4253-4260.

32. Sawyer, L. C. G., David T. , *Polymer Microscopy*. Springer Science: **1996**.

33. Delgadillo, P. A. R. Origin of defects in directed self-assembly of diblock copolymers using feature multiplications. Ph.D. Dissertation, Univeristy of Chicago, Chicago, IL, and KU Leuven, Belgium, **2014**.

34. Detcheverry, F. A.; Kang, H.; Daoulas, K. C.; Müller, M.; Nealey, P. F.; de Pablo, J. J., Monte Carlo Simulations of a Coarse Grain Model for Block Copolymers and Nanocomposites. *Macromolecules* **2008**, *41*, 4989-5001.

35. Liu, C.-C.; Han, E.; Onses, M. S.; Thode, C. J.; Ji, S.; Gopalan, P.; Nealey, P. F., Fabrication of Lithographically Defined Chemically Patterned Polymer Brushes and Mats. *Macromolecules* **2011**, *44*, 1876-1885.

36. Cushen, J. D.; Wan, L.; Blachut, G.; Maher, M. J.; Albrecht, T. R.; Ellison, C. J.; Willson, C. G.; Ruiz, R., Double-Patterned Sidewall Directed Self-Assembly and Pattern Transfer of Sub-10 nm PTMSS-*b*-PMOST. *ACS Appl. Mater. Interfaces* **2015**, *7*, 13476–13483.

37. Semenov, A. N., Theory of Block Copolymer Interfaces in the Strong Segregation Limit. *Macromolecules* **1993**, *26*, 6617-6621.

38. Shull, K. R.; Mayes, A. M.; Russell, T. P., Segment Distributions in Lamellar Diblock Copolymers. *Macromolecules* **1993**, *26*, 3929-3936.

39. Matsen, M. W., The Standard Gaussian Model for Block Copolymer Melts. *Journal of Physics: Condensed Matter* **2002**, *14*, R21.

40. Canny, J., A Computational Approach to Edge Detection. *Pattern Analysis and Machine Intelligence, IEEE Transactions* **1986**, *PAMI-8*, 679-698.

41. Stoykovich, M. P.; Daoulas, K. C.; Müller, M.; Kang, H.; de Pablo, J. J.; Nealey, P. F., Remediation of Line Edge Roughness in Chemical Nanopatterns by the Directed Assembly of Overlying Block Copolymer Films. *Macromolecules* **2010**, *43*, 2334-2342.

42. Anastasiadis, S. H.; Retsos, H.; Toprakcioglu, C.; Menelle, A.; Hadziioannou, G., On the Interfacial Width in Triblock *versus* Diblock Copolymers: A Neutron Reflectivity Investigation. *Macromolecules* **1998**, *31*, 6600-6604.

43. Matsen, M. W.; Thompson, R. B., Equilibrium Behavior of Symmetric ABA Triblock Copolymer Melts. *J. Chem. Phys.* **1999**, *111*, 7139-7146.

44. Lodge, T. P.; Hanley, K. J.; Pudil, B.; Alahapperuma, V., Phase Behavior of Block Copolymers in a Neutral Solvent. *Macromolecules* **2003**, *36*, 816-822.

45. Hiemenz, P. C.; Lodge, T., *Polymer chemistry*. 2nd ed.; CRC Press: Boca Raton, **2007**; pp 587.

46. Guinier, A., *X-ray Diffraction in Crystals, Imperfect Crystals, and Amorphous Bodies*. Dover: **1994**.

47. Koneripalli, N.; Levicky, R.; Bates, F. S.; Matsen, M. W.; Satija, S. K.; Ankner, J.; Kaiser, H., Ordering in Blends of Diblock Copolymers. *Macromolecules* **1998**, *31*, 3498-3508.

48. Bencher, C.; Smith, J.; Miao, L.; Cai, C.; Chen, Y.; Cheng, J. Y.; Sanders, D. P.; Tjio, M.; Truong, H. D.; Holmes, S.; Hinsberg, W. D., Self-Assembly Patterning for Sub-15 nm Half-Pitch: a Transition From Lab to Fab. *Proc. SPIE* **2011**, *7970*, 79700F.

49. Nagpal, U.; Müller, M.; Nealey, P. F.; de Pablo, J. J., Free Energy of Defects in Ordered Assemblies of Block Copolymer Domains. *ACS Macro Lett.* **2012**, *1*, 418-422.

50. Bates, C. M.; Seshimo, T.; Maher, M. J.; Durand, W. J.; Cushen, J. D.; Dean, L. M.; Blachut, G.; Ellison, C. J.; Willson, C. G., Polarity-Switching Top Coats Enable Orientation of Sub–10-nm Block Copolymer Domains. *Science* **2012**, *338*, 775-779.

51. Hirahara, E.; Paunescu, M.; Polishchuk, O.; Jeong, E.; Ng, E.; Shan, J.; Kim, J.; Hong, S.; Baskaran, D.; Lin, G.; Vora, A.; Tjio, M.; Arellano, N.; Rettner, C. T.; Lofano, E.; Liu, C.-C.; Tsai, H.; Chunder, A.; Nguyen, K.; Friz, A. M.; Bowers, A. N.; Balakrishnan, S.; Cheng, J. Y.; Sanders, D. P. Directed Self-Assembly of Topcoat-Free, Integration-Friendly High-X Block Copolymers, *Proc. SPIE* **2015,** 9425, 94250P.

CHAPTER 4: ENGINEERING THE KINETICS OF DIRECTED SELF-ASSEMBLY OF BLOCK COPOLYMERS TOWARD FAST ASSEMBLY AND LOW DEFECTIVITY

4.1 Introduction

Directed self-assembly (DSA) of block copolymers (BCP) has received considerable attention in recent years from both academia and industry for applications in advanced lithography and semiconductor patterning.[1–3] DSA harnesses lithographically defined templates with chemical contrast and/or topography to precisely control the placement of self-assembled BCP nanostructures.[4,5] In turn, the BCP can spontaneously interpolate between the lithographic features, multiplying the feature density and patterning resolution.[6,7] High levels of perfection and pattern complexity have been achieved and DSA-based device and integration have been demonstrated.[8–10] For DSA to be applicable in high volume semiconductor manufacturing, challenges remain in defect reduction to reach the industrial target of less than 1 defect per 100 cm^2 area, or less than one per trillions of structures. To achieve such extremely low levels of defect density, it is imperative to fully understand the mechanisms of structure formation and carefully consider the processing parameters.

The evaluation and optimization of DSA have been mainly based on the structures at thermal equilibrium but the kinetics of structure formation are equally important. Recent theoretical investigations have shown that the free energy of defects is much higher than that of the aligned state.[11,12] Thus the defects cannot be equilibrium structures but rather local, metastable deviations that are kinetically trapped. Hur *et al.* and Li *et al.* studied the molecular pathways for the annihilation of dislocation defects using the string method.[13,14] They found that even for a single dislocation pair separated by one domain, one of the simplest defects, there are

multiple free energy barriers along the annihilation pathway that can cause the morphology to become trapped in a defective state. Larger and more complex defects have much higher barriers and are increasingly difficult to annihilate.

The simulation results suggest that there exist a complex thermodynamic landscape that determines the kinetics and defectivity of DSA. To enhance DSA kinetics and eliminate defects, it is necessary to design a thermodynamic landscape with both minimum barriers and a large energy penalty between disordered and aligned states. The thermodynamic landscape is determined by the free energy of transient 3D structures along the kinetic evolution. To engineer the thermodynamic landscape, we need to characterize the evolution of 3D structures and understand the materials and process parameters that dictate the stabilities of the 3D structures. Recently, electron tomography has been proven to be a powerful tool in investigating the 3D structures in BCP thin films, especially complex and non-uniform 3D morphologies that are hard to visualize using cross-sectional methods or X-ray scattering.[15–17]

Here we investigated the kinetic process of DSA using arrested annealing and TEM tomography. We seek to capture the evolution of 3D structures and decipher the mechanism behind structural formation. In addition, we systematically studied the influences of various DSA processing conditions on the kinetic evolution and strived to identify the key parameters that determines the thermodynamic landscape.

4.2 Experimental section

4.2.1 Materials

Cross-linkable polystyrene (X-PS) (AZEMBLY NLD-128), P(S-*r*-MMA) brush (AZEMBLY NLD-127, 51% PS), P(S-*b*-MMA) BCP $L_0 = 28\ nm$ (AZEMBLY PME-312) were

provided by EMD Performance Materials and used as received. Silicon wafers coated with 30 nm silicon nitride on both sides were purchased from WRS Materials.

4.2.2 Chemical pattern fabrication and BCP assembly

Chemical patterns were prepared on a 300 mm wafer process line IMEC in Leuven, Belgium, following previously reported methods.[18] Briefly, 8 nm thick X-PS was spin-coated onto the substrate and thermally crosslinked at 315℃ for 5 min under nitrogen environment. The wafers were then coated with resist and patterned with immersion lithography or e-beam lithography into line and space patterns. The resist line pattern was etched into the X-PS layer using oxygen-containing plasma. The etched resist lines have a pitch of $L_s = 84\ nm$ and the line width was $W = 21\ nm$. After resist removal, a 50 nm layer of NLD-127 was coated onto the patterned substrate and annealed at 250℃ for 5 min to graft onto the exposed substrate between X-PS guiding stripes. The excess brush was rinsed with propylene glycol methyl ether acetate (PGMEA), leaving a 5.5 nm thick brush layer between the guiding stripes. A 35 nm thick layer of PME-312 BCP was spin-coated onto the chemical pattern. The samples were then annealed on a hotplate under nitrogen environment at 190℃ or 250℃ for various times and quenched to room temperature on an aluminum block.

4.2.3 Membrane fabrication for tomography

Samples for tomography analysis were prepared using a silicon back etch method as previously reported.[19] Silicon wafers with silicon nitride coated on both sides were used for sample fabrication. Imaging windows were patterned into the backside nitride and tungsten alignment marks were deposited onto the front side. Then chemical patterns were fabricated on the front side using e-beam lithography and DSA was performed following the procedure

described in the above section. After DSA, the wafer was placed in a protective holder that sealed off the front side polymer film. The setup was then immersed in 30 $wt\%$ potassium hydroxide solution at 90℃. The exposed silicon on the backside was removed until the etching reached the silicon nitride on the front side, creating 30 nm thick membrane imaging windows. The membrane samples were then treated with sequential infiltration synthesis (SIS) to stain the PMMA block with alumina.[16]

4.2.4 Characterization

Scanning electron microscopy (SEM) was performed on a Carl Zeiss Merlin SEM using the InLens detector at 1 kV voltage. Scanning transmission electron microscopy (STEM) tomography was performed on an FEI Tecnai TEM following previously reported procedure.[17] A series of STEM images were acquired at tilt angles ranging from $-68°$ to $+68°$ and reconstructed into a full 3D volume using the Inspect 3D software. 2D slices and cross-sections were then extracted from the 3D volume using ImageJ. AFM measurements were performed on Bruker Multimode 5 AFM in tapping mode. Film thickness measurements were performed on a JA Woollam alpha-SE ellipsometer using the Cauchy model.

4.3 Results and discussion

The process to generate chemical templates for the directed self-assembly (DSA) of block copolymers (BCP) is shown in Figure 4-1.[6,20] Photoresist was coated on top pf a cross-linked polystyrene (X-PS) mat and lithographically patterned into lines and spaces. Then the photoresist lines were trimmed to the desired width and transferred into the X-PS mat using plasma etching. After the resist was stripped, an end-functional P(S-*r*-MMA) brush polymer was coated on the pattern and was annealed to graft to the spaces between X-PS lines. Then excess brush material

was rinsed by solvent to reveal chemical patterns consisting of X-PS guiding stripes and brush-coated backgrounds. BCP film was deposited on the chemical pattern and thermally annealed for different times to self-assemble. The period of the guiding stripes ($L_s = 84\ nm$) is three times of the BCP natural period ($L_0 = 28\ nm$) so the BCP domains are able to interpolate between the guiding stripes and form aligned structures at $3\times$ the density of the original template.

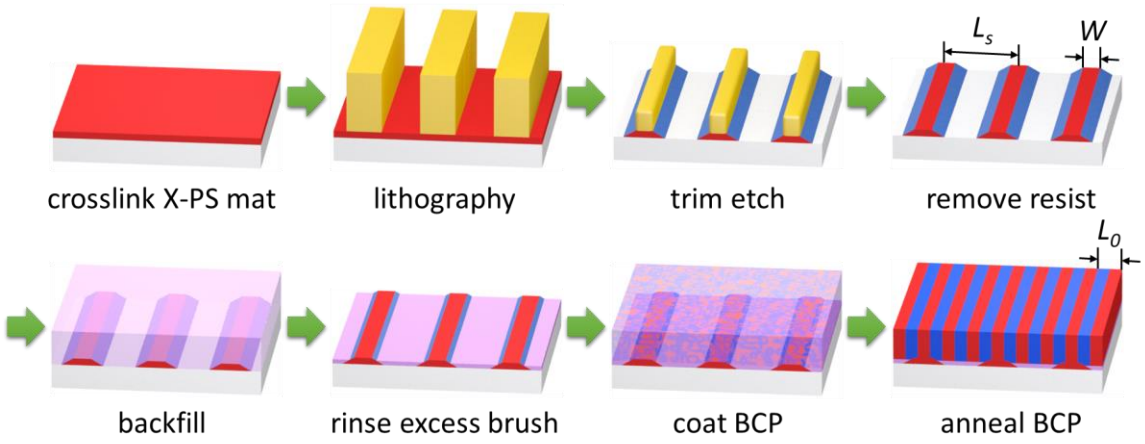

Figure 4-1. Schematic of the process flow for density multiplication DSA. A crosslinked layer of polystyrene mat was coated, patterned and trimmed to form guiding stripes. An end-functionalized random copolymer brush was then coated and grafted in between the guiding stripes over the exposed background region. Excess brush material was subsequently rinsed. Finally the block copolymer was coated onto the chemical pattern and annealed to self-assemble.

The chemoepitaxy process described above, known as the "Line Flow", has been implemented at imec on 300 mm full production equipment. imec has performed extensive optimizations on the Line Flow DSA, focusing on lowering the defectivity at thermal equilibrium. Optimum defect levels were achieved with line width $W = 0.7L_0$ and backfill brush composition of 51% PS.[21,22] These champion conditions will be used as the basis in our study.

We investigated the evolution of structures during the assembly process through arrested annealing studies. Equivalent samples prepared at the same time were annealed on the hot plate for different time durations and immediately quenched to room temperature. The samples were

not reannealed after imaging. Rather than tracking the evolution at a fixed location, the arrested annealing study captures the representative and overall morphologies at different stages of assembly. Annealing temperature of 190℃ was chosen so the assembly process is slow enough that every stage in the structural evolution could be captured.

The assembly process using thermal annealing at 190℃ is shown in Figure 4-2a. Phase separation between PS and PMMA domains starts within 12 s of annealing but the lamellae morphology is not well-formed until after 45 s of annealing. At 5 min, a distinctive "stitched" morphology can be observed in the top-down SEM image, characterized by wide, dark lines along the template direction and short segments oriented orthogonally to the template direction. Small patches of well-aligned domains were also formed. Then from 25 min to 230 min, the stitched defects are gradually annihilated and aligned grains grow. At 620 min, most of the stitched defects are annihilated into aligned domains or disclinations and dislocations. After 1200 min of annealing the domains become fully aligned.

As a comparison, we also studied the assembly at 250℃ which is a commonly used annealing temperature for fast processing (Figure 4-2b). The film is fully aligned within 2 min of annealing, but the evolution of structures is the same as that of the 190℃ annealing. The stitched morphology is first formed and then gradually annihilated. The assembly at 250℃ is very fast, making it hard to capture the onset of phase separation and grain nucleation. For PS-*b*-PMMA, the difference in surface energies of the two blocks is small in the temperature range used here and the Flory-Huggins interaction parameter χ of the material is also relatively insensitive to temperature. By choosing 190℃ annealing, we can better capture the early stages of annealing without altering the assembly process.

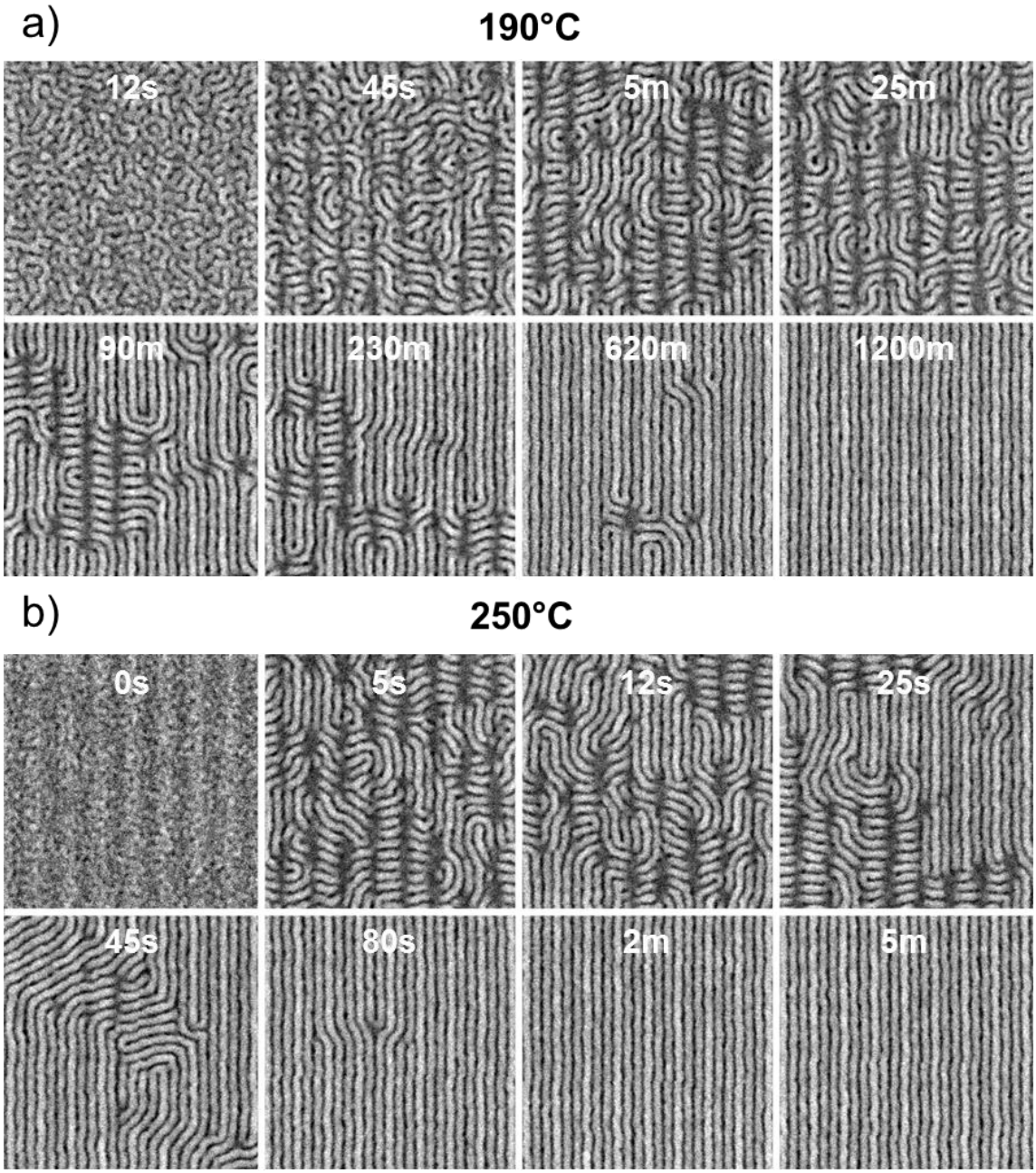

Figure 4-2. SEM images of the kinetic evolution at (a) 190°C and (b) 250°C. Though the speed of assembly is vastly different, the stages of evolution are similar at both temperatures. A characteristic stitched morphology is formed after phase separation and remains for a large portion of the assembly process. The stitched morphology and other defects are eventually annihilated to form fully aligned domains.

Throughout the alignment process, especially during the early stages of annealing, there exists many complex three dimensional structures that essential for understanding the mechanisms of DSA. Previously it has been difficult to characterize such structures experimentally and most of the information comes from molecular simulations.[23] Recently, STEM tomography has been developed to investigate the 3D structures in block copolymer thin films with high resolution[16,17]. Here we used tomography to study the initial structure immediately following phase separation within $12\ s$ of annealing at $190℃$ (Figure 4-3a) and also the stitch morphology formed after $5\ min$ of annealing (Figure 4-3b). The PMMA domains are stained with alumina using sequential infiltration synthesis (SIS) to enhance imaging contrast. Thus the bright domains in the TEM images correspond to PMMA, reversed from the SEM images where the bright domains are PS.

For the initial DSA structure, a clear disconnection between the morphologies at the top versus at the bottom of the film can be seen in the digitally prepared xy slices parallel to the substrate. At the top surface, the BCP shows spinodal-like randomly oriented domains. But right above the guide stripes, domains can be found to form discontinuous lines along the guide stripe direction. Below the surface of the guide stripes, the PMMA domains preferentially wet the oxidized sidewalls and in between the guide stripes PMMA dots can be seen to align in the center of the background region, suggesting that the domains are correctly registered relative to the guide stripes immediately after phase separation. The independent nature of the initial structures formed at the top and the bottom of the film can also be seen in the digitally prepared xz cross-section cut across the guide stripes. The individual cross-sections from each volume were summed along the y direction to obtain high signal-to-noise images. At the bottom of the film, alternating PS and PMMA domains matching the natural periodicity are already registered

relative to the guide stripes. In contrast, the top of the film lacks well-defined features in the summed image due to the random orientations of the domains.

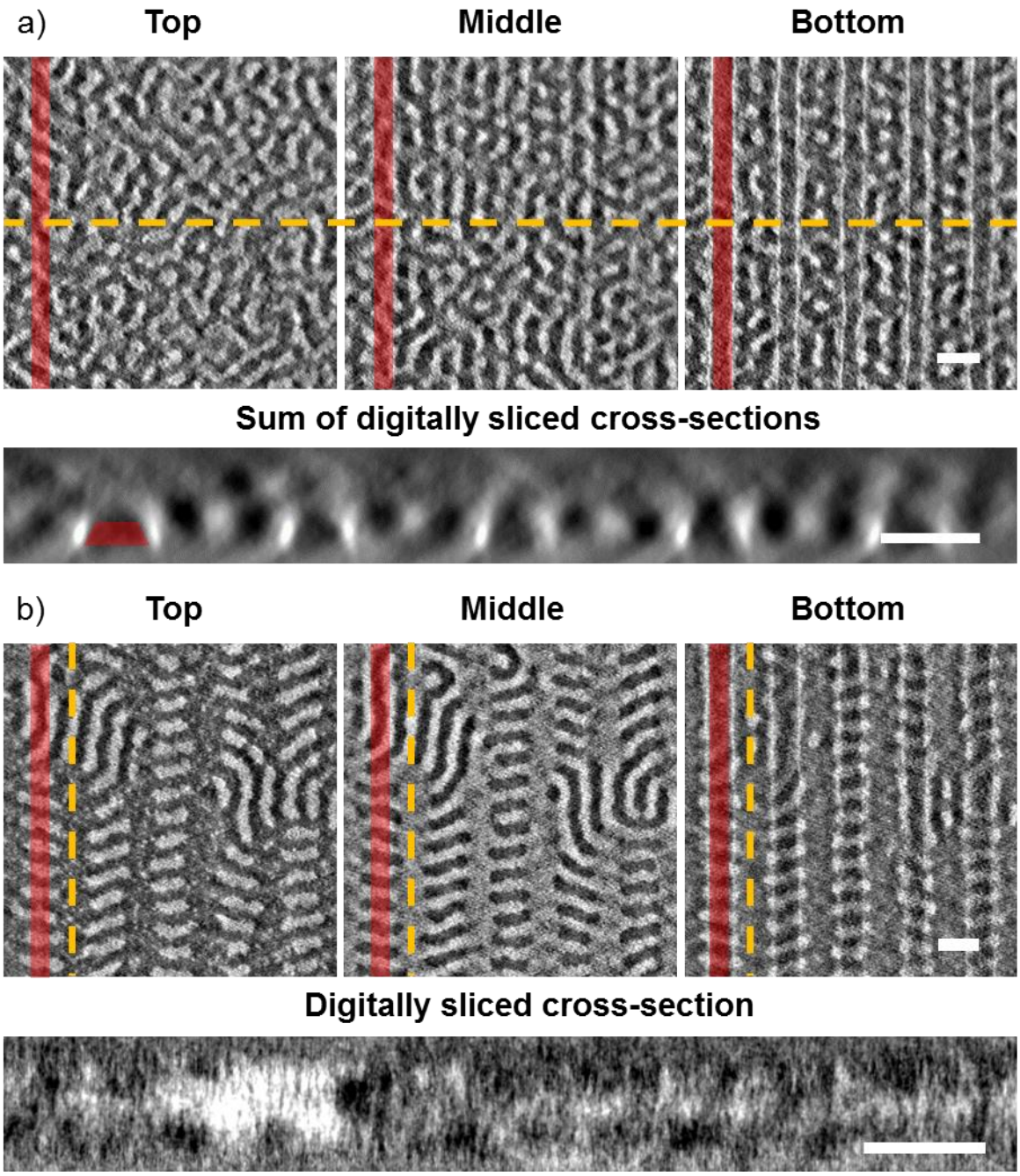

Figure 4-3. TEM tomography of the 3D structures after (a) 12 seconds and (b) 3 minutes of annealing at 190°C. The red stripes mark the location of one of the guiding stripes. The yellow dashes represent the location of cross-section. The cross-section in (a) is summed along the guiding stripes. Scale bars are 50 nm.

Upon further annealing, the stitched morphology is formed and its 3D structure is shown in Figure 4-3b. On top of the X-PS guiding stripe (marked in red), lamellae are oriented perpendicular to the substrate, including both aligned grains and short dashes orientated orthogonal to the guiding stripes. Over the background regions between the guiding stripes, the morphology appears to be featureless in all three xy slices but the color of the region shifts from dark to bright to dark from the top to bottom slices, indicating the formation of PS-PMMA-PS parallel lamellae. The parallel lamellae structure can also be seen in the yz cross-section. The interface between the alternating perpendicular and parallel lamellae resembles a Scherk's first surface, minimizing unfavorable PS-PMMA contact. At the same time, small grains of aligned lamellae that extend through most of the film thickness could also be observed. Interestingly, the lamellae split up into PMMA dots at the bottom, similar to the initial structures formed at the bottom.

The stitched morphology is formed under the influence of the chemical pattern and cannot be observed in the bulk. Structures that are similar to the stitched morphology have been observed previously in chemoepitaxy DSA[24,25], but in those cases the formation of parallel lamellae were driven by the highly preferential regions of the template and perpendicular structures formed over the non-preferential regions, opposite of the stitched structures that we observed. Here the parallel lamellae are over the background region that is only weakly preferential to PMMA and the free surface is also non-preferential to both blocks[20]. The lamellae orientation in thin film is the result of complex interplay among surface energy, interfacial energy and thickness commensurability[26,27], the latter likely plays an important role in the formation of parallel lamella over the background. The top surface of the X-PS has been shown

to be only weakly PS-preferential due to chemical modifications during the backfill step[20]. This explains why perpendicular lamellae could be formed over the guiding stripes.

The stitched morphology persists for a significant portion of the assembly process and represents an undesirable metastable state, unlike simple defects such as dislocations could be resolved relatively quickly. In-situ study of the annihilation of stitched morphology using high speed AFM has found an effective energy barrier of $340\ kJ/K$. Moreover, the orthogonally oriented segments often connect and evolve into large grains of disclinations and dislocations that are hard to annihilate. Therefore it is important to identify key parameters that determine stitch stability so strategies could be designed to optimize the kinetic evolution.

We first investigated the influence of film thickness on the kinetic evolution of structures. The thickness of the BCP film was varied from $0.57L_0$ to $1.64L_0$ while all other DSA parameters were kept the same. The samples were annealed at $190℃$ and the structural evolution during the first $5\ min$ of annealing are shown in Figure 4-4. The speed of alignment is much higher in thinner films. Within $5\ min$, the $0.57L_0$ and $0.75L_0$ films are fully aligned but in films thicker than $1.25L_0$ the aligned grains are only about $200\ nm$ in size. Given the $1200\ min$ required to fully align the $1.25L_0$ film, the assembly in films thinner than $0.75L_0$ is over 200 times faster. The improvement in kinetics is highly disproportionate compared to the 40% reduction in film thickness. In addition to the speed of alignment, the evolution of structures also vary with film thickness. In the range of thicknesses studied here, the evolution could be categorized into 3 distinctive regimes. When film thickness is less than $1.00L_0$, alignment starts within $25\ s$ without the formation of stitched morphology. Dislocations and disclinations are annihilated with further annealing and the films are mostly aligned within $5\ min$. In the second regime where film thickness is between $1.25L_0$ and $1.45L_0$, the stitched morphology are formed in the early

stages and slowly annihilated, following the same evolution described in Figure 4-2. For the $1.64L_0$-thick film, a third mode of structural evolution is observed where a fingerprint pattern is formed without stitch formation but the speed of alignment is similarly slow as that of the second regime.

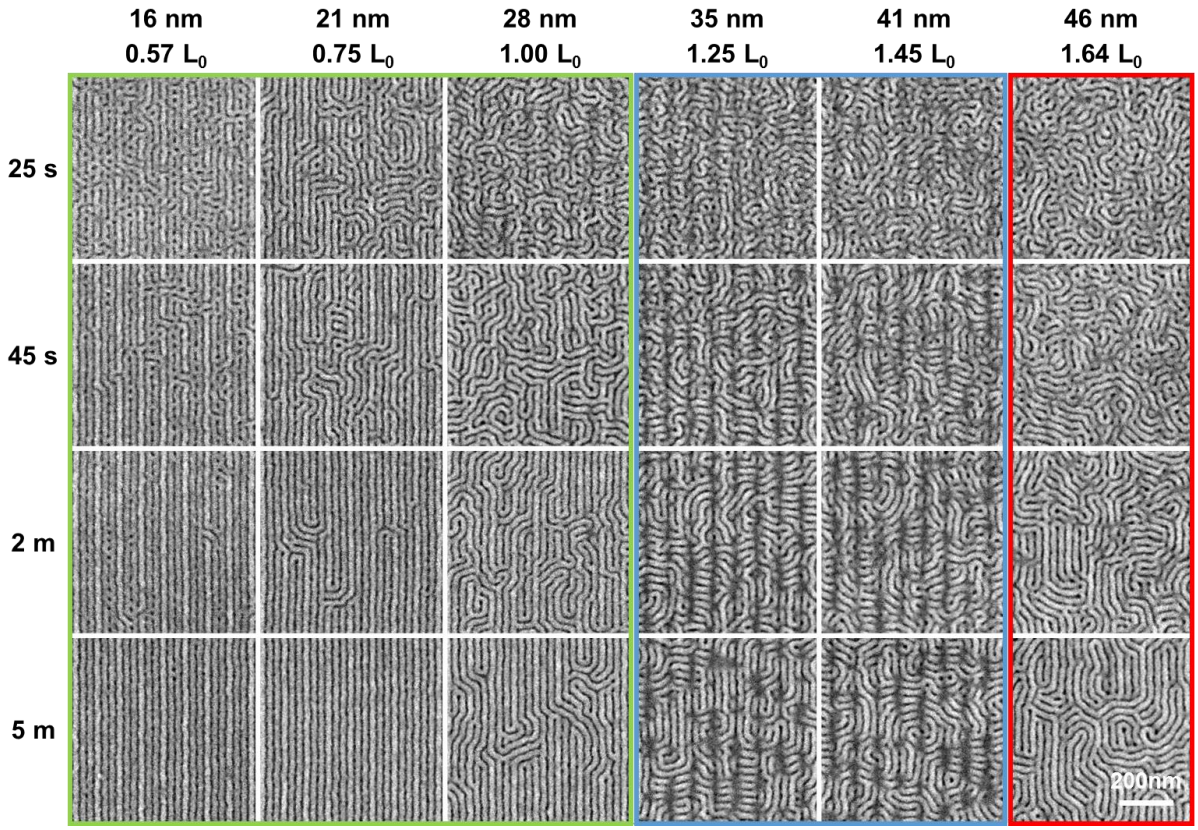

Figure 4-4. Evolution of structures for films with various thicknesses during the first 5 minutes of annealing at 190°C. Films less than 1 L_0 thick are fully aligned under 5 minutes while thicker films have much slower kinetics. The evolution of structures are also different and can be categorized into three regions: thin film region (green), stitched region (blue) and thick film region (red). Scale bar is 200 nm.

The results demonstrate that the stability of stitched morphology and overall DSA kinetics are highly dependent on the film thickness. As film thickness has a large influence on lamellae orientation, changing the film thickness to incommensurate values could disfavor formation of parallel lamellae over the background and in turn destabilize the stitch morphology.

By avoiding the metastable stitched morphology, films thinner than $1.00L_0$ show much faster kinetics. In contrast, there is little improvement in kinetics for the $1.64L_0$-thick film even though no stitched morphology is observed in the SEM. As larger grains with randomly oriented lamellae are first formed at the top surface, the free energy barrier to align the misoriented grains are higher and longer annealing time is required. It is also possible that stitch and other metastable 3D morphologies might still exist inside the film and hinder the alignment process.

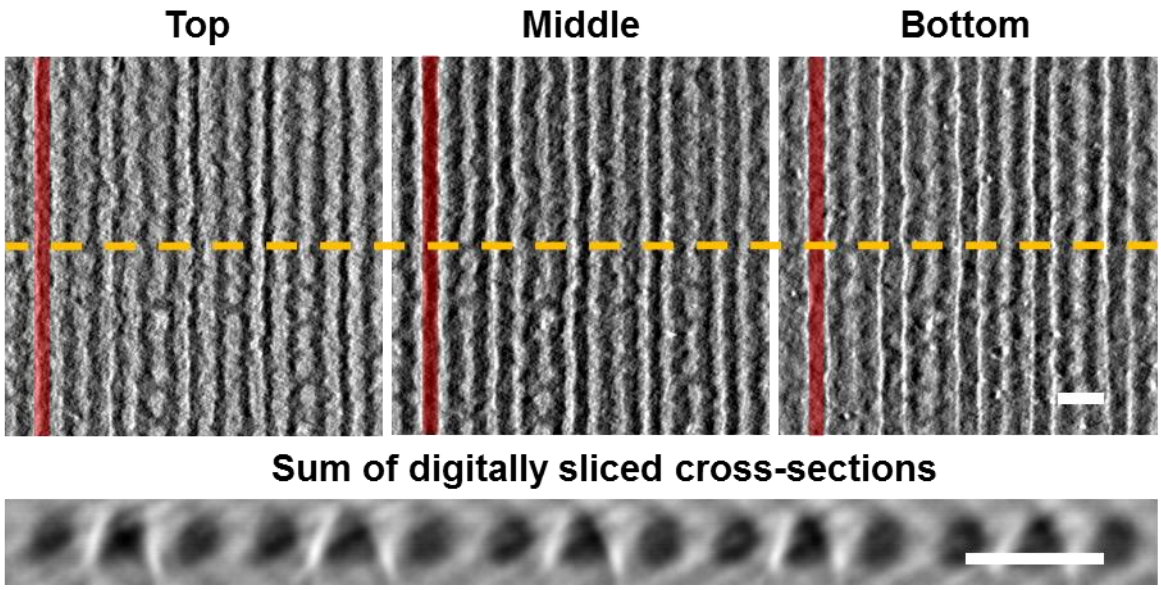

Figure 4-5. TEM tomography of the fully aligned structure at 0.57 L_0 thick showing the microbridge structures. The red stripes mark the location of one of the guiding stripes. The yellow dashes represent the location of cross-section. The cross-section summed along the guiding stripes. Scale bars are 50 nm.

Although reducing the film thickness can greatly improve the kinetics of alignment, there are additional considerations that limit the extent of thickness reduction. First the polymer layer need to be sufficiently thick so the pattern can be transferred into the silicon substrate for semiconductor fabrication. Also, when the film thickness is too thin, there is an increase in the density of PS microbridge defects, as can be seen in the $0.57L_0$ film. We investigated the 3D structure of the microbridge defect with STEM tomography and the results are shown in Figure

4-5. From the digitally prepared xy slices, we can see that the microbridge defects exist through the entire film thickness. The through-film microbridges will be printed onto the silicon substrate after pattern transfer and need to be avoided. It should be noted that there are other types of microbridges that only exist at the bottom of the film and can possibly be eliminated by tuning the etching process during pattern transfer[17,20]. $0.75L_0$ represents the optimal film thickness with fast kinetics and no microbridge defects.

Another DSA parameter we studied is the topography of the template. In the current DSA flow implemented at imec, there is minimum template topography with the top of the X-PS guide stripe only $3.5\ nm$, or $0.14L_0$, higher than the surface of the background brush. Here we increased the topography to $0.27L_0$ and $0.50L_0$ by increasing the thickness of X-PS, while keeping the line width constant at $0.7L_0$ as measured at the top of the guiding stripe. AFM measurement of the template topography after grafting of the backfilling brush is shown in Figure 4-6a. A $1.25L_0$-thick BCP layer is coated on the templates and the morphologies after $25\ s$ and $5\ min$ of annealing at 190℃ are shown in Figure 4-6b. At $25\ s$, the stitched morphology has been nucleated in all samples. The fraction of aligned domains increases with larger topography and the PS domain in the center of the guiding stripe also appears brighter due to increased topography. At the $5\ min$ mark, the control sample is still dominated by stitched domains, while large portions of the $0.27L_0$ and $0.50L_0$ samples are already aligned. Even though the evolution of structures stays the same, increasing the topography greatly enhanced the kinetics of alignment. The 3D structure of the $0.50L_0$-topography sample after DSA is determined by TEM tomography (Figure 4-6c). xy slices show that the lamellae are well-aligned and continuous throughout the thickness of film. The trapezoidal shape of the X-PS guiding stripe can be observed in the digitally sliced cross-section. The angled sidewalls of the guiding

stripes create two PMMA populations with distinct through-film profiles: PMMA domains on the background have a straight profile, whereas PMMA domains on the sidewalls follow the topography of the guiding stripes and taper at the bottom of the film. The lamellae have similar heights after annealing despite of the template topography.

The effect of topography on polymer self-assembly is determined by the commensurability of the topography with polymer periodicity as well as the enthalpic interactions between the polymer and the surfaces. In this case, the geometry of the template is designed to accommodate one PS domain on top of the guiding stripe and five polymer domains in between, satisfying the commensurability condition. Conversely, incommensurate template topography causes the polymer domains to align orthogonally to the topographical features or develop defects due to molecular packing restrictions[17,28,29]. Sidewalls that are non-preferential to the polymer blocks result in orthogonal alignment, whereas highly preferential sidewalls promote alignment along the direction of the template[20,30,31]. The sidewalls of the X-PS guiding stripes have been shown to be PMMA-preferential due to exposure to oxygen plasma during the etching process[20]. Larger topography increases the width of the PMMA-guiding sidewalls, boosting the driving force toward alignment.

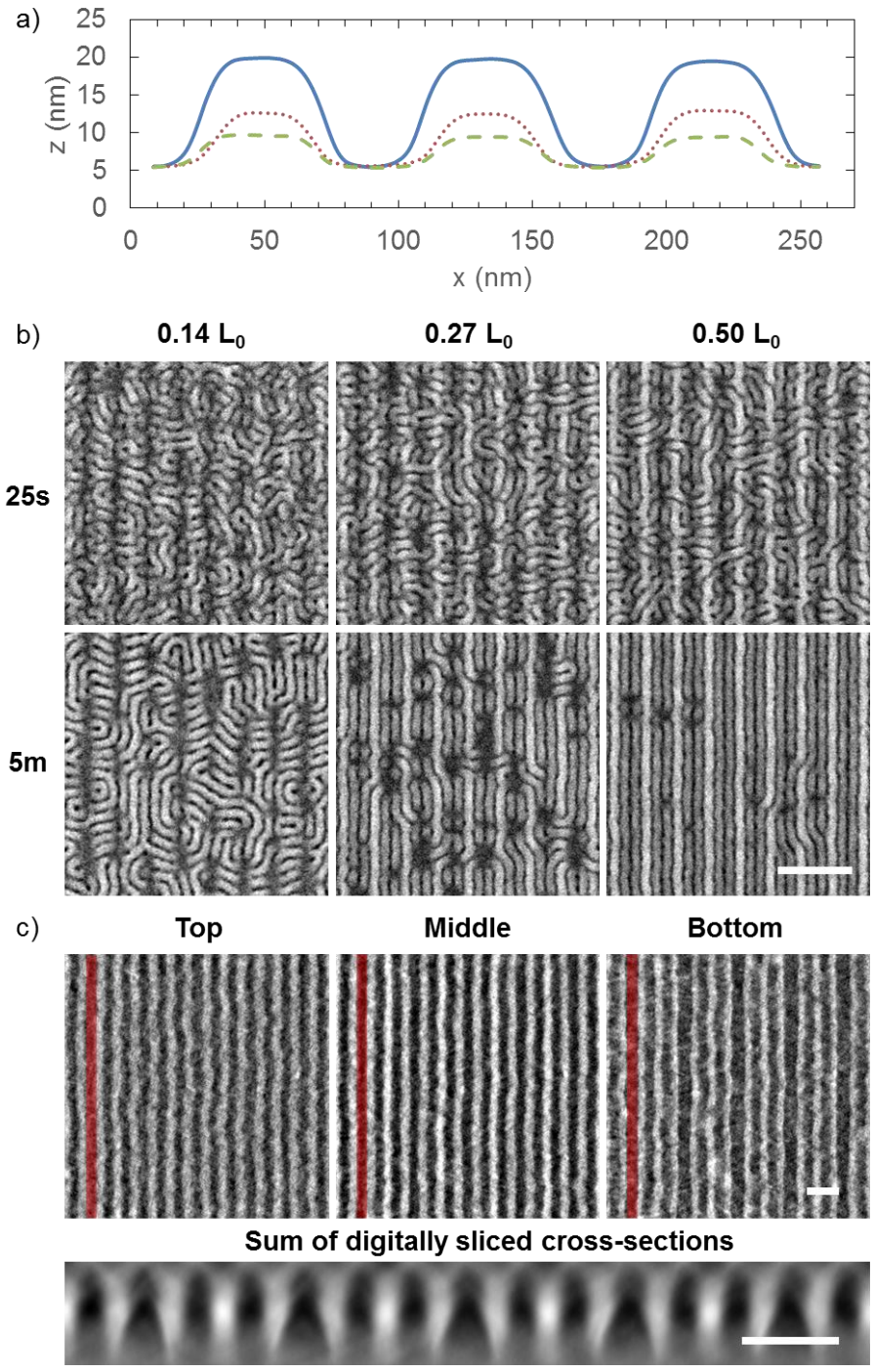

Figure 4-6. Impacts of template topography on DSA kinetics. (a) The averaged cross-sectional profile from AFM measurement for the three template topographies: 0.14 L_0 (dashed green), 0.27 L_0 (dotted red), and 0.50 L_0 (solid blue). (b) The assembly after 25 seconds and 5 minutes of annealing showing that the higher template topography leads to faster alignment. Scale bar is 200 nm. (c) TEM tomography of the assembled film with 0.50 L_0 template topography. Scale bars are 50 nm.

Besides template geometry and film thickness, the chemical composition of the template also plays an important role in DSA where it controls the enthalpic interactions between the polymer and template[32]. Previous work by Rincon *et al.* studied the sensitivity of DSA to different brush chemistries and found that for DSA with $3\times$ density multiplication perfect alignment could only be achieved when the backfill brush is weakly PMMA-preferential[33]. This is due to the fact that there are one more PMMA domain than PS domains over the background region. We investigated the impact of different background chemistries on DSA kinetics. The PS content in the random copolymer brush was varied from weakly PMMA-preferential ($44\sim51\%$) to non-preferential (56%), with 51% being the control. All other parameters were fixed (film thickness $1.25L_0$, template topography $0.14L_0$). The morphology after annealing at 190℃ for $45\ s$, $5\ min$ and $25\ min$ are shown in Figure 4-7. Samples with all four brush compositions exhibit similar kinetics and have the same evolution of structures involving stitch formation. Comparing to the significant impact on DSA kinetics from film thickness and template topography, we conclude that the chemistry of the background region plays a negligible role in determining the stability of stitched morphology and the kinetics of DSA. The findings echo the observation by Rincon *et al.* that brush compositions from $44\sim51\%$ lead to identically sized process windows in guiding stripe widths.

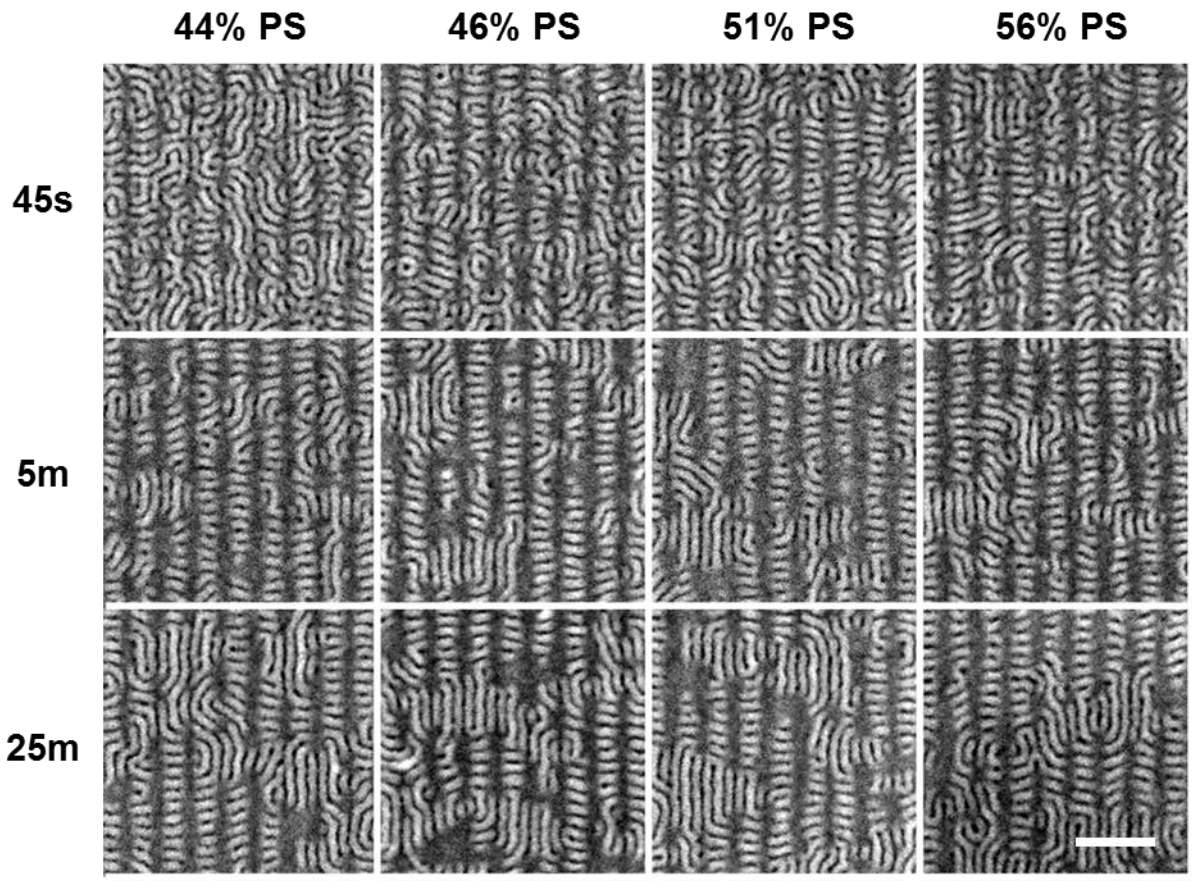

Figure 4-7. Impacts of background chemistry on DSA kinetics. Structural evolution during the first 25 minutes of annealing on 4 different brush compositions shows that the background chemistry does not have a significant impact on the stability of stitched morphology. Scale bars is 200 nm.

Based on the learnings from tuning individual DSA parameters, we studied the DSA kinetics when combining both reduced BCP film thickness and increased template topography. Figure 4-8 shows the structural evolution of a sample with $0.75L_0$ BCP thickness and $0.50L_0$ template topography when annealed at 190℃. There is no stitch formation and a significant portion of the film is already aligned within $25\ s$. At $2\ min$, only a small number of dislocation pairs are left and the defect density has dropped to $\sim 1/\mu m^2$. The polymers are perfectly aligned after $5\ min$ of annealing.

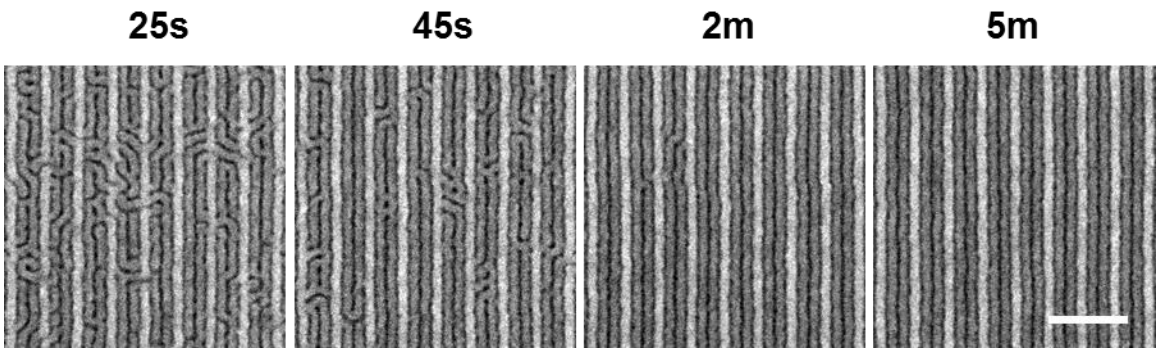

Figure 4-8. Combining 0.75 L_0 film thickness and 0.50 L_0 template topography leads to greatly enhanced kinetics. Scale bars is 200 nm.

A complete picture of the kinetic evolution during the DSA process can be drawn by combining the temporal information from the arrested annealing as well as the three dimensional spatial characterization from tomography. Microphase separation occurs simultaneously throughout the film but different initial structures were formed locally at the top and bottom (Figure 4-3a). Randomly oriented domains are formed at the non-preferential free surface, but chemical and topographical contrast drives immediate alignment in the vicinity of the template. As grains coarsen in all three dimensions, global minimization under the influences of both boundaries lead to the formation of stitched morphology that is different from either of the two initial structures at the top and bottom (Figure 4-3b). There are also grains where the aligned morphology at the template manages to extend to the top surface. We had previously observed in in-situ AFM study that once the through-film alignment is achieved it never relapsed to a defective state due to the large difference in free energy often in excess of hundreds of kT. These aligned grains then gradually grow and the stitched defects are eventually annihilated. This suggests that the initial semi-aligned structures at the bottom are metastable and can evolve into misoriented metastable structures such as the stitch. In contrast, through-film aligned domains

are much lower in energy compared to defective ones and drive the irreversible evolution toward alignment.

For films thinner than $1.00L_0$, the semi-aligned grains are able to influence the morphology at the top surface before large randomly oriented domains are formed. Therefore alignment is quickly achieved throughout the film. The dense microbridges observed in the $0.56L_0$ are reminiscent of the PMMA dots in the initial semi-aligned structures. The thin film thickness allow the PMMA dots to quickly propagate to the top surface, but without the influence of topography confinement and preferential substrate the PMMA dots gradually evolves into through-film lamellae. When film thickness $> 1.5L_0$, the fingerprint patterns formed at the top surface require longer annealing times to resolve. The independent coarsening of grains at the top and bottom of the film when thickness $> 1.5L_0$ has been previously hypothesized and demonstrated[34]. For commensurate templates, the aligned grains at the bottom will grow upward and eventually propagate throughout the film. In Figure 4-3a we have shown that different initial morphologies are formed at the top and bottom independently in thinner films as well. The grains coarsen throughout the film in all three dimensions and when the grain size is comparable with the film thickness the assembly becomes cooperative throughout the film thickness. If large randomly oriented grains are formed before cooperative assembly could be achieved, longer annealing times will be required for alignment due to higher free energy barriers.

The PMMA dots in the initial semi-aligned structure at the bottom of the film represent a metastable non-bulk morphology. The dots are related to the high density microbridges observed in the $0.56\ L_0$ thin film (Figure 4-4) and similar dot structures can also be found at the bottom of the aligned grains among the stitched structures (Figure 4-3b). The dots can evolve into through-

film aligned lamellae or through-film dots as in the $0.56\ L_0$ thin film or become parallel lamellae as in the stitched morphology. The initial structure at the bottom may appear to be highly asymmetric and PS-rich like cylinder forming polymers, but the actual composition should still be mostly symmetric as the PS in the guide stripes comes from the X-PS mat and only the background region in between are occupied by the BCP with 3 PMMA stripes and 2 PS stripes. It is not immediately clear why the PMMA domain in the center of the background is discontinuous and dots-like. Incommensurate topographical confinement likely contributed to the dot formation as the X-PS line width is $W = 0.7\ L_0$ and still wider at the bottom, leaving insufficient space to fit 5 polymer domains in between the guide stripes. Indeed, Williamson *et al.* have previously reported that reducing the space between guide stripes, either by increasing W or reducing L_s, would promote the formation of PS microbridges at the bottom of the film[22]. Counterintuitively, they also found that increasing the PMMA content in the backfilling brush would lead to more PS microbridge formation and likely more PS over the background. We expect that by optimizing the template and annealing conditions continuous and aligned lamellae could be formed immediately at the bottom upon annealing which would in turn lead to faster assembly and less metastable defects.

4.4 Conclusion

We have identified the kinetic evolution of 3D structures during the assembly process in density multiplication DSA. Morphologies are first developed independently at the top and bottom of the film and then evolve cooperatively as grains coarsen. Alignment started at the template interface immediately after annealing whereas the free surface only shows randomly oriented domains. There also exists a metastable "stitched" morphology that represents an undesirable bottleneck in the kinetic evolution. The stitched morphology consists of orthogonally

aligned perpendicular lamellae over the guiding stripes and parallel oriented lamellae over the background region. We demonstrated that by changing the BCP film thickness we could avoid the formation of the metastable stitch and greatly enhance the speed of assembly by over 100x. We also showed that increasing the template topography does not eliminate stitch formation but could expedite the annealing process due to enhanced driving force from PMMA-guiding sidewalls. The combination of arrested annealing and 3D metrologies helps to decipher the fundamental mechanisms governing structural formation and sheds light on the strategy for better pattern design. Through targeted tuning of key DSA parameters, we believe we can engineer the thermodynamic landscape to minimize free energy barriers and ultimately eliminate the defects in DSA.

4.5 References

1. Darling, S. B. Directing the Self-Assembly of Block Copolymers. *Prog. Polym. Sci.* **2007**, *32*, 1152–1204.

2. Jeong, S. J.; Kim, J. Y.; Kim, B. H.; Moon, H. S.; Kim, S. O. Directed Self-Assembly of Block Copolymers for next Generation Nanolithography. *Mater. Today* **2013**, *16*, 468–476.

3. Ji, S.; Wan, L.; Liu, C. C.; Nealey, P. F. Directed Self-Assembly of Block Copolymers on Chemical Patterns: A Platform for Nanofabrication. *Prog. Polym. Sci.* **2016**, *54–55*, 76–127.

4. Segalman, R. A.; Yokoyama, H.; Kramer, E. J. Graphoepitaxy of Spherical Domain Block Copolymer Films. *Adv. Mater.* **2001**, *13*, 1152–1155.

5. Kim, S. O.; Solak, H. H.; Stoykovich, M. P.; Ferrier, N. J.; de Pablo, J. J.; Nealey, P. F. Epitaxial Self-Assembly of Block Copolymers on Lithographically Defined Nanopatterned Substrates. *Nature* **2003**, *424*, 411–414.

6. Liu, C.-C.; Han, E.; Onses, M. S.; Thode, C. J.; Ji, S.; Gopalan, P.; Nealey, P. F. Fabrication of Lithographically Defined Chemically Patterned Polymer Brushes and Mats. *Macromolecules* **2011**, *44*, 1876–1885.

7. Cheng, J. Y.; Sanders, D. P.; Truong, H. D.; Harrer, S.; Friz, A.; Holmes, S.; Colburn, M.; Hinsberg, W. D. Simple and Versatile Methods To Integrate Directed Self-Assembly with

Optical Lithography Using a Polarity- Switched Photoresist. *ACS Nano* **2010**, *4*, 4815–4823.

8. Gronheid, R.; Rincon Delgadillo, P.; Pathangi, H.; Van den Heuvel, D.; Parnell, D.; Chan, B. T.; Lee, Y.-T.; Van Look, L.; Cao, Y.; Her, Y.; *et al.* Defect Reduction and Defect Stability in IMEC's 14nm Half-Pitch Chemo-Epitaxy DSA Flow. In; Resnick, D. J.; Bencher, C., Eds.; 2014; Vol. 9049, p. 904905.

9. Tsai, H.; Pitera, J. W.; Miyazoe, H.; Bangsaruntip, S.; Engelmann, S. U.; Liu, C.; Cheng, J. Y.; Bucchignano, J. J.; Klaus, D. P.; Joseph, E. A.; *et al.* Two-Dimensional Pattern Formation Using Graphoepitaxy of PS- B -PMMA Block Copolymers for Advanced FinFET Device and Circuit Fabrication. *ACS Nano* **2014**, *8*, 5227–5232.

10. Liu, C.-C. C.; Franke, E.; Lie, F. L.; Sieg, S.; Tsai, H.; Lai, K.; Truong, H.; Farrell, R.; Somervell, M.; Sanders, D.; *et al.* DSA Patterning Options for FinFET Formation at 7nm Node. *SPIE Adv. Lithogr.* **2016**, *9777*, 97770R.

11. Li, W.; Müller, M. Directed Self-Assembly of Block Copolymers by Chemical or Topographical Guiding Patterns: Optimizing Molecular Architecture, Thin-Film Properties, and Kinetics. *Prog. Polym. Sci.* **2016**, *54–55*, 47–75.

12. Li, W.; Müller, M. Defects in the Self-Assembly of Block Copolymers and Their Relevance for Directed Self-Assembly. *Annu. Rev. Chem. Biomol. Eng.* **2015**, *6*, 187–216.

13. Hur, S.-M.; Thapar, V.; Ramírez-Hernández, A.; Khaira, G.; Segal-Peretz, T.; Rincon-Delgadillo, P. A.; Li, W.; Müller, M.; Nealey, P. F.; de Pablo, J. J. Molecular Pathways for Defect Annihilation in Directed Self-Assembly. *Proc. Natl. Acad. Sci.* **2015**, *112*, 14144–14149.

14. Li, W.; Nealey, P. F.; de Pablo, J. J.; Müller, M. Defect Removal in the Course of Directed Self-Assembly Is Facilitated in the Vicinity of the Order-Disorder Transition. *Phys. Rev. Lett.* **2014**, *113*, 1–5.

15. Tavakkoli K G, a; Gotrik, K. W.; Hannon, a F.; Alexander-Katz, A.; Ross, C. a.; Berggren, K. K. Templating Three-Dimensional Self-Assembled Structures in Bilayer Block Copolymer Films. *Science* **2012**, *336*, 1294–1298.

16. Segal-Peretz, T.; Winterstein, J.; Doxastakis, M.; Ramírez-Hernández, A.; Biswas, M.; Ren, J.; Suh, H. S.; Darling, S. B.; Liddle, J. A.; Elam, J. W.; *et al.* Characterizing the Three-Dimensional Structure of Block Copolymers via Sequential Infiltration Synthesis and Scanning Transmission Electron Tomography. *ACS Nano* **2015**, *9*, 5333–5347.

17. Segal-Peretz, T.; Ren, J.; Xiong, S.; Khaira, G.; Bowen, A.; Ocola, L. E.; Divan, R.; Doxastakis, M.; Ferrier, N. J.; de Pablo, J. J.; *et al.* Quantitative Three Dimensional Characterization of Block Copolymer Directed Self -Assembly on Combined Chemical and Topographical Pre-Patterned Templates. *ACS Nano* **2016**, acsnano.6b05657.

18. Rincon Delgadillo, P. A. Implementation of a Chemo-Epitaxy Flow for Directed Self-

Assembly on 300-Mm Wafer Processing Equipment. *J. Micro/Nanolithography, MEMS, MOEMS* **2012**, *11*, 31302.

19. Ren, J.; Ocola, L. E.; Divan, R.; Czaplewski, D. A.; Segal-Peretz, T.; Xiong, S.; Kline, R. J.; Arges, C. G.; Nealey, P. F. Post-Directed-Self-Assembly Membrane Fabrication for *in Situ* Analysis of Block Copolymer Structures. *Nanotechnology* **2016**, *27*, 435303.

20. Williamson, L. D.; Seidel, R. N.; Chen, X.; Suh, H. S.; Rincon Delgadillo, P.; Gronheid, R.; Nealey, P. F. Three-Tone Chemical Patterns for Block Copolymer Directed Self-Assembly. *ACS Appl. Mater. Interfaces* **2016**, *8*, 2704–2712.

21. Rincon Delgadillo, P. a.; Gronheid, R.; Lin, G.; Cao, Y.; Romo, A.; Somervell, M.; Nafus, K.; Nealey, P. F. Process Sensitivities in Exemplary Chemo-Epitaxy Directed Self-Assembly Integration. In *Proc. of SPIE*; Tong, W. M.; Resnick, D. J., Eds.; 2013; Vol. 8680, p. 86801H.

22. Williamson, L.; Kim, J.; Cao, Y.; Lin, G.; Gronheid, R.; Nealey, P. F. Impact of BCP Asymmetry on DSA Patterning Performance. *Proc. SPIE* **2015**, *9423*, 942315.

23. Edwards, E. W.; Stoykovich, M. P.; Müller, M.; Solak, H. H.; de Pablo, J. J.; Nealey, P. F. Mechanism and Kinetics of Ordering in Diblock Copolymer Thin Films on Chemically Nanopatterned Substrates. *J. Polym. Sci. Part B Polym. Phys.* **2005**, *43*, 3444–3459.

24. Detcheverry, F. a.; Liu, G.; Nealey, P. F.; de Pablo, J. J. Interpolation in the Directed Assembly of Block Copolymers on Nanopatterned Substrates: Simulation and Experiments. *Macromolecules* **2010**, *43*, 3446–3454.

25. Liu, G.; Detcheverry, F.; Ram??rez-Hern??ndez, A.; Yoshida, H.; Tada, Y.; De Pablo, J. J.; Nealey, P. F. Nonbulk Complex Structures in Thin Films of Symmetric Block Copolymers on Chemically Nanopatterned Surfaces. *Macromolecules* **2012**, *45*, 3986–3992.

26. Suh, H. S.; Kang, H.; Liu, C. C.; Nealey, P. F.; Char, K. Orientation of Block Copolymer Resists on Interlayer Dielectrics with Tunable Surface Energy. *Macromolecules* **2010**, *43*, 461–466.

27. Suh, H. S.; Kang, H.; Nealey, P. F.; Char, K. Thickness Dependence of Neutral Parameter Windows for Perpendicularly Oriented Block Copolymer Thin Films. *Macromolecules* **2010**, *43*, 4744–4751.

28. Kim, H.-C.; Rettner, C. T.; Sundström, L. Fabrication of 20 Nm Half-Pitch Gratings by Corrugation-Directed Self-Assembly. *Nanotechnology* **2008**, *19*, 235301.

29. Hong, S. W.; Huh, J.; Gu, X.; Lee, D. H.; Jo, W. H.; Park, S.; Xu, T.; Russell, T. P. Unidirectionally Aligned Line Patterns Driven by Entropic Effects on Faceted Surfaces. *Proc. Natl. Acad. Sci. U. S. A.* **2012**, *109*, 1402–1406.

30. Park, S. M.; Stoykovich, M. P.; Ruiz, R.; Zhang, Y.; Black, C. T.; Nealey, P. F. Directed

Assembly of Lamellae- Forming Block Copolymers by Using Chemically and Topographically Patterned Substrates. *Adv. Mater.* **2007**, *19*, 607–611.

31. Cushen, J.; Wan, L.; Blachut, G.; Maher, M. J.; Albrecht, T. R.; Ellison, C. J.; Willson, C. G.; Ruiz, R. Double-Patterned Sidewall Directed Self-Assembly and Pattern Transfer of Sub-10 Nm PTMSS- *B* -PMOST. *ACS Appl. Mater. Interfaces* **2015**, *7*, 13476–13483.

32. Liu, C.-C.; Ramírez-Hernández, A.; Han, E.; Craig, G. S. W.; Tada, Y.; Yoshida, H.; Kang, H.; Ji, S.; Gopalan, P.; de Pablo, J. J.; *et al.* Chemical Patterns for Directed Self-Assembly of Lamellae-Forming Block Copolymers with Density Multiplication of Features. *Macromolecules* **2013**, *46*, 1415–1424.

33. Rincon Delgadillo, P. a. Origin of Defects in Directed Self-Assembly of Diblock Copolymers Using Feature Multiplication, University of Chicago, 2014.

34. Welander, A. M.; Craig, G. S. W.; Tada, Y.; Yoshida, H.; Nealey, P. F. Directed Assembly of Block Copolymers in Thin to Thick Films. *Macromolecules* **2013**, *46*, 3915–3921.

CHAPTER 5: PRINCIPLES FOR THREE DIMENSIONAL SELF-ASSEMBLY USING SPHERE-FORMING BLOCK COPOLYMERS

5.1 Introduction

Three dimensional (3D) nanostructures with long-range ordering and perfect registration to the substrate are widely found in modern transistors and metamaterials, and the architectures are crucial for the unique physical properties and device performance [1,2]. Such structures have been typically fabricated through a layer-by-layer process that involves multiple top-down patterning steps and requires meticulous inter-layer alignment. In contrast, block copolymers (BCPs) spontaneously assemble into periodic structures at the nanometer length scale and have the potential to greatly simplify 3D manufacturing[3,4]. Directed self-assembly (DSA) uses lithographically defined templates with chemical contrast (chemoepitaxy)[5–7] or topographical features (graphoepitaxy)[8–10] to guide the assembly of BCP and has been a potential candidate for commercial fabrication of next-generation semiconductors. Although great progress has been made in the past decade to control the ordering and registration of BCP, most of the focus has been on perfecting the two-dimensional (2D) pattern of BCP to transfer onto the underlying substrate and the investigation on controlling the three-dimensional assembly behavior has been rare.

Exploring the fundamental physics governing 3D assembly requires a BCP system that can produce 3D response to the template. Perpendicular cylinders and lamellae are the most-studied morphologies for two-dimensional assemblies but they lack periodic features in the third dimension. In contrast, the spheres formed by highly asymmetric diblock copolymers organize into 3D superlattices and represent a suitable model system for studying 3D assembly. In the

bulk, depending on the polymer chemical composition and molecular architecture, the spheres have been known to arrange into different lattices including BCC, FCC, hexagonal-close-pack (HCP) and Frank-Kasper σ phase[11–13], which have comparable free energies[14,15]. In the thin film, the lattice structure is also highly influenced by the film thickness as well as the interactions at the free surface and the substrate interface. Homogeneous substrates that prefer one of the polymer blocks promote the formation of a wetting layer and non-bulk HCP structures near the interface[16]. As film thickness increases, HCP slowly transitions into the bulk BCC lattice after over 20 layers of spheres. For films with non-preferential wetting conditions, hemispheres are formed on the top and bottom interfaces and the bulk BCC structure could be obtained in thin films containing only 3 layers of spheres[17]. The 3D assembly of spheres could be controlled by graphoepitaxy with "V"-shaped grooves to form face-centered cubic (FCC) lattice[18], but the lattice symmetries and orientations that can be patterned were limited to few template geometries and the template would necessarily remain in the final structure as support. On the other hand, chemoepitaxy uses flat substrates and offers great flexibility in pattern design. Past work showed that when the film thickness matched the size of one unit cell of the body-centered-cubic (BCC) lattice, the BCC (100) plane can be induced to present itself on the film surface and the square array could be distorted isotropically or anisotropically by changing the pattern design[17].

Here we describe a set of guidelines for using 2D chemical patterns to direct the assembly of BCP into a wide variety of single crystalline 3D lattice structures. Rather than precise mathematical descriptions, these are guidelines to determine relative lattice stabilities and furthermore, to deliberately and independently control the crystallographic symmetries and orientations of the 3D lattice. By understanding the dominant interactions responsible for 3D

assembly, this methodology represents a major advance toward 3D structure engineering using BCP DSA.

5.2 Results and discussion

5.2.1 3D DSA by controlling template layout and film thickness

The key hypothesis in this work is that 3D assemblies with different lattice types and orientations are close enough in free energy so the assembly could be dictated by controlling the thin-film boundary conditions and the film thickness. We used poly(styrene-*block*-methyl methacrylate) (PS-*b*-PMMA) diblock copolymer system, which formed PMMA spheres in a BCC lattice in the bulk when annealed at 190°C. As the two components have similar surface energies at the thermal annealing temperatures[19], the free surface is non-preferential to either block and the 3D assembly is therefore controlled by the template design and film thickness. For other copolymer systems with highly different surface energies, the non-preferential boundary condition could be achieved through either solvent vapor annealing[20,21] or top coat approach[22,23]. We used 2D templates with PMMA-wetting spot arrays and PS-wetting background to drive the 3D assembly from the substrate interface. Lithographically controllable variations in template layout allowed us to change the crystallographic symmetries and orientations of the 3D DSA using a single BCP system. For 3D DSA of a specific lattice, two design rules need to be simultaneously satisfied: the template layout needs to match the layout of a plane in the 3D lattice, and additionally, the film thickness needs to be commensurate with the corresponding spacing between neighboring layers of spheres.

We first demonstrate the DSA strategy with assemblies containing three layers of spheres. In a typical experiment, spot arrays were patterned on the crosslinked PS layer with e-

beam lithography and then treated with oxygen plasma to become PMMA preferential. BCP was then spin-coated and soft baked at 80°C to remove the residual solvent. Finally the film was thermally annealed at 190°C for 12 h. To confirm the 3D structure, an in-situ back etch method was used to prepare DSA samples on silicon nitride membrane for TEM characterization[24].

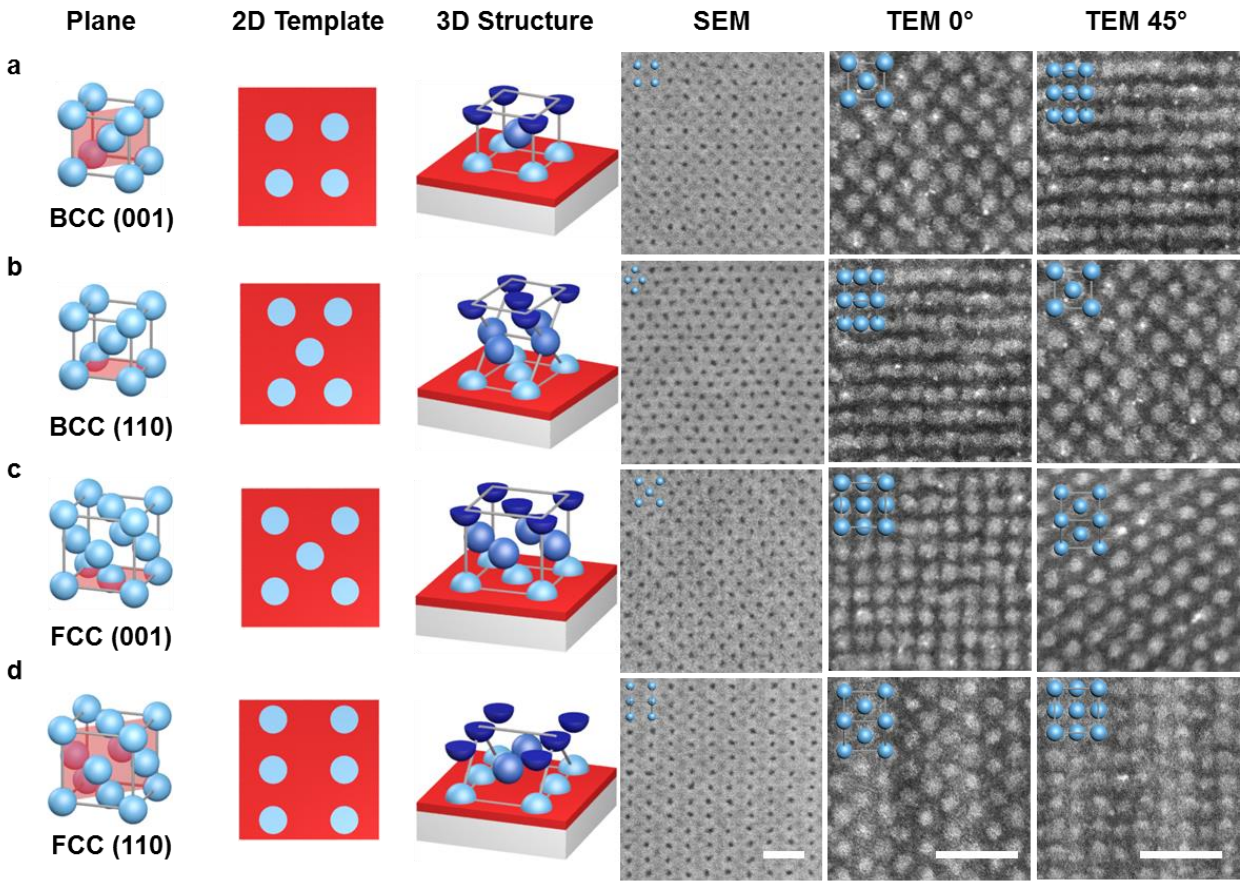

Figure 5-1. 3D DSA by controlling template layout and film thickness. a-d, Chemoepitaxy of PS-*b*-PMMA spheres in BCC<001>, BCC<110>, FCC<001> and FCC<110> orientations with three layers of spheres. In each row from left to right, the panels correspond to: a unit cell showing the target plane, the 2D layout of the template matching the plane, the 3D structure of the sphere lattice assembled on the template, top down SEM of the assembled sample, along with TEM images of the assembled film taken at 0° and 45° sample tilt. For clarity, the PS domain has been removed in the schematics. In the 3D DSA schematics, spheres on different layers were colored in different shades of blue. The insets on the electron microscopy images show the expected structures. Scale bars are 100 nm.

The lattice parameter of the bulk BCC lattice, defined as the edge length in the cubic unit cell, is determined by small angle X-ray scattering to be $L_{BCC} = 40.1$ nm. In the case of BCC <001> DSA (Figure 5-1a), the template consisted of a square array of spots with pitch $L_s = L_{BCC}$, matching the layout of the BCC (001) plane in the bulk. The BCP film had a thickness of $t = L_{BCC}$ and therefore contained 3 layers of spheres. After annealing, SEM image of the top surface showed the BCC (001) pattern and 2D TEM images at 0° and 45° sample tilt were in perfect agreement with the projections of BCC <001> and BCC <110> orientations respectively, proving that the structure was indeed the BCC lattice in <001> orientation. The orientation of the bulk lattice can be manipulated by matching the template and the film thickness to those of the corresponding lattice planes. For BCC <110> (Figure 5-1b), the template represented a centered rectangular symmetry with the sides being L_{BCC} and $\sqrt{2}L_{BCC}$. The film thickness that corresponded to three layers of spheres was $\sqrt{2}L_{BCC}$.

To control the lattice type and direct the assembly of a non-bulk lattice, we first need to determine the optimum lattice parameter for a given polymer molecular weight. Here we assume that the size of the sphere in a non-bulk lattice is the same as that in the bulk BCC. Then the lattice parameter can be calculated by invoking the constraint of the constant volume fraction of spheres. In the case of FCC, the lattice parameter should be $L_{FCC} = \sqrt[3]{2}L_{BCC} = 50.5$ nm. Therefore, FCC lattice in the <001> orientation (Figure 5-1c) can be assembled by using template resembling a square symmetry rotated 45° with pitch $L_s = L_{FCC}/\sqrt{2}$ and controlling the film thickness to be $t = L_{FCC}$. Similar to BCC, the non-bulk FCC can also be oriented in different directions in the film and the DSA of FCC <110> is demonstrated in Figure 5-1d.

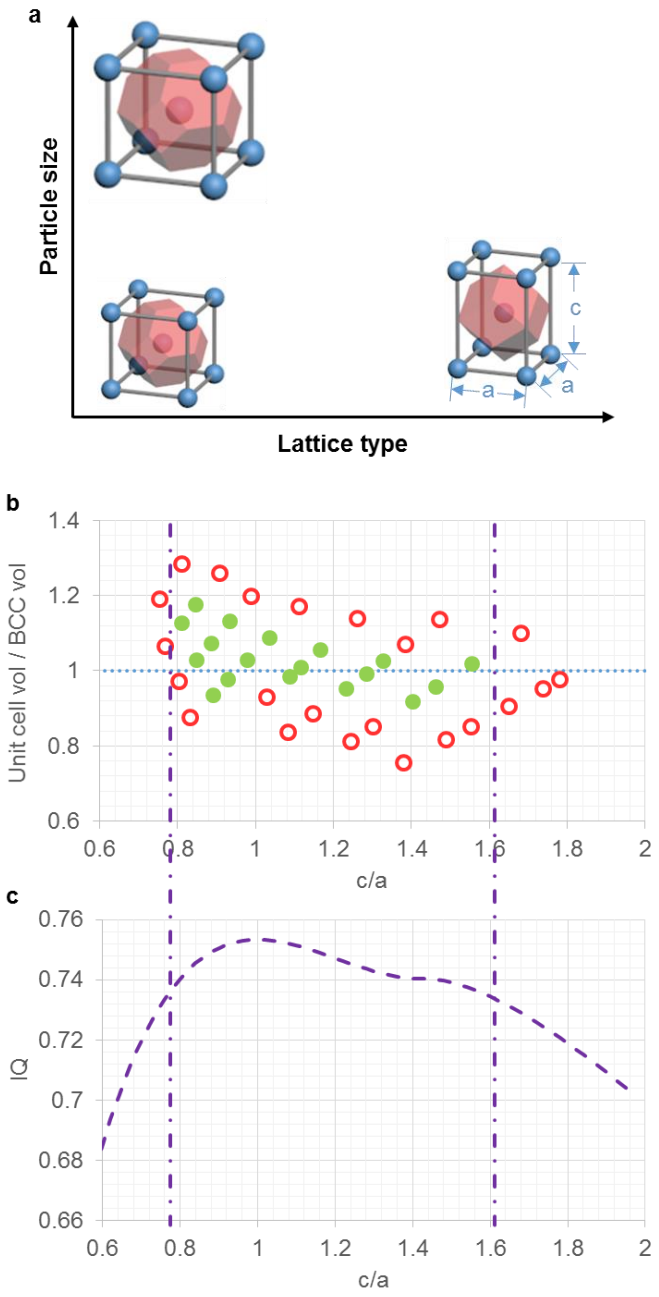

Figure 5-2. Controlling crystallographic symmetries with 3D DSA. a, The DSA of different body-centered-tetragonal lattices were studied by varying template design and film thickness. The equivalent BCT unit cells of BCC and FCC were shown along with the Wigner-Seitz cells of the center spheres. b, Normalized phase diagram of unit cell volume versus lattice type showing the DSA process window where filled green dots represent well-ordered DSA and empty red dots represent films with terracing or random ordering. Blue dotted line signifies lattices with the same unit cell volume as that of the bulk BCC. c, Sphericity of the Wigner-Seitz cells for different lattice symmetries as measured by isoperimetric quotient. The doted lines represents the boundary of the process window in b.

5.2.2 Stability of different lattice types and unit cell sizes

The 3D DSA is not limited to BCC and FCC lattices. Rather than testing every possible lattices, we look to generalize and establish the rules governing which lattice types can be achieved in DSA. BCC and FCC are closely related to the body-centered-tetragonal (BCT) lattice, with a square base ($a \times a$) and height (c) (Figure 5-2a). We systematically investigated a series of BCT <001> assemblies by using patterns of square arrays with pitch $L_s = a$ from 33 nm to 45 nm and BCP film thicknesses $t = c$ from 35 nm to 60 nm. The results were categorized by whether well-ordered and defect-free structures were obtained (filled green) or not (open red) (Figure 5-2b). In the normalized plot, the horizontal axis, c/a, signifies the type of the lattice and the vertical axis is the unit cell volume over that of the bulk BCC unit cell, $a^2c/{L_{BCC}}^3$, representing the size of the lattice. A process window clearly exists. In the vertical direction, DSA was only possible between 0.92 and 1.18 for the normalized volume of the unit cell, implying that the volume was mostly constant (blue dash line). Because all BCT unit cells contain 2 spheres and the volume fraction of polymer is constant, it must dictate that the volume of the spheres were constant, validating our previous hypothesis. Although enthalpic interactions favor an increase in sphere size as it would reduce the interfacial area per chain between the two blocks, entropic contributions keep the sphere size constant to avoid penalties induced by chain stretching or compression. This rule can be used to estimate the optimum lattice parameter for templating non-bulk lattices. As the bulk lattice parameter scales with the two-thirds power of BCP molecular weight, stable lattices with different unit cell sizes could be achieved by tuning polymer chain length[3].

The constraint on crystallographic symmetries, on the other hand, was found to be $0.8 < c/a < 1.6$. It arises from the competition between the preferred spherical shape for individual

particles and the restrictions on particle shape imposed by the templated lattice symmetry. The further away a particle deviates from spherical shape, the more materials will have to be redistributed to uniformly fill space, invoking penalties in free energy. The particle shape for a given lattice symmetry can be captured by the sphericity of its Wigner-Seitz cells[25]. Sphericity is quantified by the isoperimetric quotient (IQ), defined as $IQ = 36\pi V^2/S^3$, where V and S are the volume and surface area of Wigner-Seitz cells, respectively. IQ ranges from 0 to 1 with $IQ = 1$ indicating a perfect sphere. We calculated the IQ of the Wigner-Seitz cells for different BCT lattices with c/a from 0.6 to 2 (Figure 5-2c). The IQ reached a maximum of 0.7534 when $c/a = 1$, representing the BCC lattice. This means that BCC requires the least amount of chain stretching and explains why it is the preferred morphology in the bulk. IQ dropped monotonically as c/a diverged from 1, but there was a shoulder at $c/a = \sqrt{2}$, resembling the FCC lattice, with $IQ = 0.7405$. Outside of $1 \leq c/a \leq \sqrt{2}$, the sphericity quickly decreased. By mapping the range of c/a where perfect registration was achieved (purple dash) onto the IQ curve, it can be established that the cut offs at both ends of the spectrum correspond to $IQ \sim 0.735$. This minimum sphericity represents a limit to the amount of distortions in particle shape that can be allowed and sets a boundary for the range of lattice types available for DSA.

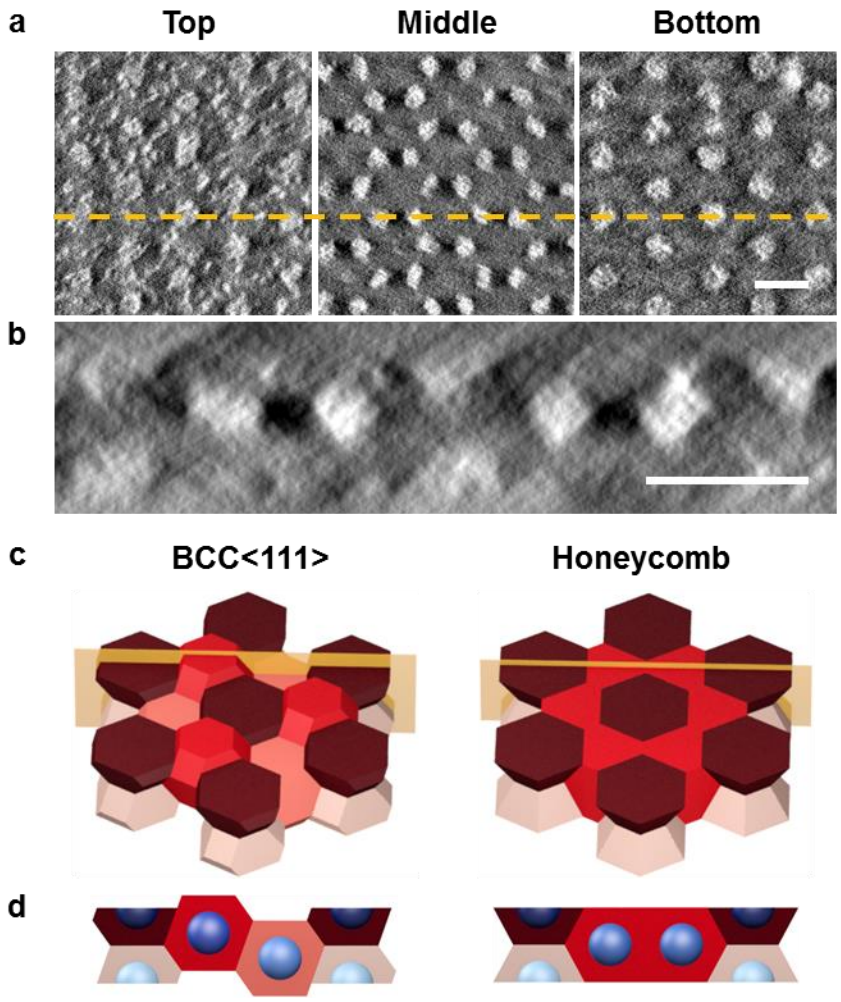

Figure 5-3.Formation of honeycomb lattice through lattice distortion. a, In-plane slices created from TEM tomography showing the hexagonal symmetries at the top and bottom layers and the honeycomb symmetry in the middle layer. b, Digitally sliced cross-section along the golden dashed line in a showing the three-layer honeycomb lattice. c, 3D schematics of BCC<111> and honeycomb lattice showing the arrangements of the Wigner-Seitz cells. Cells at different layers are colored with different shades of red. d, Cross-section along the golden plane in c showing the uneven surfaces of BCC<111> versus the flat surfaces of honeycomb lattice. Scale bars are 50 nm.

5.2.3 Surface induced lattice deformation

The control of lattice orientations is achieved on the premise that the free energies of the BCP stay constant for different orientations. This is true in the bulk as neither the chain configurations nor the interface between the blocks are affected by lattice rotations. In thin film, the confinements at the substrate interface and free surface break the symmetry and the energy of the DSA system becomes dependent on orientation. In the case of BCC <111>, the template was a large hexagonal pattern with center-to-center distance of $\sqrt{2}L_{BCC}$ and the corresponding spacing between each layer was $\sqrt{3}L_0/6$. The hexagonal pattern matching BCC (111) could be obtained at the top surface only when the DSA film thickness was $\sqrt{3}L_{BCC}/2$, corresponding to 3 spacings and presumably containing 4 layers of hexagonally arranged spheres. Interestingly, TEM tomography[26] revealed that the film consisted of 3 layers of spheres: a center layer resembling a honeycomb pattern was sandwiched between two hexagonal layers of hemispheres at the top and bottom (Figure 5-3a). A digitally sliced cross-section (Figure 5-3b) shows that the spheres on the top and bottom layers sat in the center of the 6-member rings of the honeycomb layer. Comparing this unique honeycomb lattice to the BCC lattice with 4 layers of spheres, the top and bottom layers are the same for both lattices but the two middle layers of the BCC lattice "merged" into one layer in the honeycomb lattice. The preference for the honeycomb lattice over the BCC can be understood by analyzing the chain stretching under thin film confinements, visualized by Wigner-Seitz cells (Figure 5-3c). If the spheres were to adopt the BCC symmetry and the corresponding Wigner-Seitz cells, the resulting structure would not have flat surfaces at the top and bottom as the two middle layers protrude from one surface and correspondingly depress from the other (Figure 5-3d). To maintain BCC <111> orientation under thin film confinements, the PS corona of the two middle layers would need significant redistribution to

compensate for the $\sqrt{3}L_{BCC}/12$ offsets. Assuming that the length of the polymer chain is $\sim 0.5L_{BCC}$, the distortion corresponds to ~30% change in chain length, invoking heavy entropic penalties. Instead, the spheres abandoned the BCC symmetry and "shifted" the two middle layers to form one honeycomb layer. For the honeycomb lattice, two species of Wigner-Seitz cells were formed: the honeycomb layer had a volume of 0.9868 V_{BCC} and a sphericity of 0.7034; the top and bottom layers consisted of half cells, but the corresponding full cells would have a volume of 1.0264 V_{BCC} and sphericity of 0.7788. As the sphere population of the honeycomb layer is twice of that of the hexagonal layers, the overall sphericity of the system can be estimated by a weighted average of 0.7285, close to the edge of the sphericity window that we established using the BCT lattices. This transition in lattice symmetry greatly reduced the entropic penalty and was necessary for successful DSA. It demonstrated the rule that DSA is only possible for lattice orientations that satisfy the confinement of the thin film interfaces, as manifested by a flat surface formed by the Wigner-Seitz cells.

5.2.4 Quantized behavior in thickness and the assembly in thick films

To fully exploit the potential of 3D DSA, we investigated the ability of the template pattern to propagate through substantial thickness. BCP films were assembled with thicknesses from 15 nm to 144 nm in ~4 nm intervals on templates matching BCC (001) and FCC (001) patterns respectively. The results show that for both templates good registration and ordering were only achieved at quantized film thicknesses (Figure 5-4a). When the thickness was not commensurate with the layer spacings for the corresponding template, the assembly either lacked long range order or formed hole-island structures with well-ordered arrays offset by one layer. The width of the assembly windows stayed relatively constant at less than $\pm 5\ nm$ even as the number of layers increased, despite of less distortion per chain. This is because as the film

thickness increased from a commensurate value the Wigner-Seitz cells had to be elongated and enlarged to fill the space with the same number of layers, changing both the lattice symmetry and size of the unit cell. The films responded by terracing or forming randomly ordered structures to minimize the entropic penalties. This quantized behavior in thickness is analogous to the observation in graphoepitaxy of spheres that good ordering was only possible when the trench width was commensurate with the row to row distance[27,28]. It should also be noted that, in the case of FCC <001>, there was a slight mismatch between the expected thickness (green dashed lines) and the actual assembly window, more obvious in films thicker than 100 nm. The observed layer spacing was 23.9 nm compared to the expected value of $0.5\ L_{FCC} = 25.3\ nm$, representing a 6% difference. This is partly because that the calculated layer spacing is based on the assumption of constant sphere volume for non-bulk lattices, which is an approximation and can cause small deviations. Another possible contribution is that our e-beam lithography system can only vary template pitches in 1 nm resolution so a slightly smaller lattice parameter in the thickness direction is expected when the pitch is rounded up.

When the commensurability requirement is satisfied, DSA can propagate through very thick films for both bulk and non-bulk lattices. At 294.4 nm, both BCC <001> and FCC <001> were assembled in the same film with perfect ordering and registration (Figure 5-4b). This thickness corresponds to 15 and 12 layers of spheres for BCC <001> and FCC <001> patterns respectively. In contrast, in the case of self-assembled films on non-preferential substrates, only the BCC lattice was observed in films more than 6 layers thick. The perfection of non-bulk lattice in thick film showcases the ability of the 2D chemical pattern to dictate the 3D structure of BCP assembly. It is plausible though that the non-bulk lattice will eventually fail to propagate as the entropic penalty to sustain the non-bulk lattice increases with thickness.

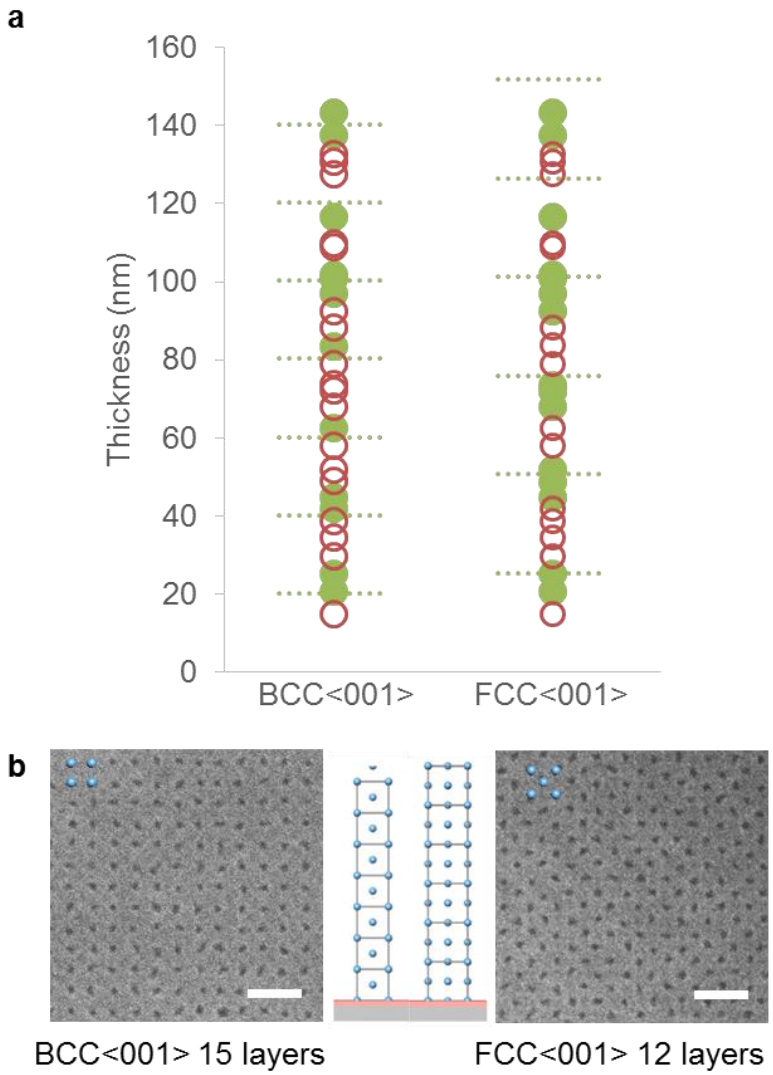

Figure 5-4. DSA of BCC<001> and FCC<001> through thick films. a, DSA of BCC<001> and FCC<001> lattices with different film thicknesses. Well-ordered structures (filled green dots) were only achieved when film thickness was commensurate with the corresponding layer spacing (green dashed lines). b, Top down SEM images of BCC<001> and FCC<001> DSA in 294 nm-thick film. Scale bars are 100 nm.

5.3 Conclusion

We have demonstrated a set of design rules for controlling the 3D assembly of BCP spheres using 2D chemical templates. These rules allow us to dictate the crystallographic symmetries, orientations and unit cell sizes of 3D lattices with single crystalline domain and

perfect registration over arbitrarily large areas and through macroscopic thicknesses. The highly-ordered and tailorable superlattices of nanoparticles have potential applications in photonic and plasmonic material design[29,30]. Functionalization of the spheres could be achieved by tuning the polymer chemistry[18,31] or converting the spheres to metal or metal oxides after assembly through sequential infiltration synthesis (SIS)[32] or immersion in anionic metal solutions[33]. More generally, the understanding gained from these rules will facilitate the design of DSA strategies for other BCP morphologies with 3D lattice structures, such as gyroid and perforated lamellae, where similar sets of design rules might be applicable.

5.4 References

1. *Design of 3D Integrated Circuits and Systems*; Sharma, R., Ed.; CRC Press, 2014.

2. Liu, N.; Guo, H.; Fu, L.; Kaiser, S.; Schweizer, H.; Giessen, H. Three-Dimensional Photonic Metamaterials at Optical Frequencies. *Nat. Mater.* **2008**, *7*, 31–37.

3. Bates, F. S.; Fredrickson, G. H. Block Copolymers—Designer Soft Materials. *Phys. Today* **1999**, *52*, 32.

4. Ross, C. a.; Berggren, K. K.; Cheng, J. Y.; Jung, Y. S.; Chang, J.-B. Three-Dimensional Nanofabrication by Block Copolymer Self-Assembly. *Adv. Mater.* **2014**, 4386–4396.

5. Kim, S. O.; Solak, H. H.; Stoykovich, M. P.; Ferrier, N. J.; de Pablo, J. J.; Nealey, P. F. Epitaxial Self-Assembly of Block Copolymers on Lithographically Defined Nanopatterned Substrates. *Nature* **2003**, *424*, 411–414.

6. Liu, C.-C.; Ramírez-Hernández, A.; Han, E.; Craig, G. S. W.; Tada, Y.; Yoshida, H.; Kang, H.; Ji, S.; Gopalan, P.; de Pablo, J. J.; *et al.* Chemical Patterns for Directed Self-Assembly of Lamellae-Forming Block Copolymers with Density Multiplication of Features. *Macromolecules* **2013**, *46*, 1415–1424.

7. Ji, S.; Wan, L.; Liu, C. C.; Nealey, P. F. Directed Self-Assembly of Block Copolymers on Chemical Patterns: A Platform for Nanofabrication. *Prog. Polym. Sci.* **2016**, *54–55*, 76–127.

8. Segalman, R. A.; Yokoyama, H.; Kramer, E. J. Graphoepitaxy of Spherical Domain Block Copolymer Films. *Adv. Mater.* **2001**, *13*, 1152–1155.

9. Bita, I.; Yang, J. K. W.; Jung, Y. S.; Ross, C. a.; Thomas, E. L.; Berggren, K. K.

Graphoepitaxy of Self-Assembled Block Copolymers on Two-Dimensional Periodic Patterned Templates. *Science* **2008**, *321*, 939–943.

10. Tsai, H.; Pitera, J. W.; Miyazoe, H.; Bangsaruntip, S.; Engelmann, S. U.; Liu, C.; Cheng, J. Y.; Bucchignano, J. J.; Klaus, D. P.; Joseph, E. A.; *et al.* Two-Dimensional Pattern Formation Using Graphoepitaxy of PS- B -PMMA Block Copolymers for Advanced FinFET Device and Circuit Fabrication. *ACS Nano* **2014**, *8*, 5227–5232.

11. Bates, F. S.; Cohen, R. E.; Berney, C. V. Small-Angle Neutron Scattering Determination of Macrolattice Structure in a Polystyrene-Polybutadiene Diblock Copolymer. *Macromolecules* **1982**, *15*, 589–592.

12. Lee, S.; Bluemle, M. J.; Bates, F. S. Discovery of a Frank-Kasper Phase in Sphere-Forming Block Copolymer Melts. *Science (80-.).* **2010**, *330*, 349–353.

13. Matsen, M. W. Effect of Architecture on the Phase Behavior of AB-Type Block Copolymer Melts. *Macromolecules* **2012**, *45*, 2161–2165.

14. Arora, A.; Qin, J.; Morse, D. C.; Delaney, K. T.; Glenn, H.; Bates, F. S.; Dorfman, K. D. Broadly Accessible SCFT for Block Polymer Materials Discovery. **2016**, 1–52.

15. Thomas, E. L.; Kinning, D. J.; Alward, D. B.; Henkee, C. S. Ordered Packing Arrangements of Spherical Micelles of Diblock Copolymers in Two and Three Dimensions. *Macromolecules* **1987**, *20*, 2934–2939.

16. Stein, G. E.; Kramer, E. J.; Li, X.; Wang, J. Layering Transitions in Thin Films of Spherical-Domain Block Copolymers. *Macromolecules* **2007**, *40*, 2453–2460.

17. Ji, S.; Nagpal, U.; Liao, W.; Liu, C.; de Pablo, J. J.; Nealey, P. F. Three-Dimensional Directed Assembly of Block Copolymers Together with Two-Dimensional Square and Rectangular Nanolithography. *Adv. Mater.* **2011**, *23*, 3692–3697.

18. Chuang, V. P.; Cheng, J. Y.; Savas, T. a; Ross, C. a. Three-Dimensional Self-Assembly of Spherical Block Copolymer Domains into V-Shaped Grooves. *Nano Lett.* **2006**, *6*, 2332–2337.

19. Mansky, P.; Liu, Y.; Huang, E.; Russell, T. P.; Hawker, C. J. Controlling Polymer-Surface Interactions with Random Copolymer Brushes. *Science (80-.).* **1997**, *275*, 1458–1460.

20. Xiong, S.; Wan, L.; Ishida, Y.; Chapuis, Y.-A.; Craig, G. S. W.; Ruiz, R.; Nealey, P. F. Directed Self-Assembly of Triblock Copolymer on Chemical Patterns for Sub-10-Nm Nanofabrication via Solvent Annealing. *ACS Nano* **2016**, *10*, 7855–7865.

21. Gu, X.; Gunkel, I.; Hexemer, A.; Gu, W.; Russell, T. P. An In Situ Grazing Incidence X-Ray Scattering Study of Block Copolymer Thin Films During Solvent Vapor Annealing. *Adv. Mater.* **2014**, *26*, 273–281.

22. Bates, C. M.; Seshimo, T.; Maher, M. J.; Durand, W. J.; Cushen, J. D.; Dean, L. M.;

Blachut, G.; Ellison, C. J.; Willson, C. G. Polarity-Switching Top Coats Enable Orientation of Sub-10-Nm Block Copolymer Domains. *Science* **2012**, *338*, 775–779.

23. Yoshida, H.; Suh, H. S.; Ramirez-Hernandez, A.; Lee, J. I.; Aida, K.; Wan, L.; Ishida, Y.; Tada, Y.; Ruiz, R.; de Pablo, J.; *et al.* Topcoat Approaches for Directed Self-Assembly of Strongly Segregating Block Copolymer Thin Films. *J. Photopolym. Sci. Technol.* **2013**, *26*, 55–58.

24. Ren, J.; Ocola, L. E.; Divan, R.; Czaplewski, D. A.; Segal-Peretz, T.; Xiong, S.; Kline, R. J.; Arges, C. G.; Nealey, P. F. Post-Directed-Self-Assembly Membrane Fabrication for *in Situ* Analysis of Block Copolymer Structures. *Nanotechnology* **2016**, *27*, 435303.

25. Lee, S.; Leighton, C.; Bates, F. S. Sphericity and Symmetry Breaking in the Formation of Frank–Kasper Phases from One Component Materials. *Proc. Natl. Acad. Sci.* **2014**, *111*, 17723–17731.

26. Segal-Peretz, T.; Ren, J.; Xiong, S.; Khaira, G.; Bowen, A.; Ocola, L. E.; Divan, R.; Doxastakis, M.; Ferrier, N. J.; de Pablo, J. J.; *et al.* Quantitative Three Dimensional Characterization of Block Copolymer Directed Self -Assembly on Combined Chemical and Topographical Pre-Patterned Templates. *ACS Nano* **2016**, acsnano.6b05657.

27. Cheng, J. Y.; Mayes, A. M.; Ross, C. A. Nanostructure Engineering by Templated Self-Assembly of Block Copolymers. *Nat. Mater.* **2004**, *3*, 823–828.

28. Cheng, J. Y.; Zhang, F.; Chuang, V. P.; Mayes, A. M.; Ross, C. A. Self-Assembled One-Dimensional Nanostructure Arrays. *Nano Lett.* **2006**, *6*, 2099–2103.

29. Jones, M. R.; Osberg, K. D.; MacFarlane, R. J.; Langille, M. R.; Mirkin, C. A. Templated Techniques for the Synthesis and Assembly of Plasmonic Nanostructures. *Chem. Rev.* **2011**, *111*, 3736–3827.

30. Fan, J. A.; Wu, C.; Bao, K.; Bao, J.; Bardhan, R.; Halas, N. J.; Manoharan, V. N.; Nordlander, P.; Shvets, G.; Capasso, F. Self-Assembled Plasmonic Nanoparticle Clusters. *Science* **2010**, *328*, 1135–1138.

31. Whittell, G. R.; Hager, M. D.; Schubert, U. S.; Manners, I. Functional Soft Materials from Metallopolymers and Metallosupramolecular Polymers. *Nat. Mater.* **2011**, *10*, 176–188.

32. Peng, Q.; Tseng, Y. C.; Darling, S. B.; Elam, J. W. A Route to Nanoscopic Materials via Sequential Infiltration Synthesis on Block Copolymer Templates. *ACS Nano* **2011**, *5*, 4600–4606.

33. Chai, J.; Wang, D.; Fan, X. N.; Buriak, J. M. Assembly of Aligned Linear Metallic Patterns on Silicon. *Nat. Nanotechnol.* **2007**, *2*, 500–506.